学位論文

Synthesis and Functionalization of Oxynitride Semiconductor Anatase TaON

（酸窒化物半導体アナターゼ型TaONの合成と機能化）

平成27年12月博士（理学）申請

東京大学大学院理学系研究科

化学専攻

鈴木　温

Synthesis and Functionalization of Oxynitride Semiconductor Anatase TaON

by

Atsushi Suzuki

Department of Chemistry

Graduate School of Science

The University of Tokyo

December, 2015

Abstract

Anatase tantalum oxynitride (TaON), being one of the metastable polymorphs of TaON, is an oxynitride semiconductor with d^0 electron configuration and has the same crystal structure as anatase TiO_2, which is an oxide semiconductor applied to electric devices as a photoelectrode and a transparent electrode because of its high photocatalytic efficiency and high Hall mobility (μ_H ~20 $cm^2V^{-1}s^{-1}$). This leads to an expectation that anatase TaON can also be used as an electrode material with interesting electric and optical properties. However, anatase TaON has been synthesized only in polycrystalline fine powder form by ammonolysis, and doping of 5-15 % Mg or Sc is needed to stabilize the metastable anatase structure. As a result, the grain boundaries and doped impurities prevented the characterizations of intrinsic properties of anatase TaON. Indeed, physical properties of anatase TaON have never been reported except optical ones and even those optical properties showed large variation.

In this thesis, I synthesized undoped anatase TaON in epitaxial thin film form on the lattice matched single crystalline substrates by using nitrogen plasma assisted pulsed laser deposition (NPA-PLD). With the aid of epitaxial force from the lattice-matched single crystalline substrate, metastable anatase TaON was successfully synthesized without impurity doping. A high growth temperature and a balanced supply of oxygen and nitrogen were crucial for obtaining high-quality anatase TaON thin films. Electrical transport measurements revealed that the anatase TaON film grown at 800 °C or post-annealed in vacuum exhibited good electrical conductivity of ~1×10^{-2} Ωcm and a temperature-independent *n*-type carrier density (n_e) of the order of 10^{19} cm^{-3}, which are characteristic of degenerated semiconductors. The Hall mobility (μ_H) of ~17 $cm^2V^{-1}s^{-1}$ at 300 K is comparable to that of anatase TiO_2. The anatase TaON thin film exhibited a bandgap (E_g) of 2.37 eV and refractive index (*n*) of ~3.0 in the visible region. Generally, transparent electrodes require high μ_H and *n*, and

photoelectrodes need absorption in visible light and high μ_H for high efficiency. Thus, I concluded that anatase TaON is promising for photoelectrode and transparent electrode.

Considering the practical applications of anatase TaON, anatase TaON further needs modification of its properties. This is because electric devices require various physical properties for individual uses, for example, (1) large n_e, large E_g, and wide lineup of n in transparent electrodes, and (2) small n_e and small E_g in photoelectrodes. Therefore, I also attempted to control the optical and transport properties of anatase TaON to widen the range of applications.

Tuning of its optical properties, n and E_g, was achieved by making solid-solution with anatase TiO_2: $(TiO_2)_x(TaON)_{1-x}$, which was fabricated by NPA-PLD by carefully controlling the nitrogen amount with oxygen partial pressure. E_g systematically changed from visible light region (~2.4 eV) to ultraviolet region (> 3.2 eV) in accordance with the ratio of TaON and TiO_2, x. This implies that $(TiO_2)_x(TaON)_{1-x}$ could be optimized for wide applications from visible light active photoelectrode and transparent electrode by adjusting x. The n value in visible light region was also controlled from 3.2 (TaON side) to 2.7 (TiO_2 side).

Transport properties of anatase TaON were controlled by carrier doping with Li insertion, which was conducted by soft-chemical Li insertion with *n*-butyllithium solution. Li insertion was confirmed by lattice expansion and composition analysis. Concentration of *n*-butyllithium solution affected on both Li amount and carrier density in anatase TaON, which suggested that inserted Li generated conduction electrons as expected. The lowest resistivity of Li-doped anatase TaON was ~6.7×10^{-4} Ωcm, which was enough low for transparent electrode applications. I also tried carrier doping by W substitution. However, the carrier density of anatase TaON did not change by W substitution, possibly due to charge compensation with substitution of N^{3-} for O^{2-} during the film growth. Success of carrier

doping by Li insertion, which could avoid charge compensation, supports the above-mentioned carrier doping scenario.

Practically, low-cost and large-area fabrication is favorable. However, the requirements for growth of anatase TaON, high growth temperature and expensive single crystalline substrate, are serious disadvantage towards the practical applications of anatase TaON. I examined lowering of growth temperature and film deposition on glass without expensive single crystalline substrates, by using anatase TiO_2 seed layer, which stabilized anatase TaON with the same crystal structure as anatase TiO_2.

In summary, I demonstrated the usefulness of anatase TaON for electric devices from its high Hall mobility and unique optical properties compared to typical oxide semiconductors (high n and narrow $E_{g,}$). I also explored the ways for controlling the optical and transport properties of anatase TaON and for low-cost and large-area fabrication of anatase TaON films. Therefore, I concluded that anatase TaON is a promising material for electric devices that can solve the problem in existing devices using typical oxide semiconductor, such as low visible light absorption in photoelectrodes and low refractive index in transparent electrodes.

Acknowledgement

First of all, I would like to express the deepest appreciation to Prof. Tetsuya Hasegawa for his tremendous support in this doctoral thesis. He provided me an enthusiastic guidance, a wonderful environment on research, and an opportunity to broaden my insight such Advanced Leading Graduate Course for Photon Science (ALPS) program, JST-CREST meeting, and internship. I am also deeply grateful to Prof. Hirose Yasushi. Without his guidance, this thesis would not have materialized. Although I changed the majors from organic chemistry at master's course and was not familiar with solid state chemistry, I could learn a lot through this research thanks to his constructive comments and warm encouragement.

I also owe a very important debt to Prof. Tomoteru Fukumura, who has given me many insightful comments and suggestion contributed to my work. His advice sometimes broke the difficulty in the thesis. Advice and comments given by Dr. Akira Chikamatsu and Dr. Hideyuki Kamisaka has been a great help in promoting my research. I have received a lot of knowledge especially, experimental techniques, from Mr. Shoichiro Nakao. I would like to appreciate them.

I am indebted to my collaborators. Mr. Seiji Ito, Mr. Akira Morita, Prof. Katsuyuki Fukutani and Prof. Hiroyuki Matsuzaki of the University of Tokyo, and Prof. Kimikazu Sasa, Mr. Satoshi Ishii and Dr. Daiichiro Sekiba of University of Tsukuba assisted me to conduct nuclear reaction measurements. I received generous supports to make the optical model in spectroscopic ellipsometry from Dr. Kuniaki Konishi of the University of Tokyo and Mr. Yoshihiro Kuge of J. A. Woollam Japan. Dr. Takafumi Nakagawa, Dr. Hiroshi Okada and Prof. Yutaka Matsuo of the University of Tokyo provided me a meaningful discussion and equipment related to the reaction of Li insertion.

I also would like to appreciate Prof. Takao Someya who was the secondary supervisor in ALPS program. He provided me the opportunity of fruitful discussion with him and other ALPS program members, which assisted me to obtain new insight in my work. I also thanks ALPS program and Panasonic Corporation for the opportunity of internship.

I would like to thank the member of Hasegawa laboratory: Dr. Sohei Okazaki, Dr. Chang Yang, Dr. Daisuke Ogawa, Dr. Youngok Park, Dr. Anri Watanabe, Dr. Daichi Oka, Dr. Kei Shigematsu, Tatsunori Kawashima, Dr. Jie Wei, Shungo Kojima, Tsukasa Katayama, Thantip S. Krasienapibal, Jeon Il, Xi Shen, Kazuki Aizawa, Shun Inoue, Kenta Shimamoto, Miho Otaki, Mayuko Oka, Ryosuke Sei, Kaori Kurita, Ryosuke Takagi, Tomoya Onozuka, Kenichi Kaminga, Masahito Sano, Jumpei Takahashi, Kyohei Yamatake, Vitchaphol Motaneeyachart, Keisuke Kawahara, Yuji Kurauchi, Ryota Kantake, Fahd S. Khan, Yutaka Uchida, Dai Kutsuzawa, Takuma Takeda, Takanori Yamazaki, Naoki Kashiwa, Shunsuke Shibata, Naoaki Hashimoto, Keisuke Yamada, Yusuke Suzuki, Koki Kawahara, Toru Koizumi, Michitaka Fukumoto, Satoshi Fujiwara, and Takahiro Maruyama. I would also thank the secretaries, Ms. Mie Umino, Ms. Miki Komazawa, Ms. Mayumi Kikuchi, and Ms. Aya Imoji, for their kind supports.

Finally, I would like to express my gratitude to my family for their moral support and warm encouragements.

Contents

Chapter 1
General introduction

1.1 Oxide semiconductor

Oxide semiconductors have been used in various electric devices as important components such as photoelectrodes and transparent electrodes, but development of new oxide semiconductors with superior properties is still desired. To evaluate newly developed materials, it is needed to examine their intrinsic properties. For this purpose, single crystalline samples are favorable. In this section, I introduce the synthesis of single crystalline oxides with thin film form and typical applications of oxide semiconductors with high Hall mobility. Practically, not only synthesis and characterization methods of oxide semiconductors but also controlling their physical properties are important. Thus, I will also describe the technique to control its physical properties.

1.1.1 Synthesis of single crystalline oxide thin films

First, I explain the difference between polycrystal and single crystal briefly. Single crystal consists of one domain with one orientation in the whole region. On the other hand, polycrystal is an assembly of many single crystals called grains with different crystallographic orientation. Neighboring two grains with different orientation are separated by a grain boundary, which generally contains defects and affects “bulk” properties. For example, conduction carriers are scattered at the grain boundaries. Thus, a polycrystalline sample is not suitable for investigating intrinsic properties, such as electrical transport properties.

To prepare high quality single crystalline thin films, the process called epitaxial growth has often been used. In the epitaxial growth, single crystalline thin films are grown on single crystalline substrate as the template [1,2]: films are grown with certain orientation matching to the crystalline plane of the substrate due to interaction, called epitaxial force, between the atoms in the films and the atoms in the substrate. This process also enables us to fabricate a metastable phase selectively on an appropriate lattice-matched substrate by epitaxial force.

There are two kinds of epitaxial growth, homoepitaxial and heteroepitaxial growth. The situation that the grown thin film and the substrate have the same crystal structure and orientation is called homoepitaxial growth. Epitaxial thin films with less lattice failure such as stacking fault tend to be obtained in homoepitaxial growth, because the lattices are completely matched at the interface between thin film and substrate (Fig. 1.1a). On the other hand, if the epitaxial thin film and the substrate have different crystal structures or orientation, heteroepitaxial growth occurs. Smaller difference of lattice constants between thin film and substrate leads to less lattice failure in the grown epitaxial thin film (Fig. 1.1b). However, large lattice mismatch (generally >0.1%) causes defects called misfit transitions, which makes the crystallinity worse (Fig. 1.1c). This lattice mismatch is a main problem in heteroepitaxial growth, because the selection of single crystalline substrates as a template is limited. To improve this situation, an intermediate layer as buffer or seed layer is often

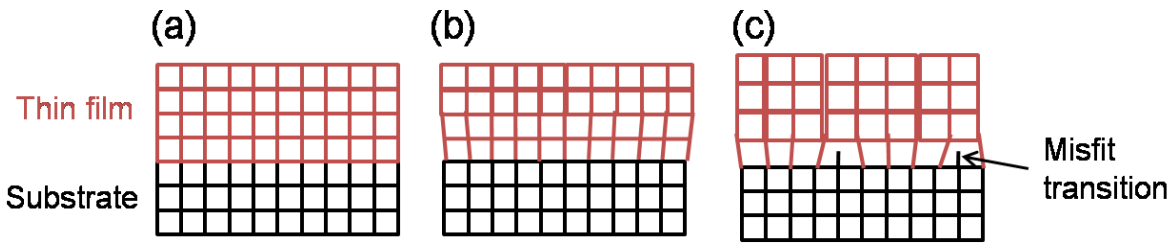

Figure 1.1 Schematic illustration of (a) homoepitaxial growth and heteroepitaxial growth with (b) small and (c) large lattice mismatch between thin film and substrate.

introduced between film and substrate [3]. Epitaxial growth is also utilized for complicated thin films such composition spread films [4] and multi-layer films [5].

1.1.2 Application of oxide semiconductors with high Hall mobility

Oxide semiconductor indicating low resistivity ($\rho < 1 \times 10^{-3}$ Ωcm) and transparency to visible light (band gap $E_g \geq 3.2$ eV) is used as a transparent electrode in electric devices such as light-emitting-diodes (LED) and solar cells [6-8]. Conductivity (σ) is determined by carrier density ($n_{e,h}$) and Hall mobility (μ_H), which indicates how quickly carriers can move through the semiconductor. High Hall mobility is favorable to obtain high conductivity as described in the following formula (1-1):

$$\sigma = \rho^{-1} = e \times n_{e,h} \times \mu_H \qquad (1\text{-}1)$$

where is the resistivity and e is the elementary charge. Thus, transparent oxide semiconductors (TOSs) with high Hall mobility have been extensively studied. A typical and widely used TOS is Sn^{4+}-doped In_2O_3 (ITO), which shows high Hall mobility (μ_H ~ 54 $cm^2V^{-1}s^{-1}$ [9]). In addition, high Hall mobility TOSs without expensive and rare In metal have been developed so far, which include Al^{3+}-doped ZnO (μ_H ~ 48 $cm^2V^{-1}s^{-1}$ [10]), F^--doped SnO_2 (μ_H ~ 19 $cm^2V^{-1}s^{-1}$ [11]), Nb^{5+}-doped anatase TiO_2 (μ_H ~ 20 $cm^2V^{-1}s^{-1}$ [12]). These TOSs satisfy the practical requirements to visible light transparency and conductivity. When using a transparent electrodes in an optoelectronic device such LED, the transparent electrode should have higher refractive index than the active layer to reduce the reflection loss at the interface between the transparent electrode and the active layer as shown in Fig. 1.2 [13]. However, conventional TOSs including ITO have smaller refractive index than active layer materials such as GaN and InN (Fig. 1.3) [14-16]. Therefore, a novel semiconductor with high Hall mobility and high refractive index is desired.

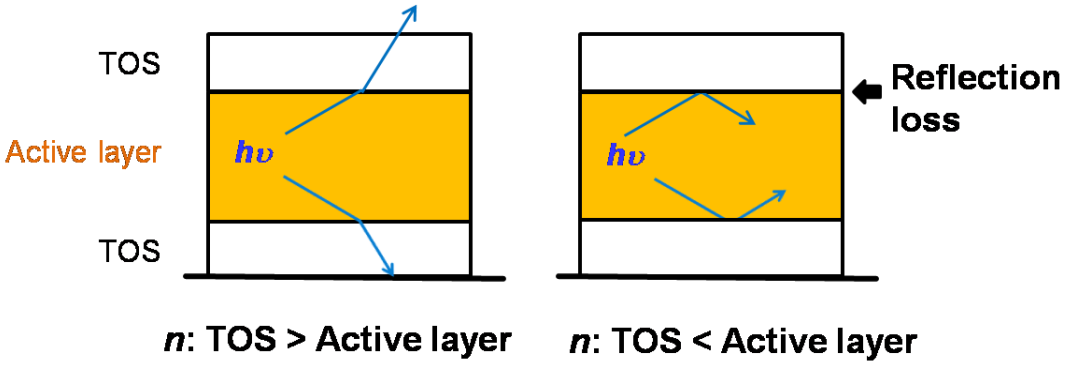

Figure 1.2 Optical path in light emitting diode with TOCs electrodes with refractive index (*n*) (a) larger and (b) smaller than that of active layer.

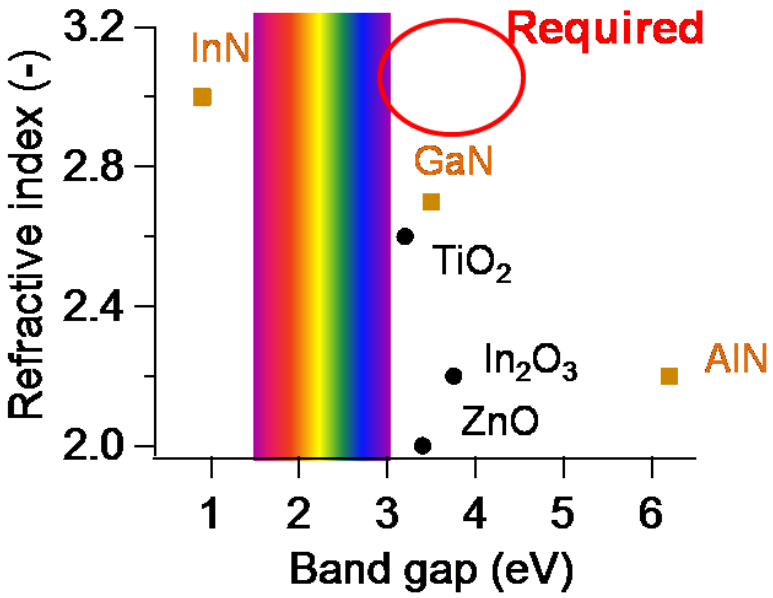

Figure 1.3 Plots of refractive index vs band gap of typical TOS (black circles) and active layer (orange squares) materials.

Oxide semiconductors are also used as photocatalysts and photoelectrodes, which show catalytic reaction under irradiation of light with larger photon energy than its band gap. Photo-carriers generated by the light irradiation decompose organic materials and generate H_2 and O_2 from water, which is called water-splitting [17]. For water-splitting, suitable band alignment in photoelectrode, that is, the lower minimum of the conduction band than

oxidation-reduction potential of H^+/H_2 and the higher maximum of the valence band than oxidation-reduction potential of O_2/H_2O, are required. In addition, high Hall mobility is favorable to obtain high photocatalytic efficiency, because the generated carriers in the photoelectrode can quickly reach to the surface at which the reaction occurs before the recombination of carriers [18]. As an oxide semiconductor meeting these requirements, anatase TiO_2 has been extensively studied [19,20]. However, pure anatase TiO_2 has lower efficiency for solar ray because of its larger band gap than visible light region (E_g~3.2 eV) [21]. In other words, anatase TiO_2 can absorb only ultraviolet rays, which is only 5% of solar ray. To obtain visible light-active photocatalysts and photoelectrodes, band gap engineering of existing oxide semiconductors and development of novel materials have been made as described in the later section.

As described above, anatase TiO_2 is one of the most extensively studied oxide semiconductors because of its high photocatalytic efficiency and high Hall mobility. Here, I briefly explain about anatase TiO_2. Anatase TiO_2 is a metastable polymorph of TiO_2. The most thermodynamically stable phase is rutile TiO_2. Both anatase and rutile structures have tetragonal symmetry and are composed of edge-sharing Ti-O_6 octahedra, where a Ti atom occupies the center and are coordinated with six O atoms (Fig. 1.4). The difference in the two structures is the number of shared edges with neighboring Ti-O_6 octahedra: rutile and anatase have two and four shared edges in Ti-O_6 octahedra, respectively. Detailed physical properties, such as transport properties, of anatase TiO_2 had not been known until recently because of the difficult in synthesis of metastable anatase structure. However, this problem has been overcome by synthesis of single crystalline anatase TiO_2 [22,23]. As a result, it was revealed that anatase TiO_2 show higher conductivity and photocatalytic efficiency than rutile TiO_2 because of its high Hall mobility [21,24].

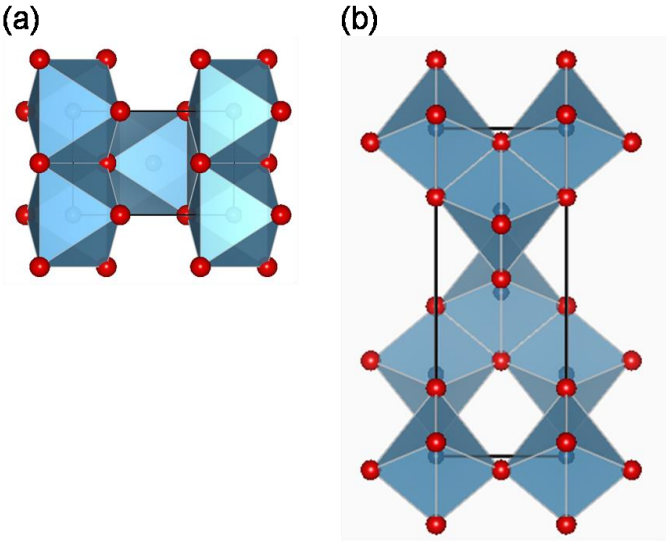

Figure 1.4 Crystal structure of (a) rutile and (b) anatase TiO_2; blue ball: Ti, red ball: O. The black solid lines indicate the unit cell.

1.1.3 Control of physical properties for practical applications

Controlling physical properties of oxide semiconductors is practically important because each electric device requires physical properties for its use. As shown in Fig. 1.5, for example, transparent electrodes need large band gap ($E_g \geq 3.2$ eV), wide lineup of refractive index and large carrier density ($n_{e,h} \geq 1\times10^{20}$ cm^{-3}) to achieve transparency to visible light, less reflection loss at the interface and high conductivity, respectively [6,13]. In contrast, photoelectrodes need small carrier density and small band gap ($E_g < 3.2$ eV) for reducing recombination site of generated photo-carriers and increasing absorption of solar ray, respectively [17,25]. Therefore, controlling optical properties and carrier densities in oxide

---

The structures shown in Fig. 1.4 were produced by VESTA software; K. Momma and F. Izumi, "VESTA 3 for three-dimensional visualization of crystal, volumetric and morphology data," *J. Appl. Crystallogr.*, **44**, 1272-1276 (2011).

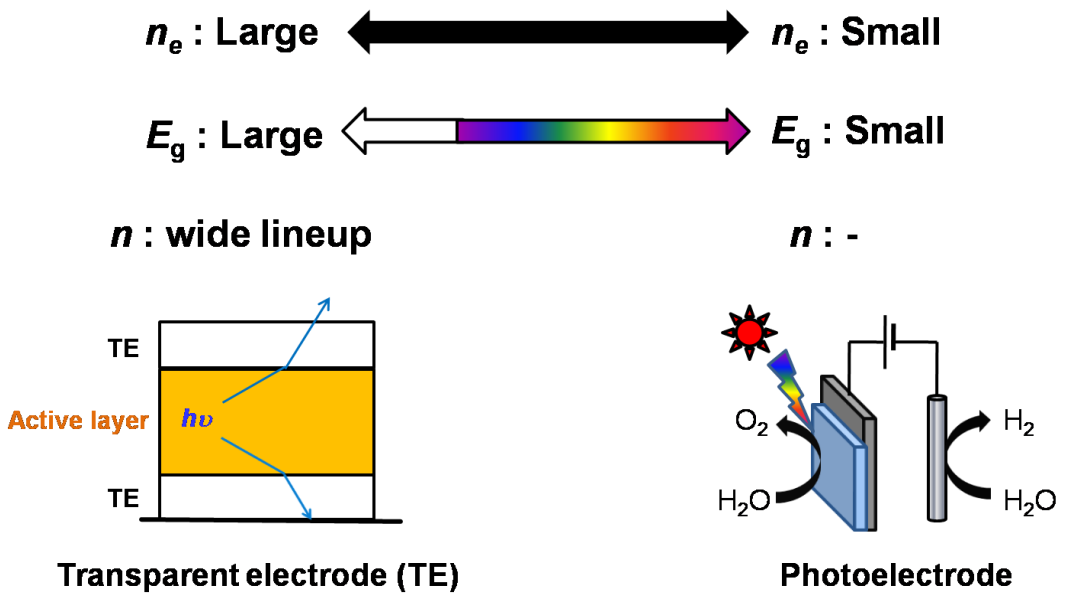

Figure 1.5 Favorable physical properties in transparent electrode and photoelectrode.

semiconductors have been extensively studied.

The majority of oxide semiconductors have band gap values in ultraviolet region. It is suitable for transparent electrodes but insufficient for photoelectrodes as described above. To overcome the situation in photoelectrodes, band gap narrowing in oxide semiconductors has mainly been achieved by doping an element with smaller electronegativity than oxygen such as nitrogen [26], phosphor [27] and sulfur [28]. Because of the smaller electronegativity, *p*-orbitals of these elements form energy levels shallower than O 2*p* orbital, which makes band gap narrower (Fig. 1.6) [29]. However, there is a limit to the doping amount because the doped element has different valence or ion size from oxygen. For example, in heavily nitrogen doped anatase TiO_2, rutile TiO_2 as a secondary phase appears [30]. This limitation in doping results in small controllable range in band gap. In addition, doping generally worsens crystallinity and generates anion vacancy due to charge compensation effect. These decrease Hall mobility and increase the density of recombination site for generated photo-carriers,

resulting in worse photocatalytic efficiency [31]. Solid-solution method is also an established way for band gap engineering in compound semiconductors. Using two materials, *A* and *B*, with the same crystal structure and different optical properties, band gap can be controlled widely in complete solid-solution $A_{1-x}B_x$ ($0 \leq x \leq 1$) as shown in Fig. 1.7 [32]. When the crystal structure is different between the two materials, the solid-solution can be synthesized only at a certain *x* range [33].

As described in Equation (1-1), not only high Hall mobility but also high carrier density $n_{e,h}$ of the order of 10^{20} cm^{-3}: i.e., degenerated *n*-type or *p*-type semiconductors, are necessary for transparent electrodes to achieve high conductivity [6]. When ions with different valence are introduced into host crystal, electron or hole can be generated. Thus, substitutional or insertional doping is the most common method to increase the carrier density in oxide semiconductors. Most of researches on transparent electrodes have been developed to *n*-type TOSs such In_2O_3, SnO_2 and ZnO. Examples of *n*-type doping to these materials are ITO [9], Sb^{5+} [34] or Ta^{5+} [35] or F^- [11] -doped SnO_2, and Al^{3+} [10] or Ga^{3+} [36] -doped ZnO, which show higher carrier density and conductivity than non-doped ones. Not only intentionally doped impurities but also native defects such oxygen vacancies and interstitial cations act as donors in oxide semiconductors [37,38]. Some films even show degenerated *n*-type conduction with 10^{20} cm^{-3} order of carrier density originating from native defects. Later than these reports, anatase TiO_2 was also categorized as a high mobility wide-gap semiconductor of which carrier density can be controlled in a wide range, from insulator to degenerated semiconductor, by chemical doping (Nb^{5+} [12], Ta^{5+} [39], W^{6+} [40], F^- [16]) or oxygen vacancy [21].

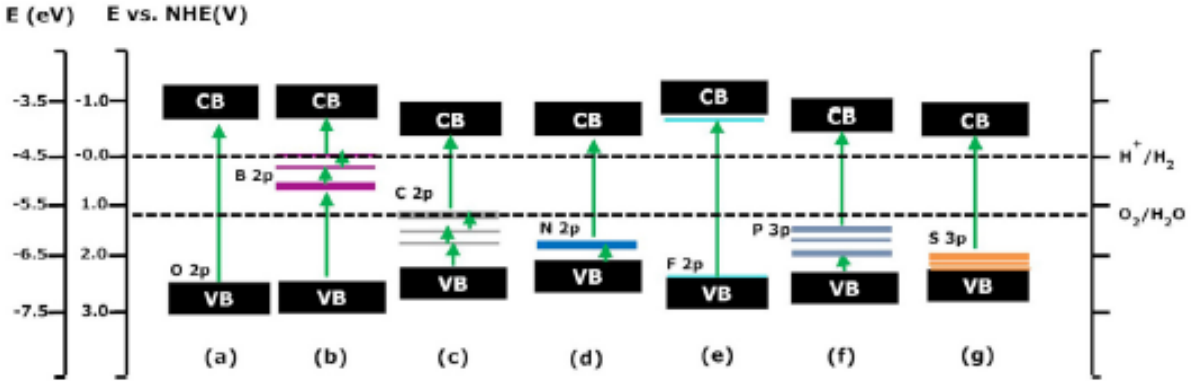

Figure 1.6 Calculated valence band maximum (VBM) and conduction band minimum (CBM) positions of metal-doped $SrTiO_3$ as compared with those of the corresponding experimental values of pure $SrTiO_3$. The VBM and CBM values are given with respect to the NHE potential (V) and energy with respect to vacuum (eV). (a) Un-doped $SrTiO_3$, (b) one B atom doped $SrTiO_3$ at 4.167 atom%, (c) one C atom doped $SrTiO_3$ at 4.167 atom%, (d) one N atom doped $SrTiO_3$ at 4.167 atom%, (e) one F atom doped $SrTiO_3$ at 4.167 atom%, (f) one P atom doped $SrTiO_3$ at 4.167 atom%, (g) one S atom doped $SrTiO_3$ at 4.167 atom%. Reprinted by permission from [29]. "Copyright 2013, Elsevier B.V."

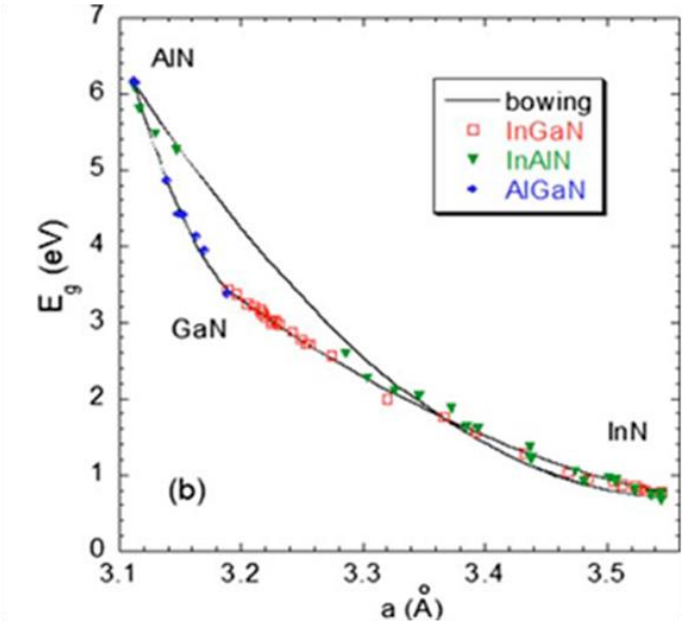

Figure 1.7 Band gap (E_g) of InGaN, InAlN, and AlGaN plotted as a function of in-plane lattice constant *a*. Reprinted by permission from [32]. "Copyright 2009, American Institute of Physics"

1.2 Oxynitride semiconductor

Oxynitride semiconductors contain two kinds of anions, oxygen and nitrogen and indicates unique optical properties compared to oxide semiconductors. Therefore, oxynitride semiconductors are expected to widen the range of physical properties of oxide-based materials. Meanwhile, the growth method and/or condition for oxynitrides are very different from those of oxides, because nitrogen is less reactive than oxygen. In this section, I introduce the present state of synthesis and physical properties of oxynitrides.

1.2.1 Synthesis of oxynitride

Most of oxynitride materials are synthesized from bulk polycrystalline powders of oxide by partial nitriding reaction with ammonia gas, which is called ammonolysis (Fig. 1.8) [41,42]. Nitrogen atoms are substituted for oxygen atoms in the precursor oxide powders under ammonia gas flow at high temperature (≥800 ˚C). Although the synthesis of oxynitride by ammonolysis is conventionally used, the obtained oxynitrides are in bulk polycrystalline powder form and not suitable for investigation of their intrinsic physical properties. Oxynitrides are usually decomposed at lower temperature than their melting points, which prevents to obtain densely sintered samples from the polycrystalline powders. Thus, the oxynitride samples synthesized by ammonolysis are forms of polycrystalline, and measured physical properties are largely affected by extrinsic factors such grain boundaries. Moreover, the nitrogen amounts in the obtained powders are too sensitive to reaction conditions such as reaction temperature, flow rate of ammonia, and wetness of ammonia, which sometimes results in emergence of impurities and inhomogenity such a gradient of nitrogen amount from the surface to the inside of grains [41]. Because of this, reported physical properties tended to show scattering, as typically seen in band gap values of $Ga_{1-x}Zn_xN_{1-x}O_x$ [43-45].

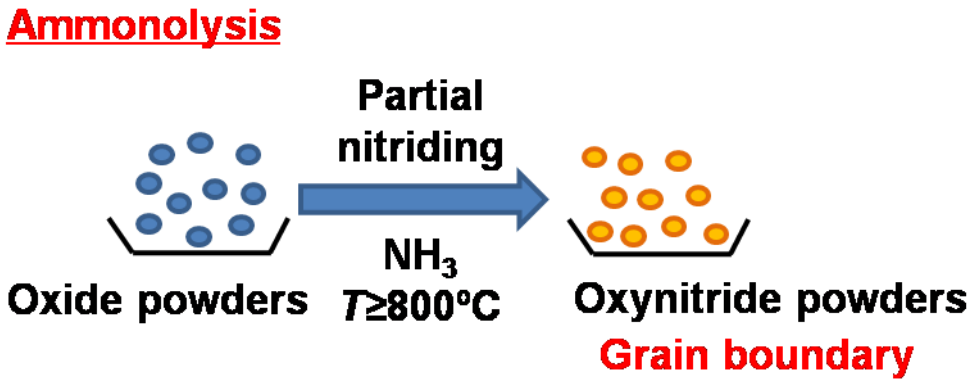

Figure 1.8 Schematic illustration of ammonolysis.

Thus, oxynitride samples of single crystalline film form with carefully controlled nitrogen amounts are required to investigate their intrinsic properties. For this purpose, epitaxial thin film growth is a promising approach. Indeed, oxynitride epitaxial thin films were successfully synthesized under various atmosphere such as N_2 gas [46], NH_3 gas [47], N_2 plasma [48, 49], and NH_3 plasma [49], although poor crystallinity and difficulty in controlling nitrogen amounts often became problems. When using inert N_2 gas atmosphere, another issue is that the reaction condition is limited to high temperature and high N_2 pressure. Because there are less reports on the epitaxial growth than that of ammonolysis, the epitaxial growth of oxynitrides still needs further studies.

1.2.2 Physical properties of oxynitride

Generally, metal oxynitrides indicate narrower band gap than oxides because of smaller electronegativity of nitrogen than that of oxygen, which makes N 2*p* orbital shallower than O2*p* orbital. Thus, some oxynitrides absorbs visible light and indicate vivid color. Comparing to nitrogen-doped oxide materials, oxynitrides can contain larger amounts of nitrogen, which leads to strong absorption in visible light region and large shift of band gap. Thus, oxynitride semiconductors can use solar-ray more efficiently than oxide

semiconductors such as anatase TiO_2 with band gap of ~3.2 eV [21]. Therefore, metal oxynitrides have attracted much attention as non-toxic pigment [50] or visible-light active photocatalysts [51] in the last decade.

In addition, the band gap of some oxynitrides is controlled by making solid-solution with oxide materials. As I described above, two materials with the same crystal structure and different optical properties are required for fabricating complete solid-solution. Because oxygen and nitrogen have almost the same ionic radii, there are many combinations of oxide and oxynitride with the same crystal structure. As one example, the band gap of the solid-solution with perovskite structure, $(NaTaO_3)_x(LaTaON_2)_{1-x}$, can be changed from ultraviolet region to visible light region ($2.0<E_g<4.1$ eV) by increasing the ratio of oxynitride [52].

Nitrogen in a crystal affects not only the band gap but also the refractive index (n). Oxynitrides usually have larger refractive index than oxides, due to smaller electronegativity of nitrogen than that of oxygen [53]. Generally, refractive index (n) becomes larger when polarizability (α) in a crystal increases as described in Equation (1-2):

$$\alpha(r) = \frac{3}{4\pi N_A}\frac{n^2-1}{n^2+2}\frac{W}{\rho} \qquad (1\text{-}2)$$

where N_A is the Avogadro's number, W is the molecular weight, and ρ is the density. The polarizability increases by decreasing ionicity of bond (r_σ) as follows:

$$\alpha(r) \cong \frac{M}{2\upsilon_A}\left(\frac{r_\sigma'+1}{r_\sigma'}\right) \qquad (1\text{-}3)$$

where $M=<0|e^2r^2|0>$ and υ_A is the atomic pseudopotentials. Considering the difference of electronegativity between cation and anion, metal-nitrogen bond has smaller ionicity than metal-oxygen bond. This leads to large refractive index in oxynitrides with metal-nitrogen bonds.

In contrast to the extensive studies carried out on the optical properties of oxynitrides, less attention has been paid to their electrical properties, mainly because of the difficulty in obtaining single crystalline or densely sintered samples as described above. Considering the diverse progress in oxide-based electronics, metal oxynitrides are also expected to exhibit attractive electrical properties [42, 51]. Recently, in fact, novel electrical functionalities were found in oxynitrides, as exemplified by high electron mobility in amorphous ZnO_xN_y [54,55], high dielectric constant and ferroelectricity in $SrTaO_2N$ [56, 57] and carrier type tunability and colossal magnetoresistance in $EuWO_{1+x}N_{2-x}$ [58].

1.2.3 A novel material, anatase TaON

In this section, I describe anatase TaON, which is a transition metal oxynitride semiconductor with d^0 electric configuration (d^0: $Ta^{5+}O^{2-}N^{3-}$) and one of polymorphs of TaON. I first introduce the TaON polymorphs and then explain about anatase TaON, which is the target material in my thesis.

Generally, TaON takes monoclinic baddeleyite structure as the most thermodynamically stable phase. Baddeleyite TaON (β-TaON) has been synthesized from the oxide powder (Ta_2O_5) by ammonolysis at 800-850˚C similar to other oxynitrides [59]. There are a few reports on the epitaxial growth of single crystalline β-TaON thin films [60]. The conduction band of TaON mainly consists of Ta 5*d* orbital. On the other hand, the valence band consists of N 2*p*, O 2*p* and Ta 5*d* orbital as shown in Fig. 1.9 [61]. TaON has narrower band gap (E_g~2.4 eV) and larger refractive index at wavelength of 633 nm (n~2.5-2.9) than Ta_2O_5 (E_g~3.9 eV, n~2.2) because of smaller electronegativity of nitrogen than that of oxygen as described in the previous section [62,63]. Therefore, β-TaON has been studied as a visible light active photocatalyst. Actually, there are reports on the photocatalytic activity, such a

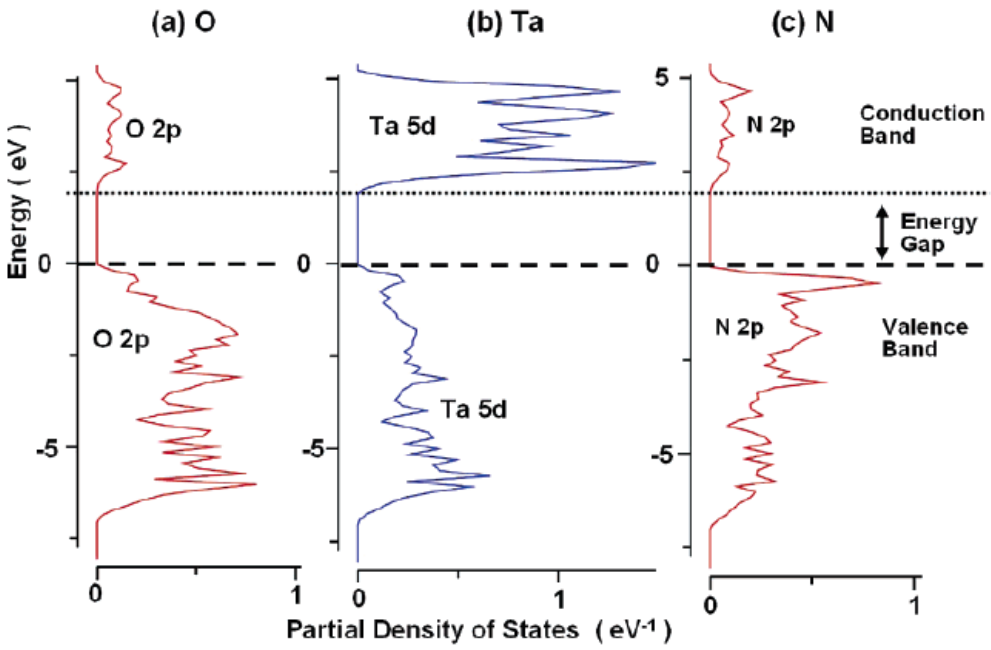

Figure 1.9 Part of a diagram of partial DOS for (a) O 2p, (b) Ta 5d, and (c) N 2p orbitals in TaON as determined by the VASP program. Reprinted by permission from [61]. "Copyright 2007, American Chemical Society"

water-splitting and oxidation of organic molecule, of *β*-TaON under visible light irradiation [64,65]. Similar to anatase TiO_2, TaON has the band alignment suitable for water-splitting.

In the last decade, experimental [66-69] and theoretical [70] studies have revealed the existence of various metastable polymorphs of TaON with anatase, bixbyite, fluorite, rutile, and VO_2 (*B*)-type structures. These metastable TaON phases have been synthesized only in polycrystalline fine powder form by nitriding precursor Ta_2O_5 powders under high-temperature ammonia flow, similar to *β*-TaON. Furthermore, substitution of Mg^{2+}, Sc^{3+}, Y^{3+}, etc. for Ta^{5+} is needed to stabilize the metastable anatase, bixbyite, fluorite and rutile structure. The substituted metal forms oxide domains with sixfold coordination in host crystal, which probably stabilize the metastable phases of TaON with sixfold coordination such anatase and rutile structures [71]. In case of TaON with VO_2 (*B*)-type structure (*γ*-TaON), lower ammonia flow rate and shorter reaction time than those of *β*-TaON are needed for

growth of phase pure γ-TaON instead of impurity doping. No need of the cation substitution in γ-TaON is explained by the stabilization energy as shown in Fig. 1.10, which indicates that γ-TaON is the most stable among the metastable polymorphs of TaON [68]. Anatase TaON is the second most stable, and very recently, synthesis of anatase TaON without additives was reported, though the obtained product contained large amounts of Ta_3N_5 and β-TaON [72]. These TaON show absorption in visible light region similar to β-TaON [70], and, especially, γ-TaON reveals photocatalytic activity in water splitting under visible light irradiation [73]. I also note that TaON with fluorite structure is expected to show the colossal ion conductivity of N^{3-} [69] similar to O^{2-} conductivity in oxides with fluorite structure, which has been applied to electrolytes in solid oxide fuel cells and oxygen sensors [74].

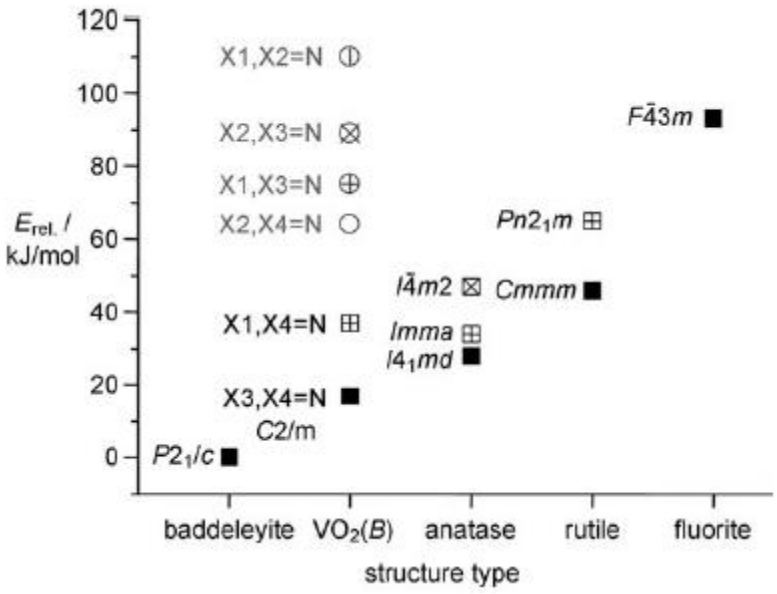

Figure 1.10 Calculated relative energies E_{rel} (PW1PW method; normalized to one formula unit) of TaON in different structure types with different anion orderings. Reprinted by permission from [68]. "Copyright 2007, John Wiley & Sons, Inc."

As my research target, I focused on anatase-type TaON from the viewpoint of electronics applications, because its crystal structure and cation electronic configuration (d^0) are identical to those of anatase TiO_2, which is a well-established *n*-type oxide semiconductor

as described in the previous section. Because anatase TiO_2 shows high Hall mobility and has been applied to transparent electrodes, photoelectrodes, and so on, anatase TaON is promising for electric devices in which high Hall mobility is required. Considering the optical properties in typical oxynitrides such as narrow band gap and high refractive index, anatase TaON has the potential to solve some problems in existing photoelectrode and transparent electrode materials based on oxide semiconductors, that is, low visible light absorption in photoelectrodes and small refractive index in transparent electrodes. However, there is a serious obstacle to investigate the intrinsic properties of anatase TaON, coming from the limititation of existing synthesis method, ammonolysis. As described above, anatase TaON has been synthesized only in polycrystalline fine powder form by ammonolysis with the need of substitution of 5-15% of Mg^{2+} or Sc^{3+} for Ta^{5+}, which behaves as an acceptor to trap carrier electrons [66, 67]. These practical factors, i.e., poor electrical connection between randomly oriented grains and high concentration of doped acceptor impurities, hinder investigation of the electrical properties of anatase TaON. Indeed, electrical transport properties of anatase TaON have never been reported. Therefore, new synthetic route to overcome the above-mentioned limitation needs to be developed.

1.3 Purpose

As mentioned above, anatase TaON is expected as a novel oxynitride semiconductor applicable to electric devices such as photoelectrodes and transparent electrodes. However, intrinsic physical properties of anatase TaON have never been investigated because anatase TaON had synthesized only in bulk polycrystalline powder form with impurities. To overcome the difficulty in synthesizing pure anatase TaON single crystal, I tried to stabilize the anatase structure by using epitaxial force from lattice-matched single

crystalline substrate as has already reported for metastable anatase TiO_2 [22]. Considering that some oxynitrides in thin film form were synthesized by PLD [48, 49], I attempted to synthesize undoped anatase TaON epitaxial thin films by using nitrogen plasma assisted pulsed laser deposition (NPA-PLD) in this study. Intrinsic optical and electric transport properties of the obtained films were investigated to confirm whether anatase TaON is truly promising as photoelectrode and transparent electrode materials, that is, whether anatase TaON indicates high Hall mobility and unique optical properties compared to oxide semiconductors.

As described in Section 1.1.3, not only developing a novel material but also controlling its physical properties are important because electric devices require various properties for each use. For example, high efficiency transparent electrodes need large carrier density, large band gap and wide lineup of refractive index. In contrast, photoelectrodes need small carrier density and small band gap. Therefore, I tried to control the physical properties of anatase TaON to widen the range of applications. I studied two topics related to this purpose. One is tuning of optical properties by making solid-solution with anatase TiO_2: $(TiO_2)_x(TaON)_{1-x}$. The solid-solution thin films were fabricated by NPA-PLD similar to pure anatase TaON and the optical properties of the obtained thin films were investigated. The other topic is carrier doping to anatase TaON by W substitution and Li insertion, which were conducted by NPA-PLD and soft-chemical process, respectively. I investigated the transport properties of the doped anatase TaON and discussed which process was suitable for carrier doping to anatase TaON.

For practical applications of anatase TaON, low-cost and large-area fabrication is required. To widen the growth condition, particularly to lower the growth temperature, of anatase TaON, I tried to stabilize anatase TaON by using various kinds of single crystalline substrates and anatase TiO_2 seed layer. Moreover, use of expensive single crystalline

substrate to stabilize the metastable anatase structure is a serious disadvantage towards its practical applications. Thus, I aimed at establishing the synthesis process of anatase TaON on inexpensive substrates such as glass.

Chapter 2
Experimental technique

2.1 Pulsed laser deposition (PLD) [75,76]

PLD is a one of physical vapor deposition techniques and has been widely used for fabricating thin films under non-equilibrium condition. Main components of PLD are a sintered pellet called a target, a substrate as a template of the thin film growth, both of which are set in a vacuum chamber, a laser for ablation and gas sources. A pulsed laser beam is focused onto the target and vaporizes the target surface. The materials vaporized from the target form plasma, called plume, which includes molecules, atoms, ions, clusters, and so on. The plume reaches to the substrate and species are deposited on the substrate surface. The deposited species migrate on the substrate, and some of them are re-evaporated and the remaining forms a thin film on the substrate. During the deposition, the substrate is heated by an infrared laser or lamp as necessary. The deposition is conducted under ultra-high vacuum or gas atmosphere supplied from the gas source; oxygen gas is often used for growth of oxides. Quadrupled and tripled Nd:YAG laser (λ = 266 and 355 nm, respectively), ArF excimer laser (λ = 193 nm), and KrF excimer laser (λ = 248 nm) are usually used for vaporizing the target surface in PLD. These lasers with several hundred nm wavelength have enough high photon energy to ablate the target surface. A target with the same composition as objective thin films is usually used, because PLD technique has the good transcription of cation from the target to the thin film. To obtain single crystalline thin films with good crystallinity by epitaxial growth, single crystalline substrates, which have good lattice matching to the objective thin film, are selected.

Here I summarize the merits of PLD as follows:

- Facilitating deposition of materials with high melting points such as oxides
- Less deviation of composition between the target and the thin film
- Precise control of the growth rate of the thin film by laser conditions for ablation
- Growth of multi-layer films by exchanging targets
- Synthesis of metastable materials under non-equilibrium condition

In this thesis, I fabricated anatase TaON and anatase $(TiO_2)_x(TaON)_{1-x}$ on lattice-matched substrates by PLD, which is suitable for growth of these materials, because they are metastable phases. A KrF excimer laser (λ = 248 nm) and an infrared lamp to heat the substrate were used for the growth. As targets, I prepared the oxide ceramic target, Ta_2O_5 or $Ti_xTa_{1-x}O_y$. Cations and oxygen were supplied by ablating the oxide ceramic targets using a KrF excimer laser. Additional oxygen was sometimes supplied as O_2 gas. Nitrogen was supplied as N_2 gas, which was activated into radicals by a radio-frequency wave (RF) plasma source (SVT Associates, Model 4.5"). The RF plasma source generated radicals from the gas molecules by induction field at electrodeless discharge lamp caused by radio-frequency wave. The deposition under nitrogen radical by PLD is called nitrogen-plasma-assisted pulsed laser deposition (NPA-PLD). A schematic illustration of NPA-PLD used in this thesis is shown in Fig.2.1.

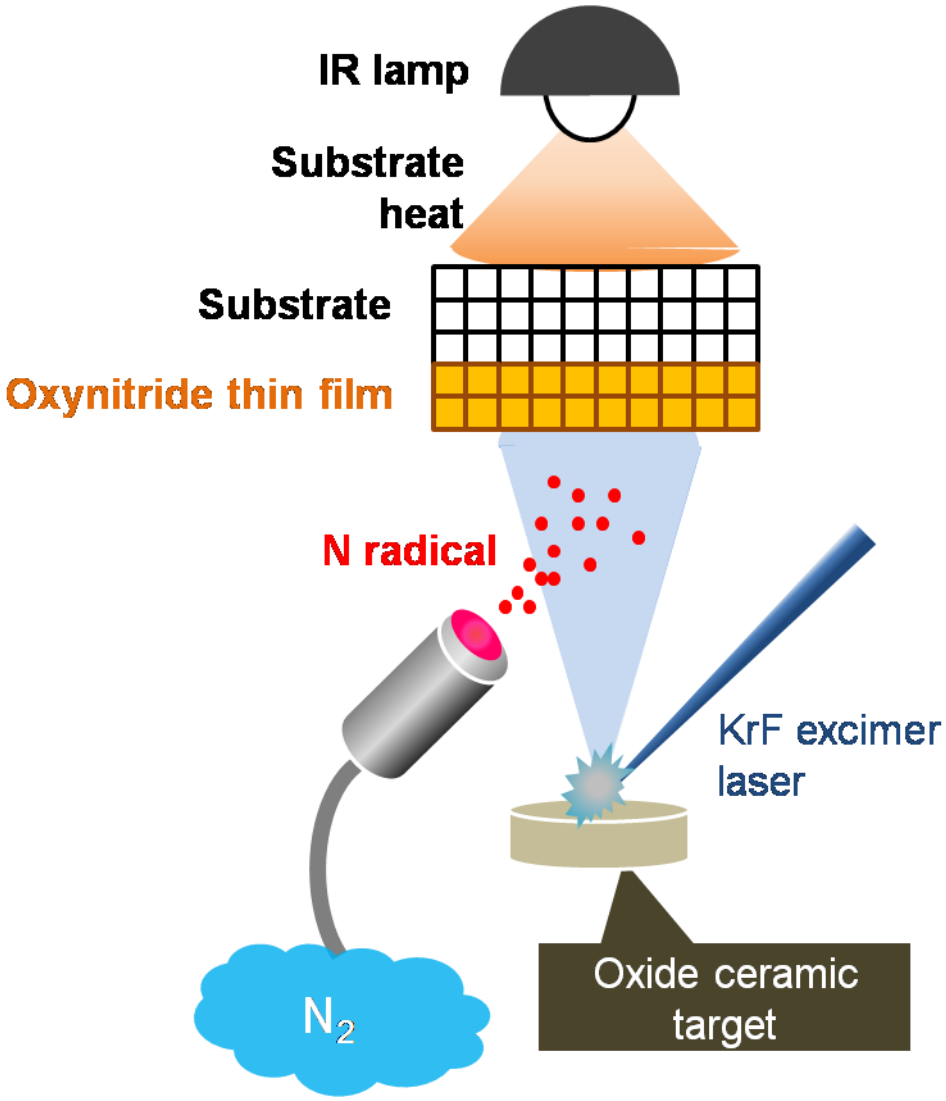

Figure 2.1 Schematic illustration of NPA-PLD setup

2.2 X-ray diffraction (XRD) [77]

X-ray diffraction is a phenomenon that X-ray undergoes diffraction from a sample with a periodic structure such as crystal lattice. By using this phenomenon, crystal structure can be determined.

X-ray diffractometer consists of X-ray generator, sample stage, and detector as

shown in Fig. 2.2. Samples can be tilted towards the directions described by angles ω and χ. Angles ω and 2θ represent the positions of the detector and the measured sample relative to the incident X-ray. In addition, samples can be rotated with the φ axis, which is perpendicular to the sample stage. The detector can move along another circular rail, with an angle 2θ to X-ray incident beam. An X-ray tube is used as the X-ray generator, where heated electrons generated at anode collide with the cathode metal. Cu metal is usually used as the cathode and characteristic X-ray from Cu ($\lambda = 0.15418$ nm) is generated. This X-ray is irradiated onto the sample put on the sample stage. When X-ray enters the sample with periodic structure such as crystal, X-ray diffraction occurs when the angles meet Bragg's law:

$$2d\sin\theta = m\lambda \qquad (2\text{-}1)$$

where d is the distance between diffraction planes (spacing of lattice planes in crystal), λ is the wavelength of incident X-ray, and m is any integer. Spacing of lattice planes in sample crystal (d) can be obtained by detecting the diffracted X-ray at specific positions, where the diffraction occurs. Each crystalline material is characterized by a specific crystal system and lattice constants, and thus X-ray diffraction patterns can be regarded as fingerprints of materials. Thus, crystal structure of the sample can be determined by XRD. There are several lineups for X-ray detectors: 0D (spotty), 1D (linear) and 2D (circular) detectors with different performances. Fine measurements are often conducted by 1D and 0D detectors because of their high resolution. On the other hand, not only 2θ direction but also χ direction of the diffraction peak can be detected by using 2D detector. Ring-shaped diffraction patterns along χ direction (Debye ring) are observed on the two-dimensional detector in case of polycrystalline samples, while diffraction patters are spot-like in case of single crystalline samples.

In this thesis, XRD measurements were conducted with a commercial diffractometer (Bruker AXS, d8 discover). Crystal structures and lattice constants of the

obtained thin films were determined by XRD measurements. In addition, crystallinity and symmetry of the film were investigated by rocking curve (ω) and φ scans, respectively. The detail of these measurements are described as follows.

Crystallinity can be evaluated from rocking curve, which is ω scan with a fixed 2θ, χ and φ. The rocking curve represents the distribution of the tilting of the crystal plane. Thus, crystallinity is usually investigated as the full width at half maximum (FWHM) of rocking curves. The symmetry of crystal can be determined by the φ scan, which is a measurement with rotation around the φ axis at fixed 2θ, χ and ω. In case of single crystals, the same number of diffraction peaks as the rotational symmetry appear. In addition, epitaxial relationship between substrates and thin film can be determined by comparing the symmetry of substrate and thin film.

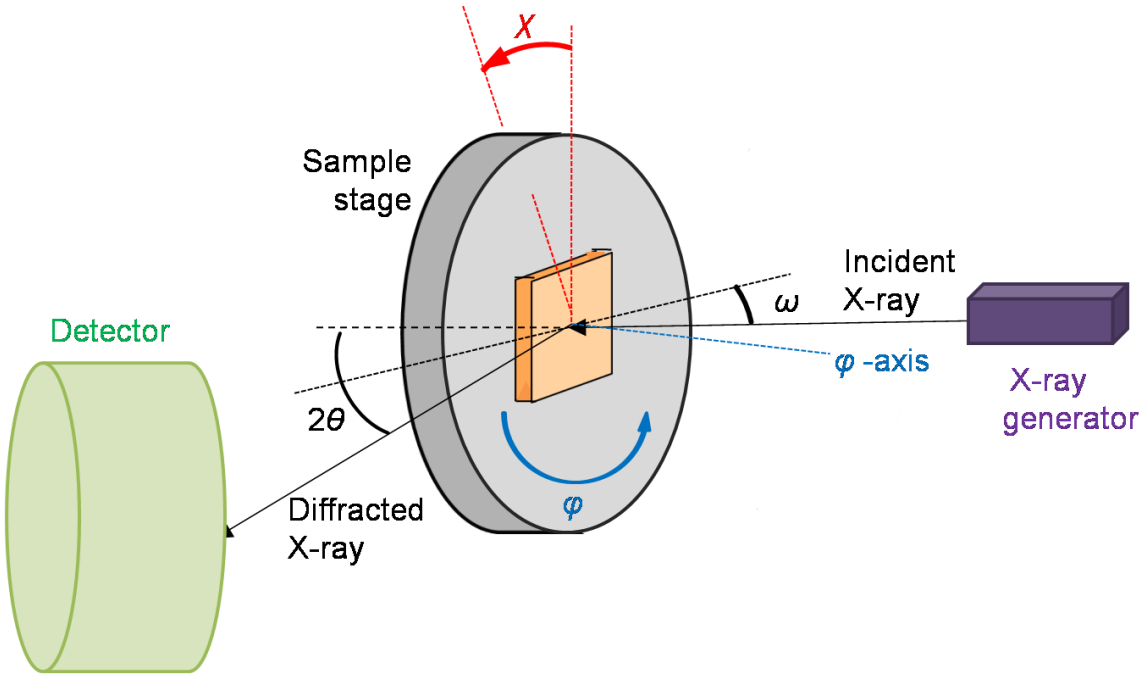

Figure 2.2 Schematic illustration of XRD setup. This geometry corresponds to χ=90º.

2.3 Transmission electron microscopy (TEM) [78]

TEM is a microscope technique to obtain the information of the inner structure of materials, such as crystal structures and defects, by detecting the electron beam transmitted through a sample. Because this electron beam interacts with atoms in the sample, one can obtain the information of the inner structure by TEM. The transmitted electron beam is observed by a fluorescent screen. The convergent angle and beam size of the electron beam on the sample flakes and fluorescent screen are controlled by some lenses equipped at the both side of the electron beam path to obtain clear images.

Compared to other analysis, TEM has remarkable advantages that it can be observe very small areas with high resolution and thus direct information about the crystal structures and defects can be obtained. On the other hand, the sample must be thin enough that electron beam can pass through. In general, an appropriate thickness is from 5 to 500 nm. Such thin samples are obtained by several techniques such as milling with focused ion beam and mechanical milling. Besides, the TEM samples should be flat, damage-free and contamination-free.

2.4 Atomic force microscopy (AFM) [79]

AFM is a kind of scanning probe microscopes with high spatial resolution (~1 nm). In case of AFM, surface morphology of sample such as roughness can be observed by detecting atomic force between probe tip and sample surface. When the sample surface is scanned two-dimensionally by the probe attached to the end of a cantilever spring, the atomic force between surface and probe bends the cantilever. Displacement of cantilever by this bending is measured by optical lever method. In this method, a laser beam reflected by the

back surface of the cantilever is detected by a position sensor (photo-diodes) which translates the displacement of cantilever by the bending to the displacement of the reflected laser beam. The surface morphology is imaged by this displacement. The distance between probe and surface is kept constant by moving the sample stage upward or downward by a piezoelectric driver during the measurement.

In this thesis, AFM measurements were conducted by a commercial scanning probe microscopy system (SII-nanotechnology, SPI4000 with SPA400).

2.5 Scanning electron microscopy / Energy dispersive X-ray spectroscopy (SEM-EDX) [80]

2.5.1 Secondary electron microscopy (SEM)

SEM is an electron microscope to investigate the surface morphology of solid materials by using accelerated and focused electron beam as a probe. When this electron beam is irradiated to a sample, emissions, such secondary electrons and backscattered electrons, are generated through interaction between the probe electrons and the atoms of the sample. Information of surface morphology is obtained by detecting these emissions (secondary electron is usually used.). Compared to optical microscope, SEM is useful to obtain stereoscopic images because of deeper depth of focus than optical microscope.

When the electron beam is irradiated to the sample, characteristic X-ray is also emitted from the atom in the sample. By detecting this characteristic X-ray, elemental analysis of the sample can be conducted. Details are as follows.

2.5.2 Energy dispersive X-ray spectroscopy (EDX)

EDX is a technique for elemental analysis of samples by detecting the characteristic X-ray emitted from the atoms in the samples. Silicon pin diode diffused Li is used as a detector. A characteristic X-rays from different atoms can be treated as different voltage pulses by the silicon pin diode, because electron-hole pairs with energy proportional to the energy of the characteristic X-ray is generated in this detector at the time of detecting the characteristic X-ray. By translating this voltage to the energy of the characteristic X-ray, energy spectrum of the sample can be obtained. Because the energy of the characteristic X-ray is specific to each atom, the chemical composition of the sample can be determined from the peak position in the energy spectrum (qualitative analysis). On the other hand, the number of detected voltage pulse corresponds to the peak intensity in energy spectrum. Although correction by standard samples is needed, the amount of the each element can be evaluated from the peak area (quantitative analysis).

In this thesis, anion amount in oxynitride thin films were determined by SEM-EDX. SEM-EDX measurements were conducted at the Research Hub for Advanced Nano Characterization, The University of Tokyo, under the support of "Nanotechnology Platform" (project No. 12024046) by MEXT. Instead of a standard sample, simulation software (SIMNRA and Casino) was used for quantitative analysis. The simulation software gives us the energy spectrum corresponding to assumed composition. By comparing the obtained energy spectrum by SEM-EDX with simulated energy spectrum, I determined the composition of thin films.

2.6 Nuclear reaction analysis (NRA) [81]

NRA was used to determine the nitrogen amount in oxynitride thin films. Determining the quantity of nitrogen is conducted by the following nuclear reaction:

$$^{15}\mathrm{N} + p \rightarrow \quad \text{compound nucleus} \rightarrow \quad ^{12}\mathrm{C} + \alpha + \gamma \qquad (2\text{-}2)$$

This reaction formula means the generation of ^{12}C and the emission of α-ray (α) and γ-ray (γ) after the reaction ^{15}N isotope with proton (p).This reaction is also described as follows:

$$^{15}\mathrm{N}(p,\alpha\,\gamma)^{12}\mathrm{C} \qquad (2\text{-}3)$$

The energy of emitted α-ray and γ-ray is always the same, when nuclear reaction of ^{15}N(p,α γ)^{12}C occurrs.

In this thesis, I determined the amount of nitrogen in oxynitride thin films by irradiating proton beam of 898 keV to the oxynitride thin films and detecting γ-ray peculiar to the nuclear reaction of ^{15}N(p,α γ)^{12}C. The γ-ray was observed by two $Bi_4Ge_3O_{12}$ scintillators, which emit fluorescence when absorbing γ-ray. By amplifying this emitted fluorescence, ^{15}N from the nuclear reaction of ^{15}N(p,α γ)^{12}C became detectable. By comparing the results measured for a sample and TiN epitaxial thin films as references, the amount of nitrogen in the sample was calculated. In this study, NRA measurements were conducted with a 1-MV tandetron accelerator at Tandem Accelerator Complex, University of Tsukuba.

2.7 Secondary ion mass spectrometry (SIMS) [82]

SIMS is a technique to determine the composition in solid materials by detecting the mass of secondary ions with mass spectrometry. When primary ions are irradiated to the surface of a sample, secondary ions are generated by collision between primary ions and atoms or molecules at the surface of sample. SIMS conducts under high vacuum to prevent

the contamination at the surface and the collision between the secondary ions and the background gas species. SIMS is a very sensitive analytical technique with detection limits of ~10^{12}-10^{16} atm/cm^3 and can be categorized as quantitative analysis when a standard sample is available. There are two kind of measurement modes, dynamic mode (D-SIMS) and static mode (S-SIMS). In D-SIMS, elemental distribution along the depth direction can be obtained by sputtering the surface during the measurement.

In this thesis, Li amounts and their distributions along the depth direction in anatase TaON thin films were determined by D-SIMS. Primary ion and acceleration voltage used are O_2^+ and 2.0 kV, respectively. The Li amount was evaluated using a standard sample, TaON thin film doped with Li^+ by ion implantation, within experimental errors of ~40%.

2.8 X-ray photoelectron spectroscopy (XPS) [83]

XPS is a technique to investigate elemental composition and electronic states of elements in a sample. In this technique, kinetic energy of photoelectron emitted from the sample is observed after X-ray is irradiated to the sample. The kinetic energy (E_k) is described by the energy of irradiated X-ray ($h\nu$), the work function (Φ), and the binding energy of electron (E_b), as shown in the following equation:

$$E_k = h\nu - \Phi - E_b \qquad (2\text{-}4)$$

Thus, from the binding energy of electron, which is specific to each element and its valence states, and its chemical environment. one can obtain compositional and electronic information.

In this thesis, the valence of cation in oxynitride thin films was determined by a commercial XPS system (PHI5000 Versa Probe, ULVAC-PHI).

2.9 Spectroscopic ellipsometry [84]

Ellipsometry is an optical technique to investigate the optical constants (refractive index (n) and extinction coefficient (k)) of thin films. Ellipsometry is composed of a light source with a polarizer, a sample stage, an analyzer and a detector. In this technique, linearly polarized light is irradiated to a thin film on the sample stage and polarized light reflected at the sample surface is detected. By changing the wavelength of the irradiated linearly polarized light continuously, an optical spectrum can be obtained, which is called spectroscopic ellipsometry.

There are two components in the polarized light, *s*-polarized light and *p*-polarized light. The former is the light polarized perpendicular to the incident plane, while the latter is the light polarized parallel to the incident plane. Because the *s*-polarized and *p*-polarized light show the different reflection behavior at the sample surface, the phase and intensity become different between *s*- and *p*-polarized light. Thus, elliptical polarized light is detected after the reflection, which is the origin of the name of ellipsometry. The elliptically polarized light is represented with parameters of Ψ and Δ, which denote to the intensity ratio and the phase difference between *s*- and *p*-polarized light, respectively, and depend on the wavelength of incident light, incident angle, thickness of the thin film and optical constants of the material. Therefore, the optical constants and the thickness of a thin film sample can be obtained from the information of Ψ and Δ in the elliptically polarized light.

For the analysis, an optical model, which is composed of a substrate and single layer or multi-layers with different thickness and optical constants, is used. The thickness and optical constants of each layer can be evaluated by repeating fitting procedures until a good fit is obtained.

In this thesis, optical constants n and k of oxynitride thin films were determined using a commercial spectroscopic ellipsometer (J.A. Woollam, M-2000U).

2.10 Ultra violet-visible-near infrared spectroscopy

Optical band gap can be determined by transmittance *T* and reflectance *R*, which are related to absorption coefficient α as follows:

$$\alpha = \frac{1}{t}\ln\left(\frac{1-R}{T}\right) \qquad (2\text{-}5)$$

where *t* is the film thickness. This equation is approximation in ignorance of multiple reflections.

In this thesis, these transmittance and reflectance values were measured by ultra violet-visible-near infrared spectroscopy.

2.11 Electric transport property measurement

In this thesis, electrical transport properties (ρ: resistivity, *n*: carrier density, and μ_H: Hall mobility) were measured by van der Pauw method and two-probe method. A physical property measurement system (Quantum Design, model 6000) was used to control the sample temperature between 10 and 300 K and the external magnetic field between −9 T and 9 T. In this section, van der Pauw method and two-probe method are mainly described.

2.11.1 van der Pauw method [85,86]

van der Pauw method is a technique suitable for electrical transport measurement of materials in thin film form. Theoretically, there is no limit for the two dimensional shape of thin film sample in van der Pauw method. In this thesis, I used thin films with dimension of ~5×5 mm and electrodes with <0.8 ×0.8 mm size. Schematic drawing of van der Pauw method is shown in Fig. 3.3a, where black regions correspond to electrodes.

The probe connection for van der Pauw method is depicted in Fig. 3.3b. Resistance is measured by four-probe method as shown in 2ch and 3ch geometry in Fig. 3.3b. In the four-probe method, the electrodes for measuring the voltage drop and flowing a DC electric current are different. Unexpected voltage drop originated from extrinsic resistances such as resistance of lead wire and ammeter, and contact resistance can be neglected. Thus, the four-probe method is suitable for the samples with relatively low resistivity. In 2ch geometry, DC electric current flows between electrodes A and B (I_{AB}) and the voltage drop between the electrodes C and D (V_{CD}) is measured. The resistance ($R_{AB,CD}$) evaluated by I_{AB} and V_{CD} is given as.

$$R_{AB,CD} = V_{CD} / I_{AB} \qquad (2\text{-}6)$$

In case of 3ch geometry, the resistance ($R_{BC,DA}$) evaluated by I_{BC} and V_{DA} is expressed as

$$R_{BC,DA} = V_{DA} / I_{BC} \qquad (2\text{-}7)$$

The resistivity is evaluated by $R_{AB,CD}$ and $R_{BC,DA}$ as described in the following equation:

$$\rho = \frac{\pi d}{\ln 2} \frac{R_{AB,CD} + R_{BC,DA}}{2} f\left(\frac{R_{AB,CD}}{R_{BC,DA}}\right) \qquad (2\text{-}8)$$

where d is the thickness of a thin film sample and f is the van der Pauw correction factor to compensate the inhomogenity of resistance originated from irregular shape of the sample, position of electrode, and so on. f cannot be solved analytically. In contrast, when $R_{AB,CD} / R_{BC,DA} < 10$ ($R_{AB,CD} > R_{BC,DA}$), f can be determined by using the following approximation:

$$f \approx 1 - \left(\frac{R_{AB,CD} - R_{BC,DA}}{R_{AB,CD} + R_{BC,DA}}\right)^2 \frac{\ln 2}{2} - \left(\frac{R_{AB,CD} - R_{BC,DA}}{R_{AB,CD} + R_{BC,DA}}\right)^4 \left[\frac{(\ln 2)^2}{4} - \frac{(\ln 2)^3}{12}\right] \qquad (2\text{-}9)$$

My samples used in this thesis, satisfied $R_{AB,CD} / R_{BC,DA} < 10$ because of good homogeneity of resistance and sample shape. Thus, f is determined by Equation (2-9).

Carrier density and Hall mobility are evaluated by Hall effect measurement

conducted with 4ch geometry of Fig. 3.3b. When magnetic field (B_z) is applied perpendicular to the thin film surface, flowing carriers from electrode A to C receive Lorentz force and the flowing direction is curved, which cause the gradient of carrier density along BD direction in Fig. 3.3b. In steady state, carriers flow straight due to the gradient of carrier density to balance the Lorentz force. When the sample has only one type of carriers, the voltage between electrode B and D (V_{BD}) is described by the following simple equation:

$$V_{BD} = -I_{AC} B_z / d\, n\, e \tag{2-10}$$

where I_{AC} is the electric current flowing between electrode A and C, and e is the elementary charge. The Hall coefficient (R_H) is defined as

$$R_H = E_{BD} / j_{AC} B_z \tag{2-11}$$

where E_{BD} is the electric field along BD direction, and j_{AC} is the current density along AC direction.

From the Equations (2-10) and (2-11), Hall coefficient is given as follows:

$$R_H = V_{BD} / I_{AC} B_z = R_{BD,\,AC} / B_z = -1 / d\, n\, e \tag{2-12}$$

where $R_{BD,\,AC}$ is the Hall resistance measured with 4ch geometry in van der Pauw method as shown in Fig. 3.3b. Thus, carrier density and Hall coefficient can be determined by the slope of $R_{BD,\,AC}$ vs B_z plot. Furthermore, carrier type can be determined by the sign of Hall coefficient: positive and negative signs correspond to hole and electron carriers, respectively. Hall mobility can be evaluated by resistivity and carrier density with Equation (1-1):

$$\mu_H = R_H / \rho \tag{2-13}$$

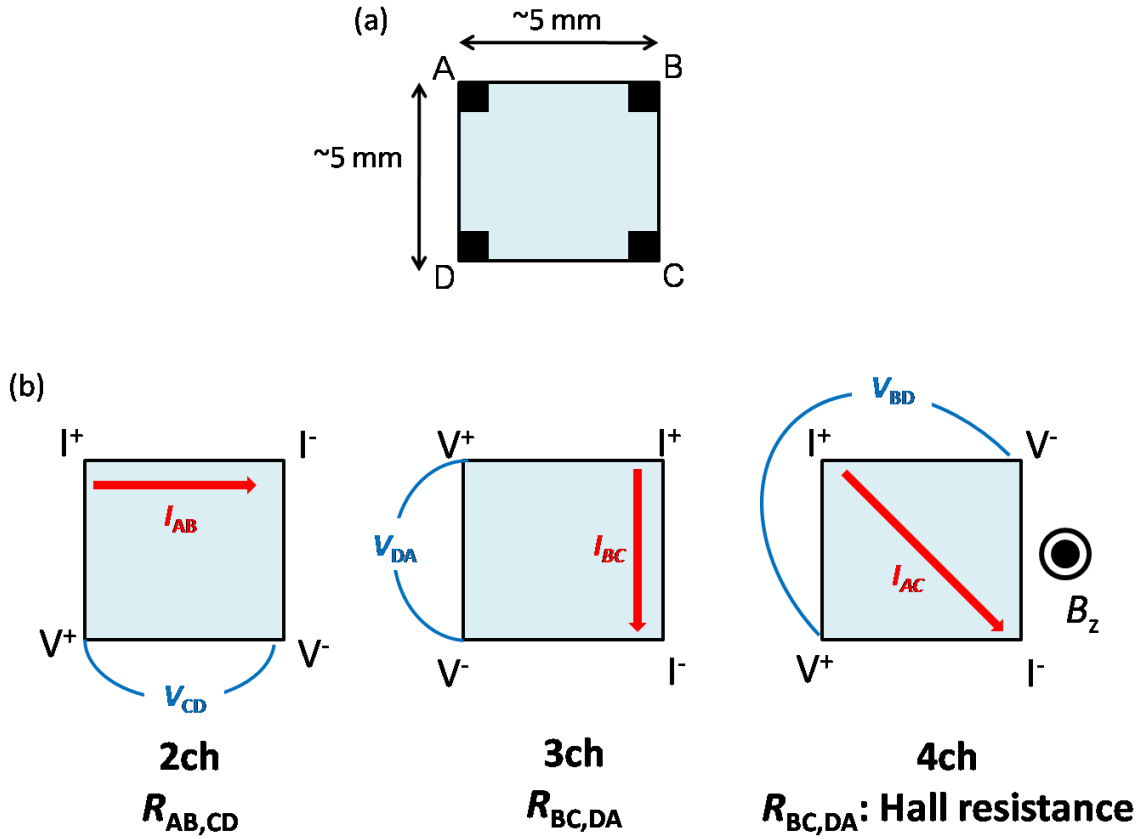

Figure 2.3 (a) Sample geometry for van der Pauw method. (b) Probe connections for 4-probe resistance (2ch and 3ch) and for Hall resistance (4ch).

2.11.2 Two-probe method

When the resistance of a sample is relatively high, two-probe method is more favorable than four-probe method. In two-probe method, the electrodes for detecting the voltage drop and flowing a DC electric current are the same. When the sample resistance is much larger than inner resistance of ammeter, the contribution of extrinsic resistance becomes negligibly small. Thus, the two-probe method is suitable for the sample with relatively high resistance.

Chapter 3
High-mobility electron conduction in oxynitride: anatase TaON

3.1 Introduction

As mentioned in Chapter 1, phase pure anatase TaON epitaxial thin films, whose electric properties are less affected by grain boundaries, are desired to investigate intrinsic physical properties of anatase TaON. In this chapter, I present a new synthetic route of anatase TaON, namely, epitaxial growth by nitrogen plasma assisted pulsed laser deposition (NPA-PLD) on a lattice-matched single crystalline substrate, where the epitaxial force from the substrate stabilizes the metastable anatase structure without the need for impurity doping reported in previous reports [66, 67]. The growth conditions of anatase TaON epitaxial thin films obtained with this method were optimized through the growth temperature and growth rate. Optical and transport properties of anatase TaON thin films indicating a good single-crystal quality were investigated to confirm whether anatase TaON is promising for practical application such a photoelectrode and a transparent electrode as a novel material.

---

*This chapter contains the contents of the following publications.

"High-Mobility Electron Conduction in Oxynitride: Anatase TaON"
A. Suzuki, Y. Hirose, D. Oka, S. Nakao, T. Fukumura, S. Ishii, K. Sasa, H. Matsuzaki, and T. Hasegawa, Chem. Mater. **26**, 976 (2014)

3.2 Experimental procedure

Anatase TaON thin films were grown by NPA-PLD on $(LaAlO_3)_{0.3}$-$(SrAl_{0.5}Ta_{0.5}O_3)_{0.7}$ (LSAT) (001) single crystalline substrate (cubic, a/2 = 0.3868 nm) with good lattice matching to the (001)-plane of anatase TaON predicted by a first-principles calculation (tetragonal, a = 0.392 nm) [70]. A ceramic Ta_2O_5 target was sintered from Ta_2O_5 powder (99.99% purity) at 1400 °C for 15 h in air. A pulsed laser beam from a KrF excimer laser (λ = 248 nm) was focused onto the Ta_2O_5 target. The fluence and repetition rate of the excimer laser were adjusted to control the deposition rate to 10-16 nm/h. The substrate temperature (T_S), serving as the main growth parameter, was varied from 650 to 800 °C by infrared lamp heating. Deposition was conducted under a partial N_2 gas pressure of 1×10^{-5} Torr, where the supplied N_2 gas was activated into radicals by a radio-frequency wave (RF) plasma source (SVT Associates, Model 4.5") with an output power of 250 W. Typical film thicknesses were 30-45 nm, evaluated by a stylus profiler with experimental error of ~5 nm. Some of the films were successively annealed at 800 °C for 20 minutes under base pressure (< 2×10^{-7} Torr) in the growth chamber.

Crystal structures of the films were examined by X-ray diffraction (XRD) measurements using Cu-Kα radiation and a four-axis diffractometer (Bruker AXS, d8 discover). Surface morphology of the obtained thin films was investigated by the atomic force microscope (AFM). Cross-sectional transmission electron microscope (TEM) observation was also performed to ensure the microscopic structure of the film. The TEM specimen was prepared by the focused ion beam micro-sampling method. The oxygen and nitrogen contents were evaluated by an energy dispersive x-ray spectroscope equipped with a scanning electron microscope (SEM-EDX), within experimental errors of ~10%. The electron accelerating voltage was set at 2.5 kV in order to reduce the background signal from the substrate. The nitrogen content was also cross-checked by nuclear reaction analysis (NRA)

using a $^{15}N(p, \alpha\gamma)^{12}C$ resonance reaction at 898 keV, which included an experimental error of ~20% due to the small sample thickness and instability of the energy of a proton beam. Valence of Ta in TaON thin films was examined by X-ray photoelectron spectroscopy. Electrical resistivity (ρ), carrier electron density (n_e), and Hall mobility (μ_H) were determined by the van der Pauw method with Au/Ti electrodes. The ρ values of highly resistive samples were evaluated by a two-probe method. A physical property measurement system (Quantum Design, model 6000) was used to control the sample temperature between 10 and 300 K and the external magnetic field between −9 T and 9 T. Optical constants of the anatase TaON films were determined by spectroscopic ellipsometry (J. A. Woolam, M-2000U) in a spectral range of 1-5 eV. A series of ellipsometric spectra obtained at incident/reflection angle from 50° to 80° with 5° step were analyzed for each sample by using a model of a single-layer film on a substrate. The dispersion function of a TaON film was modeled as a sum of single Tauc–Lorentz [87] and single Lorentz dispersion function. The optical anisotropy of anatase TaON was ignored in the analysis because isotropic and anisotropic optical models gave almost the same results.

3.3 Results and discussion

3.3.1 Synthesis of anatase TaON epitaxial thin films.

Anatase TaON thin films were grown by NPA-PLD, where a ceramic Ta_2O_5 target was ablated and reacted with nitrogen radical introduced into the growth chamber. Figure 3.1a compares θ-2θ XRD patterns of the TaON films grown on LSAT (001) single crystal substrates at various T_S. As seen from the figure, the crystal growth was quite sensitive to T_S. The films grown at $T_S \geq 750$ °C showed peaks at 2θ = ~35° and ~74°, which correspond well

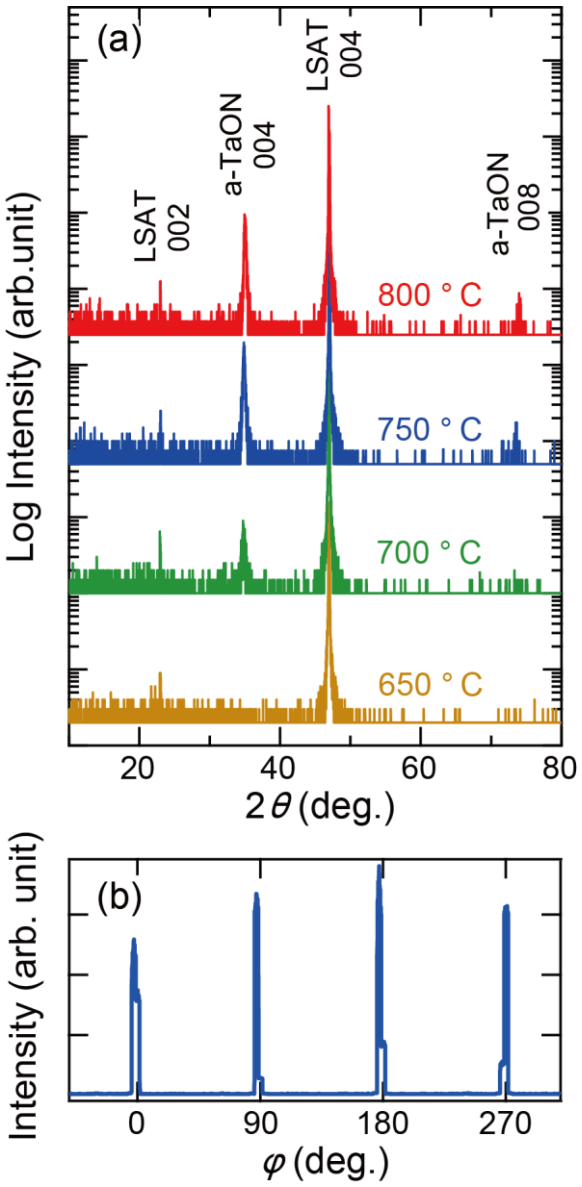

Figure 3.1 (a) θ-2θ XRD patterns of the TaON films grown on LSAT substrates at various T_S. "a-TaON" represents anatase TaON. (b) φ-scan plot of 101 diffraction from the anatase TaON film grown at 750 °C. φ = 0° was set parallel to the <100> direction of the LSAT substrate.

to the 004 and 008 diffraction of anatase TaON predicted by first-principles calculations [70], namely, 2θ = 35.5° and 75.2°, respectively. Meanwhile, for the film deposited at $T_S \leq 700$ °C, these peaks became weak or even undetectable. I also conducted asymmetrical reflection measurements on the films grown at $T_S \geq 750$ °C and confirmed the epitaxial relationships

$(001)_{TaON}$ || $(001)_{LSAT}$ and $[100]_{TaON}$ || $[100]_{LSAT}$, as expected from the lattice-matching. The φ-scan plot of the 101 diffraction (Fig. 3.1b) revealed four-fold rotational symmetry, consistent with this epitaxial relationship. The full width at half-maximum (FWHM) value of the φ-scan plot was ~0.6°, which means that small in-plane twist exists in the film. I also note that no impurity phases, such as Ta_2O_5 and baddeleyite-TaON, were detected in these measurements.

AFM measurements were also conducted to investigate the surface morphology of anatase TaON. As shown in Figs. 3.2a and 3.2b, square shape grains pattern were observed in both anatase TaON thin films fabricated at T_S = 750 and 800°C, which reflected (001)-plane shape of tetragonal anatase structure. Although sizes of the grains were different in each growth temperature, both films showed good flatness as shown in Figs. 3.2c and 3.2d (root mean square ~ 0.4 nm^{-1}). I also note that no segregation implying impurity phase were detected. The film grown at T_S = 750 °C was further investigated by cross-sectional TEM. A low-magnification TEM observation (Fig. 3.3a) revealed a sharp interface between the film and substrate, without intermixing or phase segregation, though planar defects along the {101} planes of anatase TaON, which were possibly attributable to stacking faults, were frequently seen. Contrast variations between the triangular domains would be originated from small in-plane twist of crystals. High-resolution TEM images (Figs. 3.3b and 3.3c) showed a characteristic lattice pattern of the anatase structure, as reported previously for anatase TiO_2 [88]. The electron diffraction pattern (Fig. 3.3d) also verified the (001) growth of anatase TaON. From these results, I concluded that phase-pure anatase TaON was successfully obtained as a consequence of the epitaxial force from the LSAT substrate, without the aid of Mg or Sc doping. The chemical composition of the anatase TaON thin film grown at 750 °C was evaluated as $TaO_{0.94\pm0.09}N_{1.04\pm0.1}$ by using SEM-EDX. The nitrogen content per formula unit determined by NRA was 1.2 ± 0.2, which is in good agreement with the SEM-EDX

results, within the experimental error.

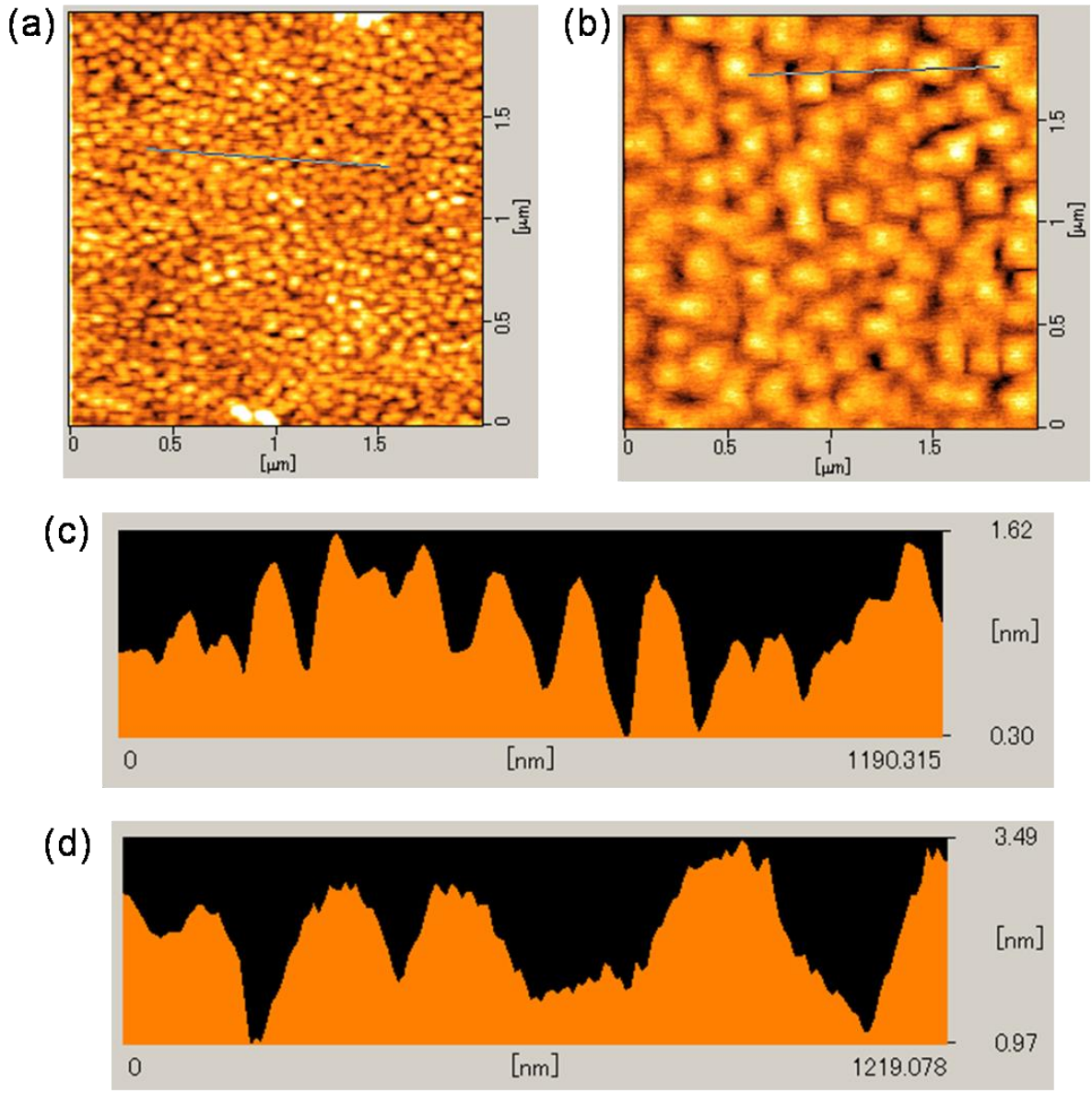

Figure 3.2 AFM images of anatase TaON thin films fabricated at (a) 750 and (b) 800 °C. Cross-sectional profiles of anatase TaON thin films fabricated at (c) 750 and (d) 800 °C. Blue lines in AFM images (a) and (b) represent the position of cross-sectional profiles.

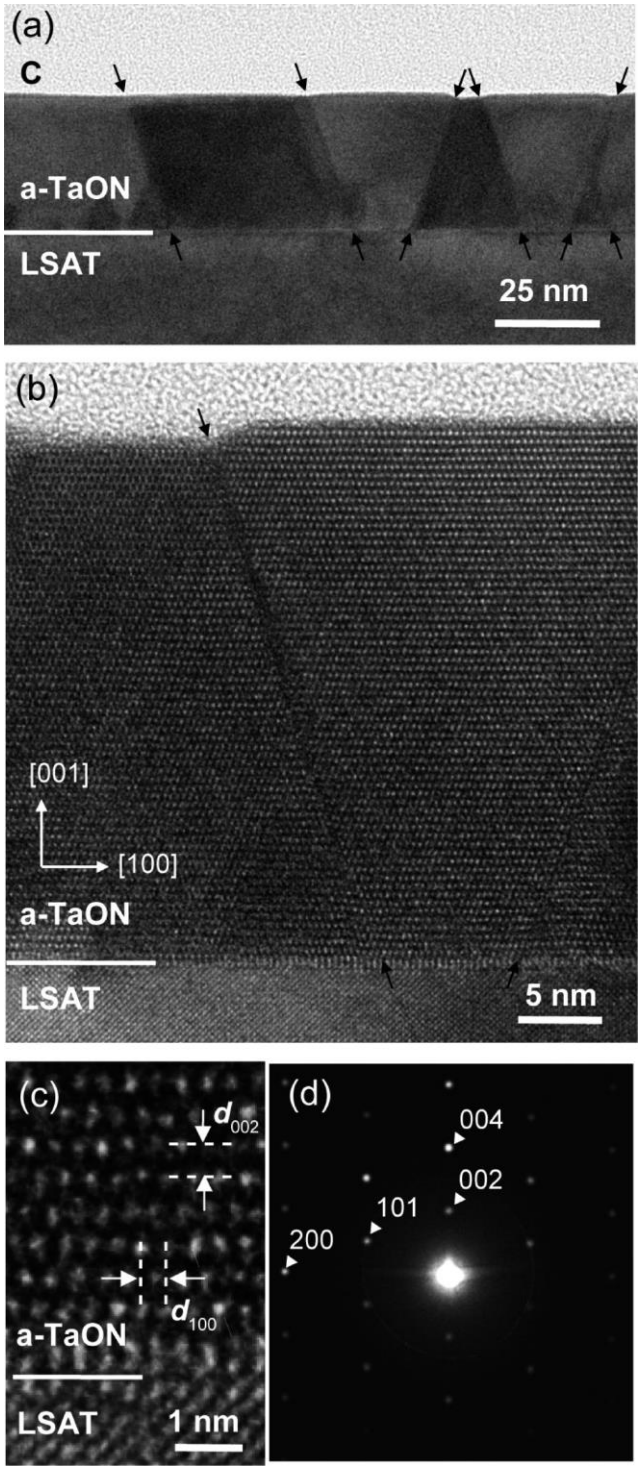

Figure 3.3 (a, b) Cross-sectional TEM image of the anatase TaON thin film grown at 750 °C, viewed along the [010] zone axis of the LSAT substrate. The arrows indicate planar defects along the {101} planes of the anatase TaON. (c) High-resolution image of the same sample. (d) Electron diffraction pattern of the same anatase TaON film. The weak ring pattern originated from the carbon coated on the film.

Figure 3.4a shows the rocking curves of the anatase TaON 004 diffraction measured for the films grown at various T_S. Notably, FWHM value shows a minimum ~0.09° at T_S = 750 °C; in other words, the best crystallinity was obtained at T_S = 750 °C. Another key growth parameter is the film growth rate, which is determined by the ablation rate of the Ta_2O_5 target. At a high ablation rate (high laser fluence or high repetition rate), oxygen was oversupplied from the target compared with the nitrogen radical introduced from the plasma source, resulting in the formation of Ta_2O_5 as a secondary phase (Fig. 3.4b). At $T_S \geq 750$ °C, the optimal deposition rate was found to be 10-16 nm/h. In the following section, I present the physical properties of the phase-pure anatase TaON thin films grown at $T_S \geq 750$ °C.

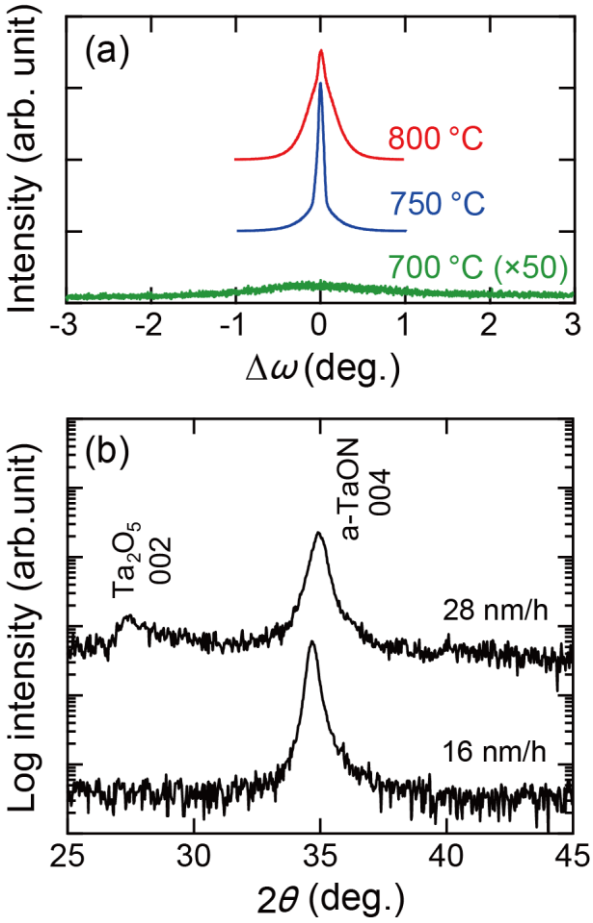

Figure 3.4 (a) Rocking curves of anatase TaON 004 for the films grown at various T_S. (b) θ-2θ plots of the anatase TaON thin films deposited at 750 °C with optimal (16 nm/h) and excessively high (28 nm/h) growth rates. The output power of the RF source was set at 300 W for the deposition of the films in (b).

3.3.2 Electrical transport properties of anatase TaON

Figure 3.5a plots ρ values of the anatase TaON films fabricated at T_S = 750 °C and 800 °C as functions of temperature. The former showed a high ρ of 10^2 Ωcm order at 300 K and semiconducting temperature dependence ($d\rho/dT < 0$), whereas the latter showed a four orders of magnitude lower ρ at 300 K (~1×10^{-2} Ωcm) and metallic temperature dependence ($d\rho/dT > 0$) down to ~100 K. Figure 3.6 shows Hall resistance vs magnetic field plot for a typical TaON thin film. Negative slope in this Hall measurements revealed that electrons carried the charges (*n*-type semiconductor). I also noted that linear relationship between Hall resistance and applied magnetic field can be observed clearly, which assures reliability of my measurement. Considering the T_S dependence of ρ and the *n*-type conduction, the carrier electrons might have originated from anion vacancies, whose number would increase at higher T_S, as frequently seen in oxide or nitride semiconductors. I further annealed the anatase TaON film (T_S = 750 °C) in vacuum at 800 °C. As shown in Fig. 3.5a, ρ was substantially reduced by the annealing, and the ρ–T curve of the annealed film was comparable to that of the anatase TaON film grown at T_S = 800 °C, supporting the above hypothesis about the carrier source. I note that the number of anion vacancies could not be determined by composition analysis, because the number of vacancies estimated from the carrier density was much lower than the experimental error (~10%). In fact, the chemical composition of the film grown at T_S = 800 °C was evaluated as $TaO_{1.0\pm0.1}N_{1.0\pm0.1}$ by SEM-EDX, which agreed well with the film grown at T_S = 750 °C, within the experimental error. XPS measurements of the TaON thin films in order to obtain information about the amount of oxygen vacancies also supported this estimation of the small number of vacancies. Figure 3.7 shows Ta 4*f* core level photoemission spectra of the TaON thin films fabricated at 750 ºC and 800 ºC. In both spectra, Ta $4f_{7/2}$ and $4f_{5/2}$ peaks are composed of a single component assignable to Ta^{5+}. That is, no spectral components of lower valence states, such

as Ta^{3+}, was detected even in the film fabricated at 800 ºC, which should contain more oxygen vacancies. This indicates that the amount of oxygen vacancies was too small to be detectable by XPS. Considering the carrier density in the film fabricated at 800 ºC (~3.7×10^{19} cm), the amount of oxygen vacancies would be of the order of 10^{20} cm^{-3}, which corresponds to ~0.4% relative to Ta atoms (~2.6×10^{22} cm^{-3}).

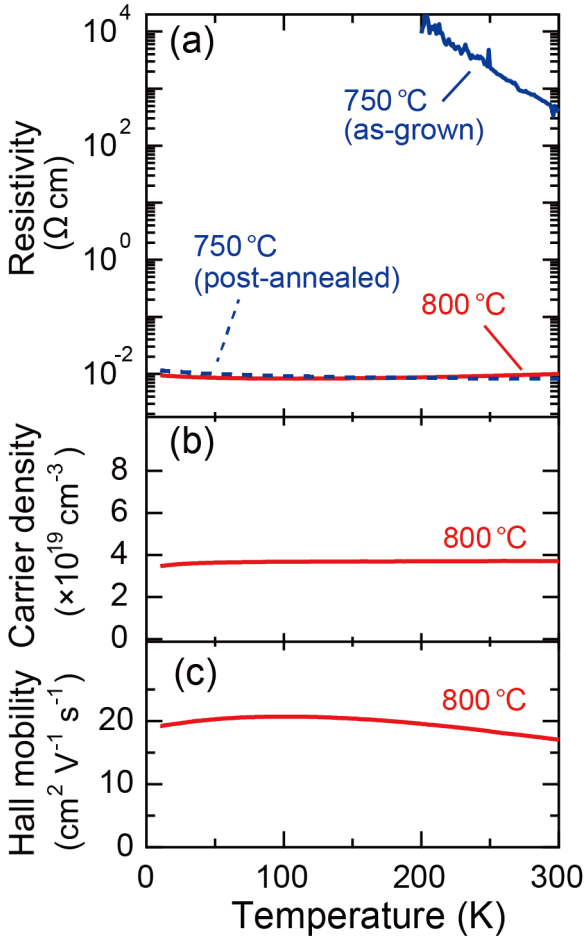

Figure 3.5 (a) Resistivity of anatase TaON epitaxial thin films plotted as functions of temperature. The dashed lines represent the data of the film grown at 750 °C and successively annealed at 800 °C under base pressure in the growth chamber. The resistivity of the film grown at 750 °C (as-grown) was measured by a two-probe method due to the high resistance. (b) Carrier density, and (c) Hall mobility of the films grown at 800 °C plotted as functions of temperature.

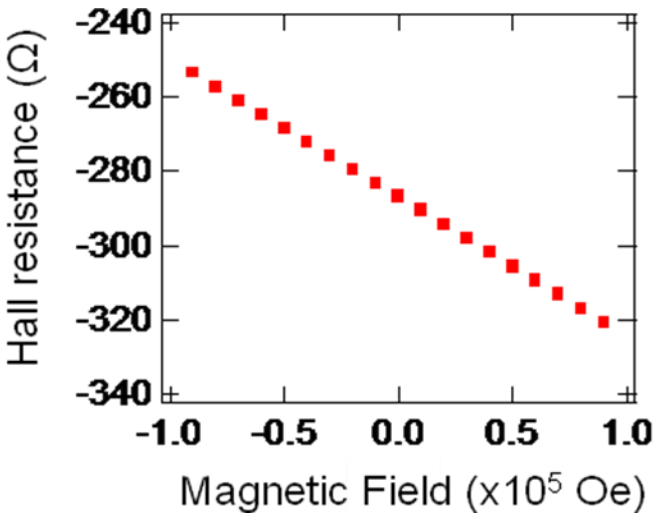

Figure 3.6 Hall resistance of anatase TaON epitaxial thin films grown at 800 °C plotted as functions of magnetic field.

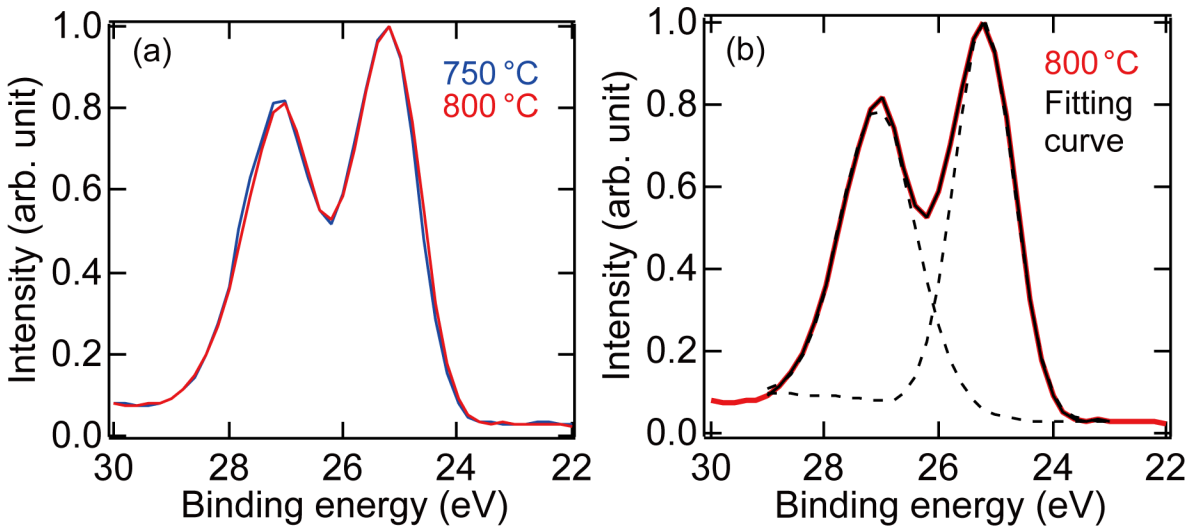

Figure 3.7 (a)Ta 4*f* core level XPS of the TaON thin films grown at 750 and 800 °C. (b) Result of curve fitting of the TaON thin film grown at 800 °C. Red and black solid lines represent the experimental data and the fitting curve (sum of two Gaussian curves), respectively. Dashed lines are each Gaussian component.

Figures 3.5b and 3.5c show temperature dependences of n_e and μ_H, respectively, for the anatase TaON thin film fabricated at T_S = 800 °C. n_e was almost constant at ~3.7×10^{19}

cm^{-3} irrespective of temperature, indicating that the anatase TaON film is categorized as a degenerated semiconductor. Remarkably, μ_H at 300 K was as high as ~17 $cm^2V^{-1}s^{-1}$, which is comparable to that of anatase TiO_2 single crystal [23], namely, ~17 $cm^2V^{-1}s^{-1}$. However, μ_H was almost temperature-independent in the whole temperature range (~20 $cm^2V^{-1}s^{-1}$), in sharp contrast to the anatase TiO_2 single crystal, in which μ_H is substantially enhanced at low temperatures where electron–phonon scattering is suppressed. Although the mechanism of the temperature independent μ_H in anatase TaON has not been fully understood yet, it is likely that the suppression of electron-phonon scattering at low temperatures is masked by predominant impurity scattering because the present films contain certain amounts of defects, such as anion vacancies and/or off-stoichiometry. Another possible explanation is that the electric transport is dominated by grain boundary scattering [89-91] caused by planar defects observed in the TEM images. Even in the case of anatase TiO_2, reduced samples with a high carrier density on the order of 10^{19} cm^{-3}, i.e., with a large number of oxygen vacancies, show similar suppression of μ_H at low temperatures [21]. On the other hand, Nb-doped TiO_2 films exhibit much higher mobility than the reduced ones [12], suggesting that μ_H of anatase TaON could be further enhanced by doping with an appropriate cation.

3.3.3 Optical properties of anatase TaON.

Finally, the optical properties of anatase TaON thin films will be briefly mentioned. Figure 3.8 shows the optical constants of the anatase TaON film grown at T_S = 750 °C determined by spectroscopic ellipsometry. The optical extinction coefficient, k, showed an abrupt increase around 2.3 eV. Assuming that anatase TaON is an indirect bandgap semiconductor like anatase TiO_2 [21] and baddeleyite TaON [92], E_g was determined to be 2.37 eV from $(\alpha h\nu)^{1/2}$ vs $h\nu$ plot (inset of Fig. 3.8), where absorption coefficient α was calculated from k ($\alpha = 4\pi k\lambda^{-1}$). This E_g value is comparable to those reported for anatase

$Mg_{0.05}Ta_{0.95}O_{1.15}N_{0.85}$ (2.2 eV) [66] and $Sc_{0.15}Ta_{0.85}O_{1.3}N_{0.7}$ (2.54 eV) [67]. The slight differences in the E_g values might be due to the difference in anion compositions or in lattice parameters. The refractive index, n, was approximately 3.0 in the visible light region, which is larger than that of Ta_2O_5 (~2.16) [63] and anatase TiO_2 (2.5-2.9) [16] in the same region. The higher n is explained by the stronger covalency of the Ta-N bond than Ta-O or Ti-O bonds, which tends to increase the polarizability [53].

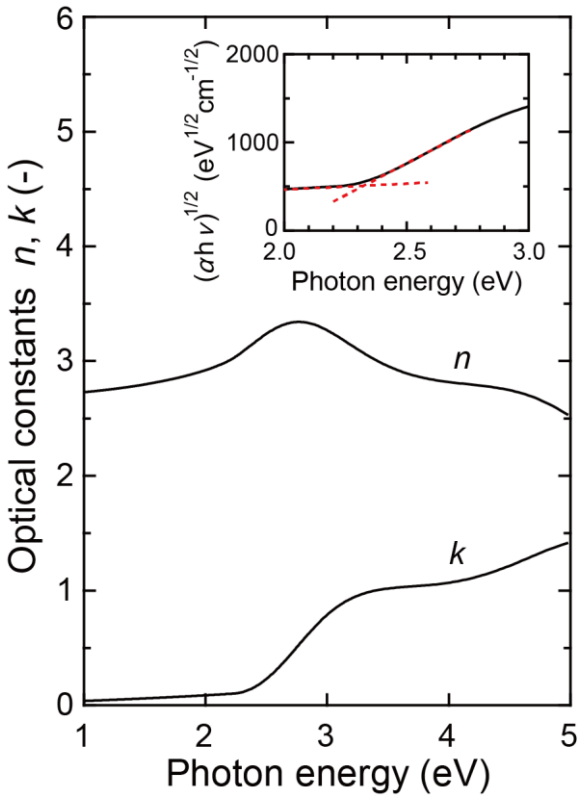

Figure 3.8 Refractive index n and extinction coefficient k of the anatase TaON thin film grown at T_S = 750 °C. (Inset) Optical bandgap of the anatase TaON thin film determined under an assumption that anatase TaON is an indirect transition semiconductor.

3.4 Summary

Phase-pure anatase TaON thin films were epitaxially synthesized on lattice-matched single crystalline substrates by using NPA-PLD. A high growth temperature and a balanced supply of oxygen and nitrogen are crucial for obtaining high-quality anatase TaON thin films. Electrical transport measurements revealed that the anatase TaON film grown at T_S = 800 °C or reduced by vacuum annealing exhibited good electrical conductivity of ~1 × 10^{-2} Ωcm and a temperature-independent *n*-type carrier density on the order of 10^{19} cm^{-3}, which are characteristic of degenerated semiconductors. The μ_H of ~17 $cm^2V^{-1}s^{-1}$ at 300 K is rather high for a *d*-electron based semiconductor and is comparable to that of anatase TiO_2. Development of effective dopants will be a key to improving the transport properties of anatase TaON. The anatase TaON thin films exhibited E_g of 2.37 eV and *n* of ~3.0 in the visible region.

My results demonstrated that epitaxial growth of oxynitride thin films is a very promising approach for investigating the physical properties of metal oxynitrides, which have been scarcely examined so far due to the difficulty in synthesizing single crystals.

Absorption in visible light and high μ_H are necessary for high efficiency photocatalyst. Compared to typical photocatalysts, such as anatase TiO_2 and baddeleyite TaON, anatase TaON is expected to show the higher efficiency because only anatase TaON among these three materials meets the both requests. Another unique property of anatase TaON is its high *n* value comparing with conventional oxide-based transparent electrode such as Sn:In_2O_3 (*n* ~2.0) and Nb:TiO_2 (*n* ~2.6). Development of a transparent electrode with high *n* is desirable because transparent conducting materials with wide lineup of *n* values are favorable to achieve refractive index matching, which is important for reducing reflection loss of incident light at the interface between transparent electrode and active layer. Therefore, I concluded that anatase TaON is promising as a photoelectrode or transparent electrode

material.

Chapter 4
Tuning of optical properties in solid-solution of anatase $(TiO_2)_x(TaON)_{1-x}$

4.1 Introduction

As described in Chapter.3, anatase TaON is promising for photoelectrodes and transparent electrodes. However, practical applications of anatase TaON needs further modification of its properties. Particularly, tuning its optical properties is important when applying it to photoelectrodes and transparent electrodes. In case of optoelectronic devices using conventional compound semiconductors, making solid-solution of materials with the same crystal structure and different optical properties is a well-established way for this purpose [32]. It is noteworthy that anatase TaON and anatase TiO_2 have the same crystal structure and different optical properties as summarized in Table 4.1. Thus, it is expected that optical properties can be tuned between the values of TaON and TiO_2 by making the solid-solution thin films of anatase $(TiO_2)_x(TaON)_{1-x}$ (TTON). However, there are no reports of complete solid-solution in anatase TTON, but only the bulk synthesis in the range of $0.52 \leq x \leq 0.87$ [93] and theoretical calculation [94] have been reported. This is mainly due to the instability of anatase structure and difficulty in controlling nitrogen composition. To overcome this problem, I tried to synthesize the solid-solution thin films of anatase TTON with various chemical composition x by using epitaxial stabilization same as the anatase TaON. Furthermore, wide tunability of their optical properties by changing x was demonstrated.

Table 4.1 Optical constants, crystal structure, and lattice constants of anatase TiO_2 and TaON

	E_g (eV)	n (-)	Crystal structure	a-axis (nm)	c-axis (nm)
TiO_2	3.2 [21]	2.6 [16]	Anatase	0.3785	0.9514
TaON	2.37	3.1	Anatase	0.388	1.031

4.2 Experimental procedure

Anatase TTON epitaxial thin films were grown on $(LaAlO_3)_{0.3}(SrAl_{0.5}Ta_{0.5}O_3)_{0.7}$ (100) (LSAT, a/2= 3.868 Å) single crystalline substrate by using nitrogen plasma assisted pulsed laser deposition (NPA-PLD). Oxide ceramic targets with different Ti to Ta ratio, $Ti_xTa_{1-x}O_y$, which were sintered from Ta_2O_5 powder (99.99% purity) and TiO_2 powder (99.99% purity) at 1400°C for 15 h in air, were used for controlling cation compositions in the films. Pulsed laser beams from a KrF excimer laser (λ=248 nm) were focused onto the $Ti_xTa_{1-x}O_y$ target. The fluence and repetition rate of the excimer laser were adjusted so as to control the deposition rate at ~13 − ~70 nm/h. Substrate temperature (T_S) was set at 750°C by infrared lamp heating. The depositions were conducted under partial O_2 gas pressure of 0 − 1×10^{-5} Torr and N_2 gas pressure of 1×10^{-5} Torr. N_2 gas was activated into radicals by a radio-frequency wave (RF) plasma source (SVT Associate, Model 4.5") with output power of 250 W. Typical film thicknesses were ~30 − 55 nm evaluated by a stylus profiler. Crystal structures of the films were examined by X-ray diffraction (XRD) measurements using Cu-Kα radiation and four-axis diffractometer with two-dimensional detector (Bruker AXS, d8 discover with GADDS). The nitrogen contents were evaluated by nuclear reaction analysis (NRA) using a $^{15}N(p, \alpha\gamma)^{12}C$ resonance reaction at 898 keV, which included an experimental error of ~20% due to the small sample thickness and the instability of the energy of proton beam. The oxygen content was calculated from the nitrogen amount assuming charge

neutrality. Optical constants of the anatase TTON films were determined by spectroscopic ellipsometry (J. A. Woolam, M-2000U) in a spectral range of 1-4 eV. A series of ellipsometric spectra obtained at incident/reflection angles from 50° to 80° with 5° step were analyzed by using a model consisting of a substrate and a single-layer film, which contains gradient of refractive index along the depth direction. The dispersion function of the TTON film was modeled as a sum of Tauc–Lorentz and Lorentz dispersion functions. Valence band spectra of TTON were examined by X-ray photoelectron spectroscopy. Electrical resistivity (ρ), carrier electron density (n_e), and Hall mobility (μ_H) were determined by van der Pauw method with Ag electrodes. A physical property measurement system (Quantum Design, model 6000) was used to control the external magnetic field between −9 T and 9 T.

4.3. Results and discussion

4.3.1 Synthesis of anatase $(TiO_2)_x(TaON)_{1-x}$: TTON epitaxial thin films

In order to control the nitrogen amount in the TTON film by oxygen partial pressure ($p(O_2)$: $0 - 1\times10^{-5}$ Torr), I first investigated the relation between nitrogen amount and growth of the phase pure anatase TTON. Concretely, I fabricated the TTON films with a cation ratio of x=0.5 at various oxygen partial pressure. Figure 4.1a compares θ-2θ XRD patterns of the films grown at various oxygen partial pressure. Phase pure TTON could be grown with oxygen partial pressure $p(O_2)$= 1×10^{-6} and 3×10^{-6} Torr. When oxygen partial pressure was higher than $p(O_2)$ = 1×10^{-5} Torr, oxide impurity Ta_2O_5 appeared. On the other hand, the lower oxygen partial pressure ($p(O_2)$ = 0 Torr) resulted in the appearance of nitride impurity $Ti_xTa_{1-x}N$. Compared to anatase TaON, anatase TTON needed more supply of oxygen to

suppress the appearance of impurities because TTON contains a larger amount of oxygen than TaON. I also conducted asymmetrical XRD measurements on the phase pure TTON films and confirmed the epitaxial relationships $(001)_{TTON} \parallel (001)_{LSAT}$ and $[100]_{TTON} \parallel [100]_{LSAT}$, same as the anatase TaON. The φ-scan plot of the 101 diffraction (Fig. 4.1b) revealed four-fold rotational symmetry, being consistent with the epitaxial relationship.

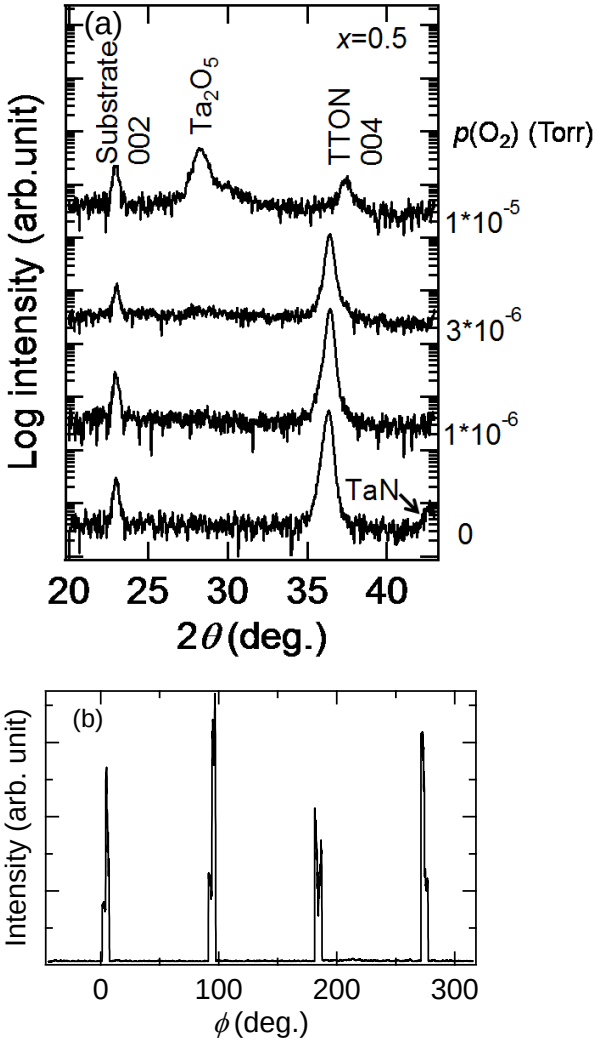

Figure 4.1 (a) θ-2θ XRD patterns of the TTON films with x=0.5 grown on LSAT substrates at various $p(O_2)$. (b) φ-scan plot of 101 diffraction from the anatase TTON film. φ = 0° was set parallel to the <100> direction of the LSAT substrate.

Nitrogen amounts of the film grown at various oxygen partial pressure were investigated by NRA. The evaluated compositional ratios of N/Ta are plotted in Fig. 4.2a. As can be seen, the nitrogen amount was successfully controlled by oxygen partial pressure, indicating that the nitrogen supply to the thin film became low, in a relative sense, by increasing the oxygen partial pressure. The phase pure TTON films showed the N/Ta ratio close to stoichiometry ($p(O_2)$= 1×10^{-6} and 3×10^{-6} Torr). On the other hand, the N/Ta ratio at $p(O_2)$ = 0 and 1×10^{-5} Torr showed large deviation from stoichiometry. This might be a reason why oxide and nitride impurities appeared at very high or very low $p(O_2)$. Therefore, to adjust nitrogen amount with oxygen partial pressure was crucial to obtain phase pure TTON. The nitrogen amount could also be controlled by the growth rate of TTON thin film, because oxygen was supplied from not only O_2 gas but also the plume from oxide ceramic target, $Ti_xTa_{1-x}O_y$. I systematically changed the growth rate by controlling the repetition rate of KrF excimer laser (4, 8, and 12 Hz) and confirmed this hypothesis: Increase of the growth rate monotonically decreased the nitrogen amount (Fig. 4.2b). This result suggests that the increase of the growth rate played the same role as the increase of oxygen partial pressure.

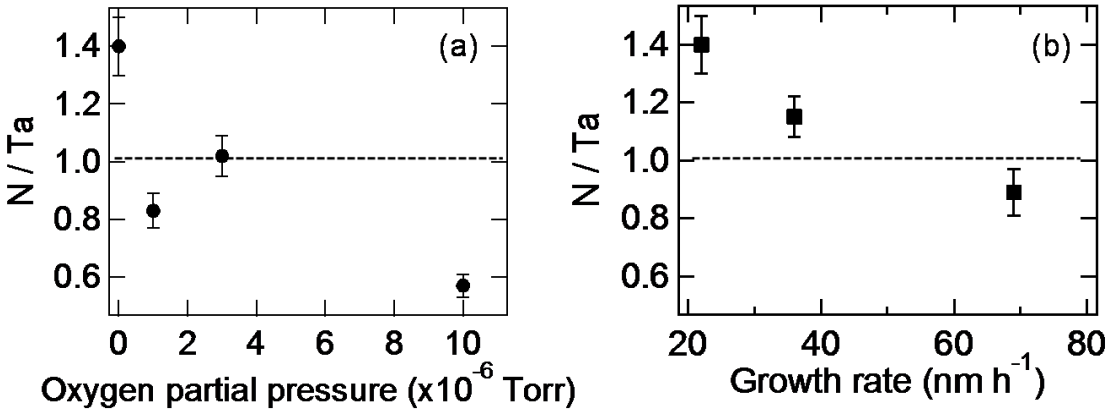

Figure 4.2 Nitrogen and tantalum ratio of anatase TTON epitaxial thin films grown at (a) various oxygen partial pressures and (b) various growth rate. Value of 1.0 corresponds to the stoichiometry of TTON (dashed lines).

Next, synthesis of TTON thin film with various x values (x=0.1, 0.3, 0.5, 0.7 and 0.9) was carried out. Similar to TTON with x=0.5, the oxygen partial pressure was optimized for each x value to obtain phase pure TTON with stoichiometric nitrogen amount. The deposition rate was set at ~13 − ~22 nm/h. For each x value, the oxygen partial pressure determined the success or failure in the growth of phase pure anatase TTON similar to TTON with x=0.5. As a result of the optimization, phase pure TTON films with any x values were obtained as shown in Fig. 4.3, which indicated no signature of phase separation to anatase TiO_2 and TaON and segregation of impurity phases. Focusing on the TTON peak positions in Fig. 4.3, one may notice that the peak was shifted to larger angle side with increasing x. In Fig. 4.4, the lattice constants of the anatase TTON calculated from the individual XRD

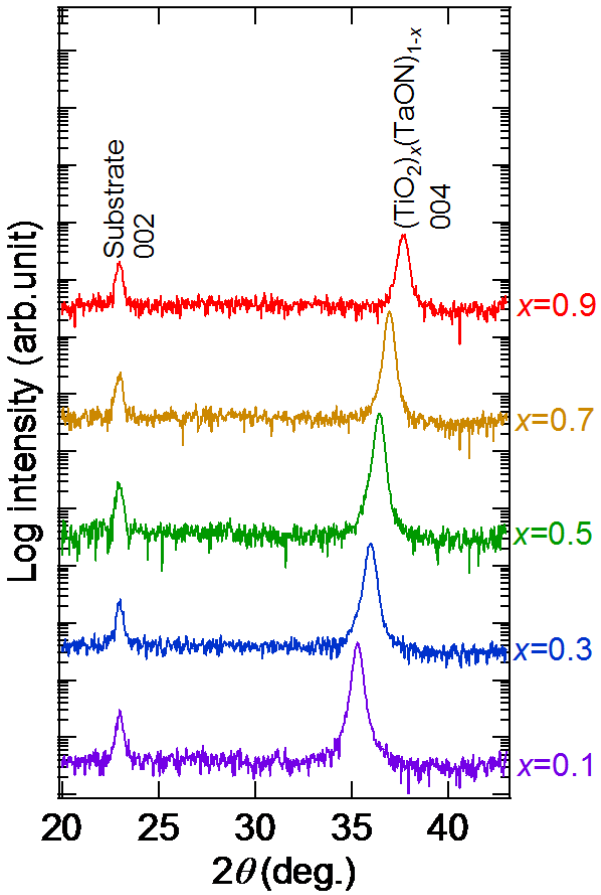

Figure 4.3 θ-2θ XRD patterns of the TTON films grown on LSAT substrate with various x values.

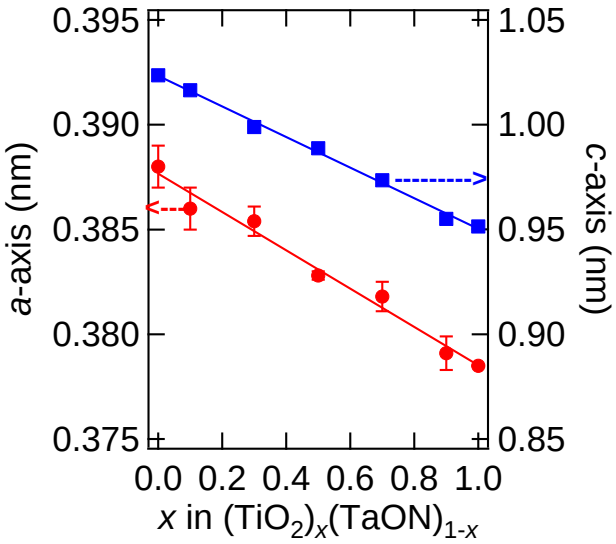

Figure 4.4 *a*-axis (red circles) and *c*-axis (blue squares) lattice constants of anatase TTON epitaxial thin films plotted as *x* value in TTON.

patterns were plotted as a function of *x*. Both in-plane (*a*-axis) and out-of-plane (*c*-axis) lattice parameters almost linearly decreased, as *x* increased, in accordance with Vegard's law. Judging from the phase pure growth of TTON and the almost linear change of lattice constants, I concluded that complete solid-solution of anatase TTON thin films were obtained.

4.3.2 Optical properties of anatase TTON

Next, extinction coefficient *k* and refractive index *n* of the TTON thin films were determined by spectroscopic ellipsometry. The obtained extinction coefficient of the TTON film (*x*=0.1, 0.3, 0.5, 0.7, 0.9) are shown in Fig. 4.5. In visible light region, extinction coefficient decreased as *x* increased. Furthermore, the spectra shape drastically changed around *x*=0.7, which possibly reflects the change in nature of N 2*p* orbital in the valence band, hybridized with O 2*p* orbital or localized. Actually, the nature of N 2*p* orbital in anatase $TiO_{2-w}N_w$ is predicted to change around *w*~0.3 by calculation [95]. Band gap E_g calculated

from $(\alpha h\nu)^{1/2}$ vs $h\nu$ plot systematically changed from visible light region (~2.4 eV) to ultraviolet region (> 3.2 eV) in accordance with *x* (Fig. 4.6a). This implies that the optical properties of TTON could be tuned in a wide range by adjusting *x*, which can cover the applications from visible light active photoelectrode to transparent electrode. The refractive index of TTON is shown in Fig. 4.5, indicating that the refractive index in visible light region decreased from 3.2 (TaON side) to 2.7 (TiO_2 side) with increasing *x* (Fig. 4.6b). In conclusion, thus, precise controllability of band gap and refractive index was confirmed in the TTON solid-solution, as expected.

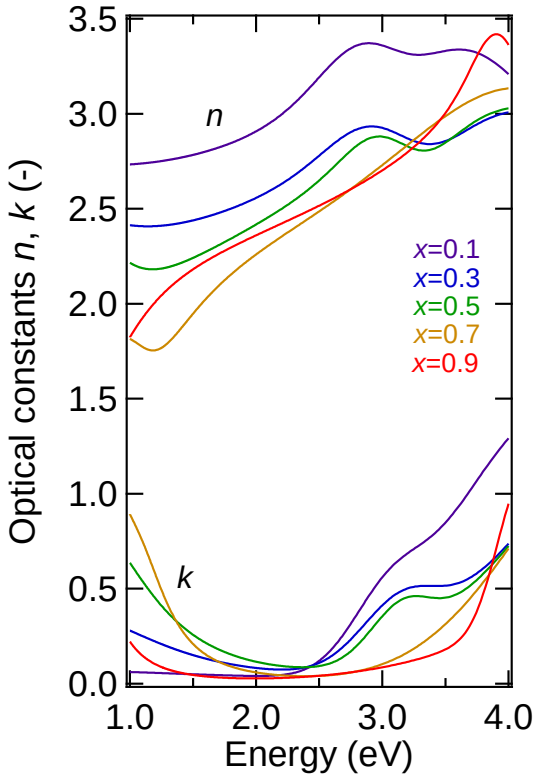

Figure 4.5 Refractive index *n* and extinction coefficient *k* of the anatase TTON thin films with *x* = 0.1, 0.3, 0.5, 0.7, and 0.9.

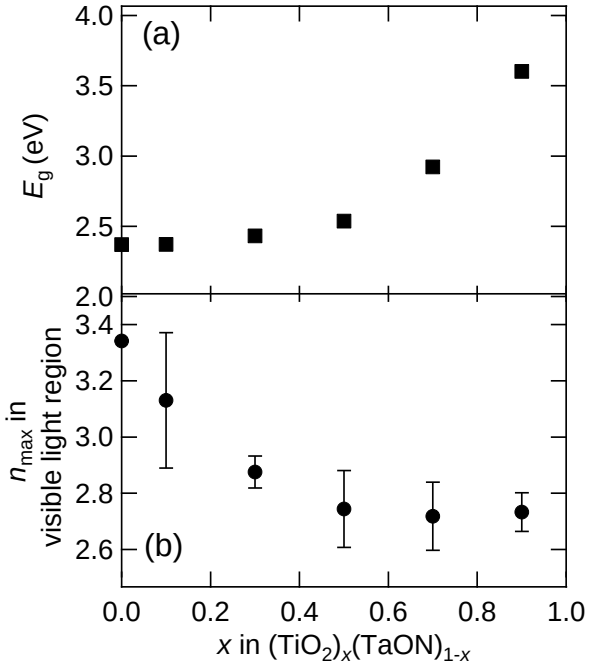

Figure 4.6 Band gap and maximum refractive index value in visible light region of anatase TTON with various *x* values. Error bars in *n* represent the gradients of *n* along the depth direction.

The tendencies of E_g can be explained as follows. In most of oxynitrides, the valence band top consists of N 2*p* orbital, which is shallower than O 2*p* orbital due to smaller electronegativity of nitrogen than oxygen. When *x* increases, contribution from N 2*p* orbital decreases and the valence band top is pushed down, resulting in the increased E_g (Fig. 4.7). Similar band gap narrowing was observed in the $Ti_{0.5}Ta_{0.5}O_yN_z$ films with different nitrogen amounts *z*. The TTON thin film with $z = 0$ was fabricated without introduction of nitrogen gas. As shown in Fig. 4.8, as the nitrogen amount increased, the absorption in visible light region was enhanced and the band gap became narrower. This result supported the above-mentioned consideration that shallower N 2*p* orbital contributed to the band gap narrowing. In case of TaON, not only the N 2*p* orbital but also hybridization among N 2*p*, O 2*p* and Ta 5*d* orbital at the valence band would contribute to the decreased band gap due to widening of the band width [61]. Thus, the band width of the valence band would become

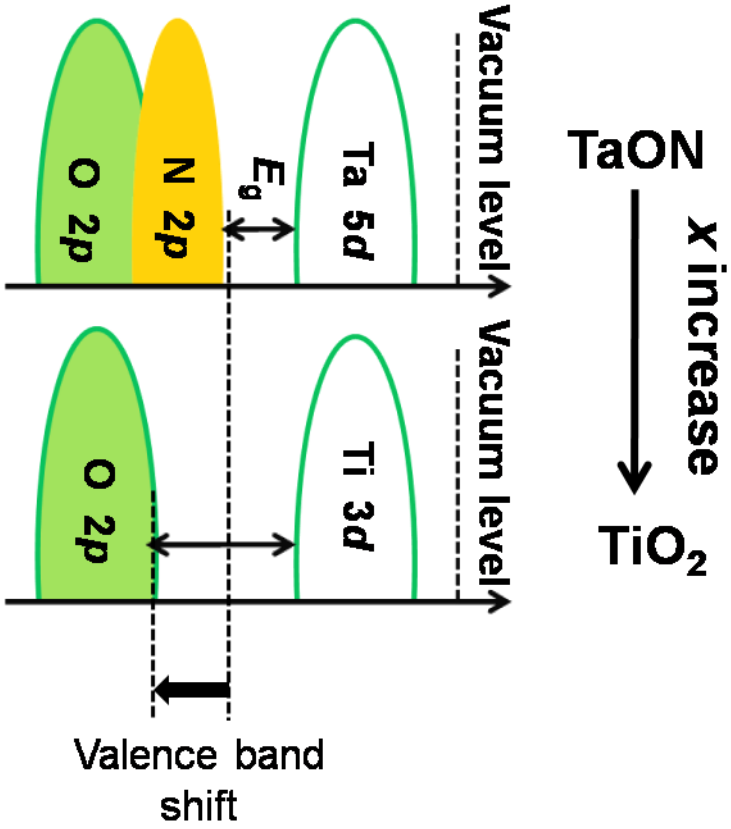

Figure 4.7 Schematic diagram of energy band of TiO_2 and TaON.

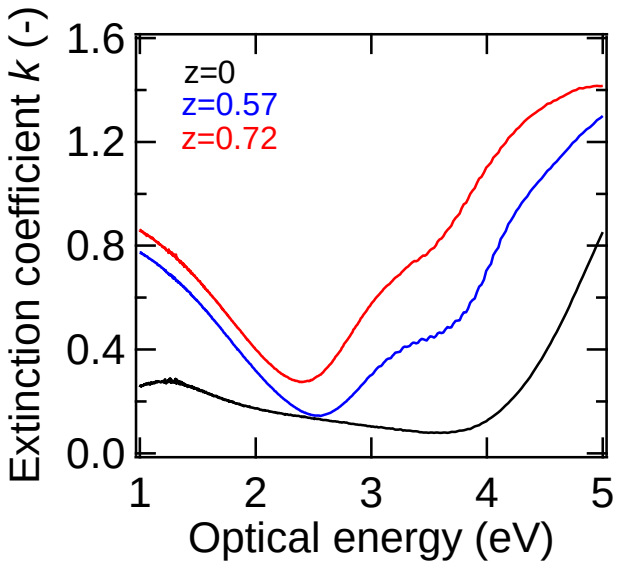

Figure 4.8 Extinction coefficient *k* of the anatase TTON thin films with *x* =0.5 and various nitrogen amount, *z*.

smaller when x increases. This change of band width was confirmed by XPS valence band spectra (Fig. 4.9). A structure located from ~2 eV to ~10 eV corresponds to the valence band. Obviously, the valence band width became narrower as the nitrogen and tantalum amount decreased, which suggests decreased hybridization among N 2*p*, O 2*p* and Ta 5*d* orbital. In this study, thus, band gap narrowing by sallower N 2*p* orbital and hybridization at the valence band were confirmed experimentally. Such variation of electronic structure is also considered to be responsible for the change in refractive index n with composition. Refractive index n of a solid generally decreases with decreasing bond covalency. Since *M*-O bonds have smaller covalency than *M*-N bonds, n of the TTON films decreases with an increase of x.

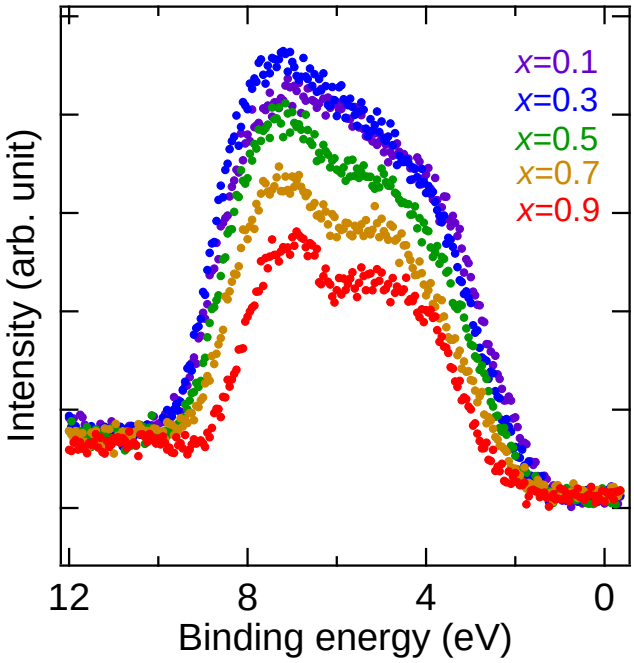

Figure 4.9 Valence-band spectra of anatase TTON thin films with x = 0.1, 0.3, 0.5, 0.7, and 0.9.

4.3.3 Transport properties of anatase TTON

Transport properties of the TTON thin films were briefly described. Figure 4.10 plots resistivity, carrier density and Hall mobility values of the anatase TTON films

fabricated at T_S = 750 °C as functions of x. The Hall measurements revealed that electrons carried charges in any x values (n-type semiconductor). The resistivity decreased by two orders magnitude as x increased. This change mainly originated from the increase of carrier density, which also increased by two orders of magnitude with x. Considering the x dependence of carrier density and the n-type conduction, the carrier electrons are thought to be originated from reduced titanium ions, Ti^{3+} and Ti^{2+}, which are usually seen in anatase TiO_2 grown in a reductive condition [96]. The growth condition of TTON used in this study was very reductive because of higher growth temperature and less oxygen partial pressure than those reported previously [12], supporting the above hypothesis about the carrier source.

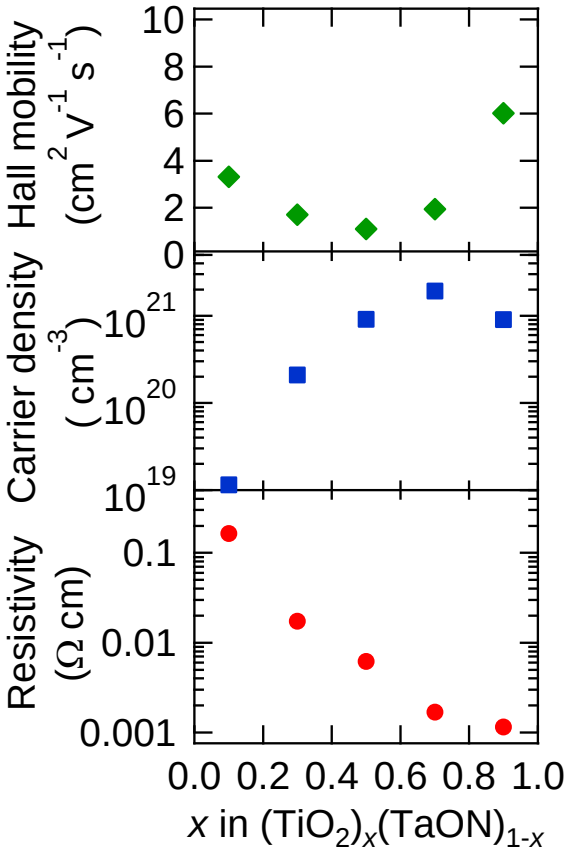

Figure 4.10 Resistivity (red circles), carrier density (blue squares), and Hall mobility (green diamonds) of anatase TTON epitaxial thin films plotted as functions of x in TTON.

The increase in carrier density and the decrease in resistivity in accordance with x might reflect increase of Ti^{3+} with x. On the other hand, the Hall mobility of TTON showed a minimum around x=0.5. However, I speculate that the Hall mobility of TTON can be further enhanced by optimization of the growth parameter, which would decrease the amount Ti^{3+} as an impurity scattering site. Further improvement of transport properties seems to be still needed towards practical application of anatase TTON.

4.4 Summary

Complete solid-solution in anatase TTON was achieved by NPA-PLD on lattice matched substrate. Considering the fact that the appearance of oxide or nitride impurity was suppressed by controlling nitrogen amount with oxygen partial pressure, adjustment of nitrogen amount was crucial for obtaining phase pure anatase TTON. Both band gap and refractive index were successfully tuned between the values of anatase TaON and anatase TiO_2 by the composition x of the solid-solution system. Both shallower N 2*p* orbital than O 2*p* orbital and hybridization among N 2*p*, O 2*p* and Ta 5*d* orbital were attributable to the systematic variation of band gap, as predicted by calculation [61, 95]. This controllability of optical properties is advantageous for wide applications from visible light active photoelectrodes and transparent electrodes with optimized refractive index.

Chapter 5
Carrier doping to anatase TaON

5.1 Introduction

When applying anatase TaON to transparent electrodes, tuning of not only its optical properties but also its transport properties are needed. Transparent electrodes are required to have low resistivity of $\rho < 1\times10^{-3}$ Ωcm [6]. However, reduced anatase TaON showed higher resistivity (ρ ~1×10^{-2} Ωcm) although anatase TaON indicated high Hall mobility (μ_H ~ 17 $cm^2V^{-1}s^{-1}$) comparable to anatase TiO_2. This is mainly due to the lower carrier density ($n_e < 5\times10^{19}$ cm^{-3}) than those of typical transparent electrode materials ($n_e > 1\times10^{20}$ cm^{-3}). Therefore, carrier doping method with anatase TaON has to be developed.

I took two approaches for carrier doping, substitution and insertion of cations. Cation substitution, which is widely used in oxide semiconductors to introduce carriers into them as described in Chapter.1, was attempted by W^{6+}-substituted for Ta^{5+} as in the case of Nb^{5+}- or Ta^{5+}-substitution for Ti^{4+} in anatase TiO_2 [12, 39]. On the other hand, soft chemical Li insertion was also adopted as carrier doping method [97]. There are several reports of soft chemical Li insertion to bulk polycrystalline anatase structure with *n*-butyllithium solution [66, 98]. However, transport properties of W- or Li-doped anatase TaON had never been investigated because of the lack of single crystalline samples.

In this study, I synthesized W- and Li-doped anatase TaON thin films by nitrogen plasma assisted pulsed laser deposition (NPA-PLD) and soft chemical Li insertion to anatase TaON thin films fabricated by NPA-PLD with *n*-butyllithium solution, respectively. I investigated the transport properties of the obtained thin films.

5.2 Experimental procedure

W-doped anatase TaON epitaxial thin films were grown on $(LaAlO_3)_{0.3}(SrAl_{0.5}Ta_{0.5}O_3)_{0.7}$ (100) (LSAT, $a/2$= 3.868 Å) single crystal substrate by using NPA-PLD. Oxide ceramic targets, $W_{0.05}Ta_{0.95}O_y$, which were sintered from Ta_2O_5 powder (99.99% purity) and WO_3 powder (99.99% purity) at 1000°C for 18 h in air were used. Lower sintering temperature than Ta_2O_5 target was expected to prevent tungsten vaporizing because tungsten has a smaller vapor pressure than tantalum. Pulsed laser from a KrF excimer laser (λ=248 nm) was focused onto the $W_{0.05}Ta_{0.95}O_y$ target. The substrate temperature (T_S) was set at 800°C by infrared lamp heating. Output power of a radio-frequency wave (RF) plasma source (SVT Associate, Model 4.5") was set to 350 W. The other conditions of the fabrication were the same as those of anatase TaON (Chapter.3). Typical film thicknesses were ~50 nm evaluated by a stylus profiler.

Anatase TaON thin films as precursor of Li insertion reaction were fabricated at 750°C by NPA-PLD. The film growth conditions are the same as those described in Chapter.3. The thin films were reacted with *n*-butyllithium in hexane solutions (Sigma-Aldrich) at room temperature or 60°C for 6 hours by dipping a crystal in an *n*-butyllithium solution, as reported in Li-doped anatase TiO_2 [98]. The reacted thin films were washed with hexane and then covered with laminate films or greases to prevent exposure to air. 1.6 M, 1.6×10^{-2} M, and 1.6×10^{-4} M *n*-butyllithium solutions were used to investigate the effect of *n*-butyllithium concentration. In addition, I carried out Li insertion to anatase TaON thin films fabricated at 800°C with more anion vacancy than that fabricated at 750°C to investigate the effect of anion vacancy in the precursor films on Li insertion. All procedures for Li insertion were performed in a glove box under an inert N_2 gas atmosphere.

Crystal structures of the films were examined by X-ray diffraction (XRD) measurements using Cu-Kα radiation and a four-axis diffractometer (Bruker AXS, d8

discover). Surface morphology of the films reacted with the *n*-butyllithium solution was investigated by atomic force microscope (AFM). The presence tungsten in the W-doped anatase TaON films was confirmed by an energy dispersive X-ray spectroscopy installed in a scanning electron microscope (SEM-EDX). The electron accelerating voltage was set at 15.0 keV to separate the tungsten and tantalum peaks, because the two peaks in low energy region (~1.7 keV) were considerably overlapped with each other. Lithium contents in the Li-doped anatase TaON films were examined by secondary ion mass spectrometry (SIMS), within experimental errors of ~40%. The Li-doped TaON thin film prepared by ion implantation was used as a standard sample for determining lithium amounts. The resistance values during the reaction with the *n*-butyllithium solution were measured by two-probe method with circuit testers. Electrical resistivity (ρ), carrier electron density (n_e), and Hall mobility (μ_H) of the doped anatase TaON films were determined by van der Pauw method with Au/Ti or Ag electrodes. A physical property measurement system (Quantum Design, model 6000) was used to control the sample temperature between 10 and 300 K and the external magnetic field between −9 T and 9 T.

5.3 Results and discussion

5.3.1 W-doped anatase TaON

θ-2θ XRD pattern of the film fabricated by $W_{0.05}Ta_{0.95}O_y$ target is shown in Fig. 5.1. The film clearly shows an anatase TaON 004 diffraction peak without any impurity peaks. The presence of W in the film was confirmed by SEM-EDX, although quantitative determination of W was difficult because of weak intensity of W peak and partial overlap with Ta peak. These results indicate that W-doped anatase TaON thin film was successfully

obtained.

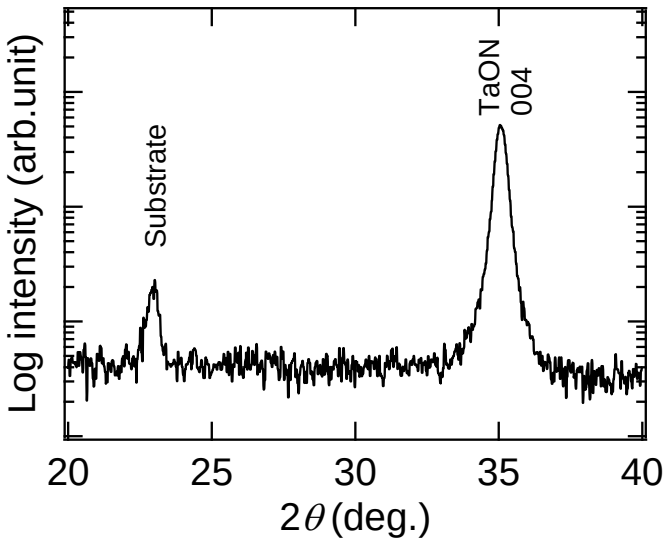

Figure 5.1 θ-2θ XRD patterns of W-doped TaON films grown on LSAT substrates at T_S=800 °C.

Resistivity and carrier density at 300 K were compared between pure and W-doped anatase TaON, shown in Fig. 5.2. In case of W-doped anatase TiO_2 ($W_{0.05}Ti_{0.95}O_2$), carriers were introduced by W substitution: Larger carrier density in $W_{0.05}Ti_{0.95}O_2$ (n_e~2.0×10^{20} cm^{-3}) than non-doped anatase TiO_2 (n_e~4.5×10^{18} cm^{-3}) [40]. In contrast, the carrier density of anatase TaON did not change at all by W substitution (n_e~4.0×10^{19} cm^{-3}), and, thus, the

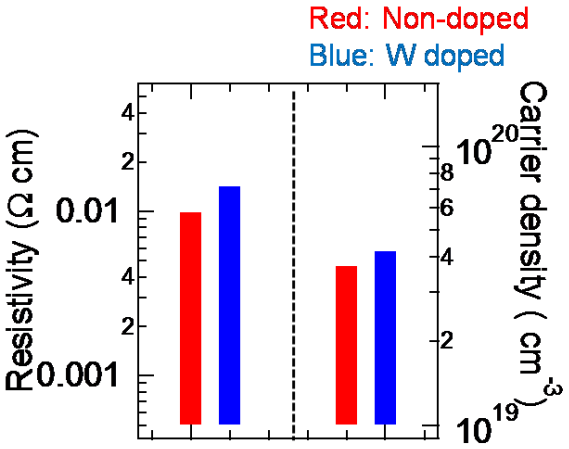

Figure 5.2 Resistivity, and carrier density of non-doped (red charts) and W-doped (blue charts) anatase TaON epitaxial thin films.

resistivity of W-doped anatase TaON (ρ~1.4×10^{-2} Ωcm) was almost the same as that of non-doped anatase TaON (ρ~1.0×10^{-2} Ωcm). These results imply that W did not act as an electron donor in anatase TaON, probably because the W-substitution was compensated by substitution of N^{3-} for O^{2-} occurring during the film growth. Therefore, carrier doping process after the film growth process (i.e. after O/N ratio is fixed) might be effective to avoid the charge compensation.

5.3.2 Li inserted anatase TaON

A θ-2θ XRD pattern of the films after the reaction with 1.6 M *n*-butyllithium solution at 60°C is shown in Fig. 5.3. By comparing the XRD pattern with that of as-grown

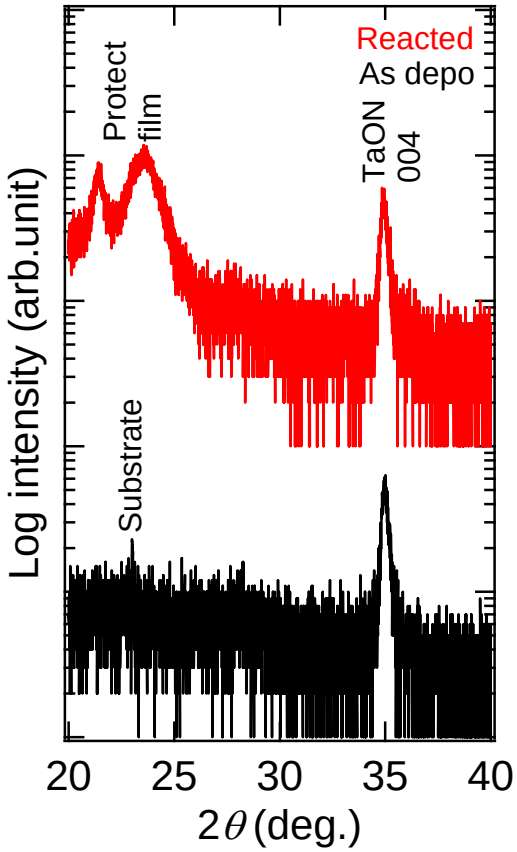

Figure 5.3 θ-2θ XRD patterns of TaON film reacted with 1.6 M *n*-butyllithium solution (red line) and as-grown TaON film (black line).

film, no decomposition of anatase TaON was confirmed. Surface morphologies examined by AFM also showed no obvious change after the reaction, such an appearance of segregation and an increase of the root-mean-square roughness, which was ~0.96 nm (as-grown) and ~1.2 nm (after the reaction) (Fig. 5.4). These results indicated that Li insertion with *n*-butyllithium solution was enough soft for anatase TaON thin films not to decompose the anatase structure.

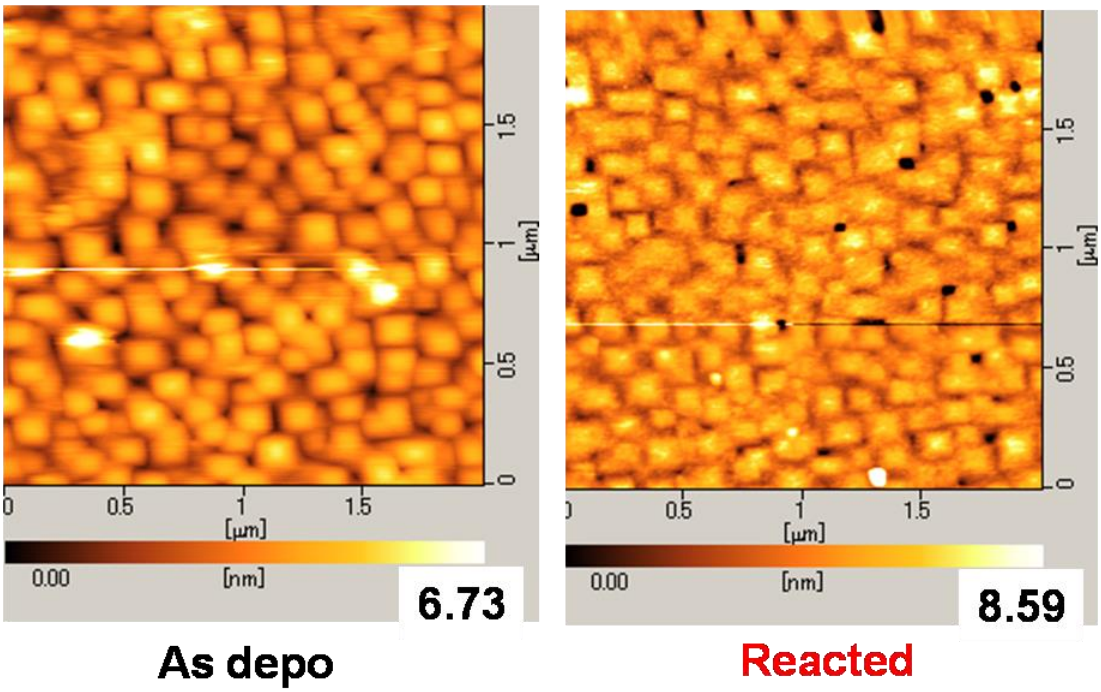

Figure 5.4 AFM images of anatase TaON thin film reacted with 1.6 M *n*-butyllithium solution (right side image) and as-grown TaON thin film (left side image).

From Fig. 5.5, it is evident that the peak position of anatase TaON 004 diffraction shifted to lower angle side after the reaction. Notably, the out-of-plane lattice parameters of anatase TaON changed from 10.262 to 10.272 Å, which correspond to 0.10% expansion. This expansion suggests that Li was successfully inserted to interstitial sites of anatase TaON similar to bulk polycrystalline anatase TiO_2 and TaON [66, 98]. Indeed, secondary ion mass spectrometry confirmed the existence of Li inside the film, of which amount was controllable over about four orders of magnitude by changing the concentration of *n*-butyllithium solution

(Fig. 5.6). The depth profile of Li exhibited a gradient of Li amount inside the film, as shown in Fig. 5.7. Li diffusion from the outside solution to the thin films might cause this gradient and there still remains room for improvement of uniformity by optimization of the reaction conditions such reaction time. On the other hand, in-plane Li distribution parallel to the surface of the thin film is almost uniform, which was confirmed by the SIMS measurements at multiple points. Hereafter I use the Li amount calculated by averaging the Li concentration profile along the depth direction as “Li amount”.

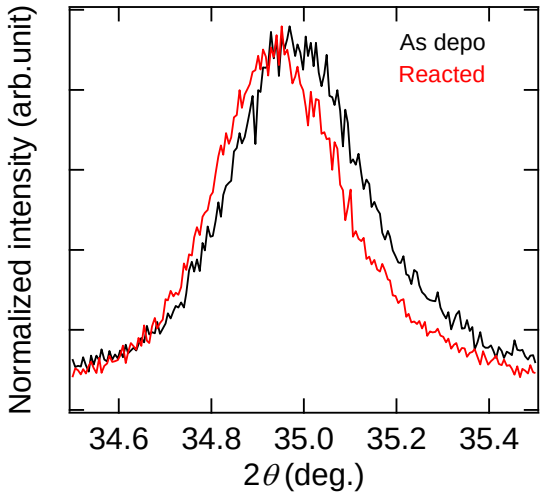

Figure 5.5 Close-up view of θ-2θ XRD patterns near 004 diffraction of anatase TaON film reacted with 1.6 M *n*-butyllithium solution (red line) and as-grown film (black line).

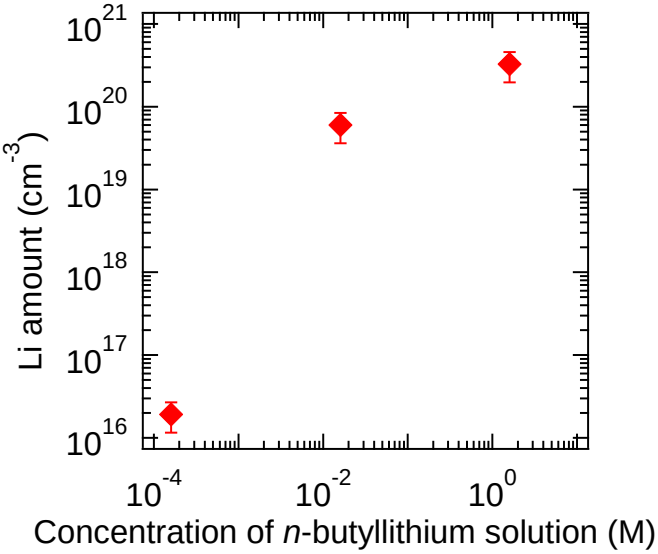

Figure 5.6 Li amount of anatase TaON films reacted with *n*-butyllithium solution plotted as functions of the concentration of *n*-butyllithium solution.

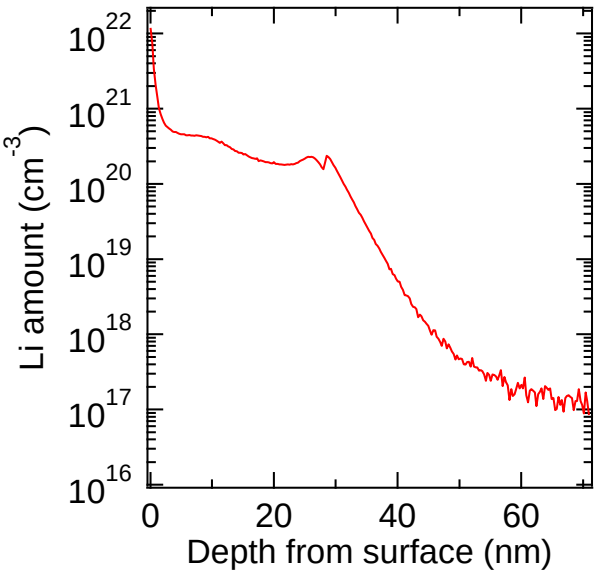

Figure 5.7 Li amount distribution along depth direction of anatase TaON film reacted with 1.6 M *n*-butyllithium solution. The region at ~0-30 nm corresponds to region of the anatase TaON thin film.

Next, I investigated the transport properties of Li-doped anatase TaON as functions of the Li concentration of *n*-butyllithium solution. Figure 5.8 indicates the resistance values of anatase TaON thin films (substrate temperature 750°C) measured during the reaction with the 1.6 M *n*-butyllithium solution at room temperature or 60°C. As shown in the figure, the resistance substantially decreased by the reaction with *n*-butyllithium solution. Considering the results of the composition analysis, the decrease of resistance implied that inserted Li generated conduction electrons as expected. The decrease of resistance was promoted at 60°C, suggesting that higher reaction temperature enhanced the Li insertion.

To examine the effect of *n*-butyllithium concentration, transport properties of the Li-doped anatase TaON thin films reacted with various concentration of *n*-butyllithium solution at 60°C were also investigated. As shown in Fig. 5.9, n_e increased with increasing the concentration of the *n*-butyllithium solution. The n_e values at the 1.6×10^{-2} and 1.6 M *n*-butyllithium solution were comparable to the concentrations of Li in the film shown in Fig.

5.6, which suggests that each inserted Li is ionized to Li^+ to release an electron with high efficiency. I also note that much larger n_e at the 1.6×10^{-4} M *n*-butyllithium solution than the Li amount was caused by the carriers generated from anion vacancy. Notably, the anatase TaON films fabricated at 750°C and reacted with 1.6×10^{-2} M *n*-butyllithium solution exhibited higher Hall mobility (μ_H ~20 $cm^2V^{-1}s^{-1}$) than anion-deficient anatase TaON with similar n_e prepared by annealing in vacuum (μ_H ~9 $cm^2V^{-1}s^{-1}$). This difference in μ_H suggests that Li works as a weaker impurity scattering center than anion vacancy. I further focused the transport properties of the Li-doped anatase TaON thin film reacted with 1.6×10^{-2} M *n*-butyllithium solution. Figure 5.10 compares ρ values of this Li-doped anatase TaON thin film with that of as-grown thin film as functions of temperature. The former showed low ρ at 300 K (~2×10^{-3} Ωcm) and metallic temperature dependence ($d\rho/dT > 0$) down to ~50 K, whereas the latter showed a five orders of magnitude higher ρ of 10^2 Ωcm order at 300 K and semiconducting temperature dependence ($d\rho/dT < 0$).

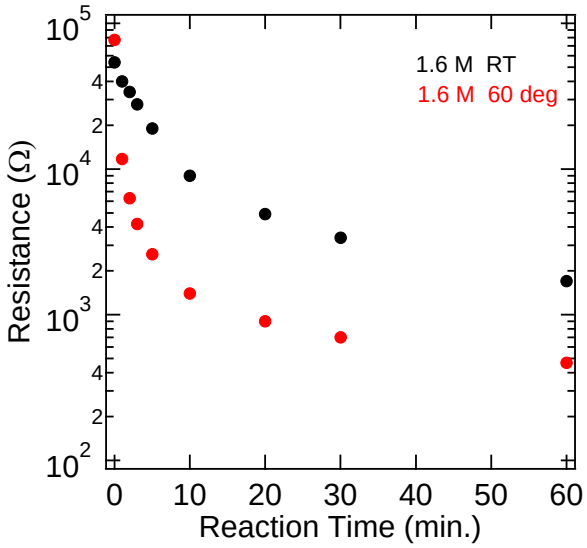

Figure 5.8 Resistance of anatase TaON thin films reacted with 1.6 M *n*-butyllithium solution at room temperature (black marks) and 60 °C (red marks) plotted as functions of reaction time.

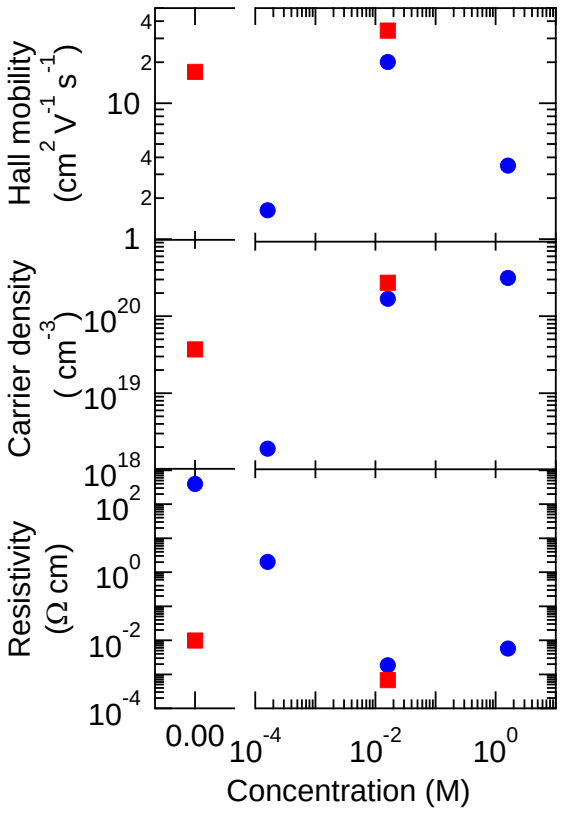

Figure 5.9 Transport properties of Li doped anatase TaON thin films plotted as functions of the concentration of *n*-butyllithium solution (0.00 M denotes to the data of precursor film). Circles and squares represent the data for the films grown at T_s = 750 and 800°C, respectively.

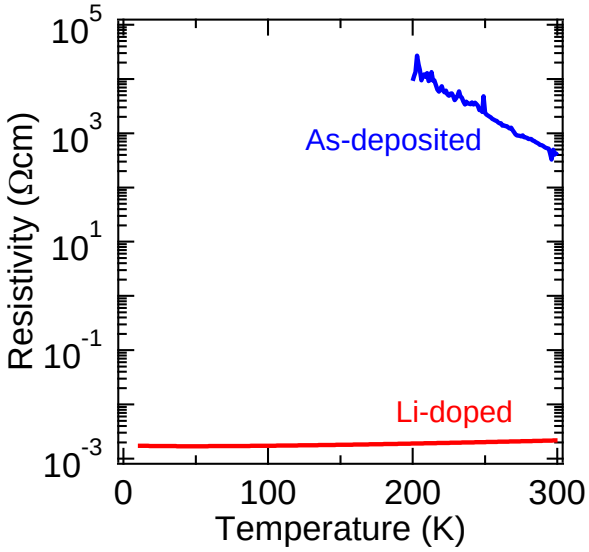

Figure 5.10 Resistivity of Li doped anatase TaON film (a red line) and as-grown film (a blue line) plotted as functions of temperature. The resistivity of the as-grown film was measured by a two-probe method due to the high resistance.

I also conducted the Li insertion to anatase TaON film fabricated at 800°C with lower resistivity than that fabricated at 750°C through the reaction with 1.6×10^{-2} M *n*-butyllithium solution. The Li amount of this film was about $(3\pm1)\times10^{19}$ cm^{-3}, which is almost the same as that of Li inserted anatase TaON fabricated at 750°C. This means that the amount of anion vacancy in anatase TaON thin films did not affect the efficiency of Li insertion. On the other hand, the resistivity of the film was smaller (ρ ~6.7×10^{-4} Ωcm), which is enough low for transparent electrode applications (Fig. 5.9). This low resistivity is mainly due to higher Hall mobility (μ_H ~34 $cm^2V^{-1}s^{-1}$) than Li inserted anatase TaON fabricated at 750°C (μ_H ~20 $cm^2V^{-1}s^{-1}$) (Fig. 5.9), probably because grain boundary scattering was suppressed in anatase TaON thin films fabricated at 800°C by forming larger grain than that at 750°C (Fig. 3.2).

5.4 Summary

I succeeded in synthesizing W-doped anatase TaON thin film by NPA-PLD. However, the carrier density of anatase TaON did not change by W substitution (n_e~4.0×10^{19} cm^{-3}), suggesting that W did not act as an electron donor in anatase TaON. It might be caused by charge compensation due to substitution of N^{3-} for O^{2-} occurring during the film growth.

On the other hand, carriers of the order of 10^{20} cm^{-3} were doped into TaON by Li insertion, which was carried out by soft chemical reaction with *n*-butyllithium solution. This demonstrates that carrier doping process after the film growth (i.e. after O/N ratio is fixed) is effective to avoid the charge compensation because anion substitution does not occur during doping process. Concentration of *n*-butyllithium solution affected on both Li amount and carrier density in anatase TaON, suggesting that inserted Li generated conduction electrons. In the region of high concentration of *n*-butyllithium solution, larger carrier density than that

of anion-deficient anatase TaON was achieved. The Li-doped anatase TaON films also showed higher Hall mobility than anion-deficient anatase TaON, indicating that Li was an effective dopant for carrier doping into anatase TaON. As a result of these larger carrier density and Hall mobility, resistivity was decreased to ρ ~6.7×10^{-4} Ωcm, which is enough low for transparent electrode applications.

These results also indicate that soft chemical Li insertion is a powerful tool for carrier doping into materials to which conventional substitutional technique such as cation substitution is not applicable.

Capter 6
Stabilization of anatase TaON by using anatase TiO_2 seed layer

6.1 Introduction

I synthesized phase-pure anatase TaON in thin-film form with the assistance of epitaxial stabilization on a lattice-matched $(LaAlO_3)_{0.3}$-$(SrAl_{0.5}Ta_{0.5}O_3)_{0.7}$ (LSAT) (001) single crystalline substrate as described in Chapter 3. The visible light absorption (E_g~2.37 eV), high refractive index (n>3.0), and high Hall mobility (μ_H~17 $cm^2V^{-1}s^{-1}$) of anatase TaON films are promising for application to photoelectrode and electronic devices.

From a practical viewpoint, the high growth temperature of anatase TaON (≥750 °C) is undesirable. In case of the growth temperature, it is well known that the temperature required for heteroepitaxy can be decreased by using a substrate with a better lattice match to that of the thin film [99]. In my study in Chapter.3, the only substrate used was LSAT, on the basis of the prediction of the lattice parameters of anatase TaON by first-principles calculations. Therefore, there may be a substrate with a better lattice match to anatase TaON. Another possible way of enhancing epitaxial growth is to introduce a seed layer that has not only the same lattice parameters, but also the same atomic arrangements as those of anatase TaON [3]. I adopted thin anatase TiO_2 epitaxial film, which has the same network of edge-shared MX_6 octahedra as anatase TaON as the seed layer.

In addition, expensive single crystal substrates for stabilizing metastable anatase phase cannot be used in practical applications. Therefore, not only decrease of the growth

temperature but also the growth on inexpensive substrate such glass substrate are necessary. Considering the previous reports of enhanced film growth using a seed layer [3], it seems possible to synthesize anatase TaON thin films even on glass substrates by using a polycrystalline anatase TiO_2 seed layer, which can be grown on glass substrate [100].

In this chapter, I carried out two synthesis, growth at lower temperature and growth on glass substrate by nitrogen-plasma-assisted pulse laser deposition (NPA-PLD). I systematically investigated the effects of lattice matching on the epitaxial growth of anatase TaON thin films. In addition, I succeeded in synthesizing anatase TaON thin film on glass substrate with polycrystalline anatase TiO_2 seed layer.

---

*This chapter contains the contents of the following publications.

"Low temperature epitaxial growth of anatase TaON using anatase TiO_2 seed layer"
A. Suzuki, Y. Hirose, D. Oka, S. Nakao, T. Fukumura, and T. Hasegawa, Jpn. J. Appl. Phys. **54**, 080303 (2015)

6.2 Experimental procedure

Anatase TaON thin films were grown on the following five substrates with different in-plane lattice parameters *a*: (001)-plane K_2NiF_4-type $LaSrAlO_4$ (LSAO) (tetragonal, *a*=3.745 Å), perovskite LSAT (cubic, *a*/2=3.868 Å), 0.5 wt% Nb-doped $SrTiO_3$ (NSTO) (cubic, *a*=3.905 Å), $KTaO_3$ (KTO) (cubic, *a*=3.989 Å), and spinel $MgAl_2O_4$ (MAO) (cubic, *a*/2=4.042 Å). The films were fabricated by NPA-PLD, which has been described in Chapter.3. A ceramic Ta_2O_5 pellet was ablated by focused UV pulses from a KrF excimer laser (λ=248 nm). The fluence and repetition rate of the excimer laser were adjusted to set the deposition rate to ~17 nm/h; typical parameters were 1.6 J cm^{-2} $shot^{-1}$ and 4 Hz, respectively. Substrate temperature (T_S) was varied from 550 to 750 °C by using an infrared lamp. The depositions were conducted under N_2 gas (1×10^{-5} Torr) activated by a radio-frequency (RF) wave plasma source with an output power of 250 or 300 W.

When anatase TaON thin films were grown on glass substrates with the polycrystalline anatase TiO_2 seed layer, the synthesis procedure shown in Fig. 6.1 was adopted. First, an amorphous anatase TiO_2 thin film was deposited on fused silica substrate at room temperature by PLD. A TiO_2 single crystalline substrate was used as an oxide target and was ablated by focused UV pulses from a KrF excimer laser (λ=248 nm). The fluence and repetition rate of the excimer laser were adjusted to set the deposition rate to ~60 nm/h; typical parameters were 1.3 J cm^{-2} $shot^{-1}$ and 2 Hz, respectively. The deposition was conducted under O_2 gas (1×10^{-3} Torr). Typical film thickness of the TiO_2 film was 10 nm, evaluated using a stylus profiler. Next, substrate temperature (T_S) was raised to 700 °C using an infrared lamp to form polycrystalline anatase TiO_2 via solid phase crystallization. Finally, a TaON film was fabricated by NPA-PLD with the same condition as the epitaxial thin film of anatase TaON described above. T_S was kept at 700 °C. The deposition was conducted under N_2 gas (1×10^{-5} Torr) activated by a radio-frequency (RF) wave plasma source with an

output power of 300 W.

The crystal structures and crystallinities of the films were examined by X-ray diffraction (XRD) analysis using Cu-Kα radiation and a four-axis diffractometer. Crystal structure and orientation of the films grown on glass substrates were analyzed by simulation software. Typical film thicknesses were 40−55 nm, evaluated using a stylus profiler. The oxygen and nitrogen contents of the TaON thin films were evaluated using an energy dispersive X-ray spectroscope equipped with a scanning electron microscope (SEM-EDX). The samples had an almost stoichiometric chemical composition within the experimental error of ~10% unless otherwise noted. Absorption coefficient of the anatase TaON films grown on glass substrates was determined by ultraviolet-visible spectroscopy (UV-Vis spectroscopy) in a spectral range of 1.5-4 eV.

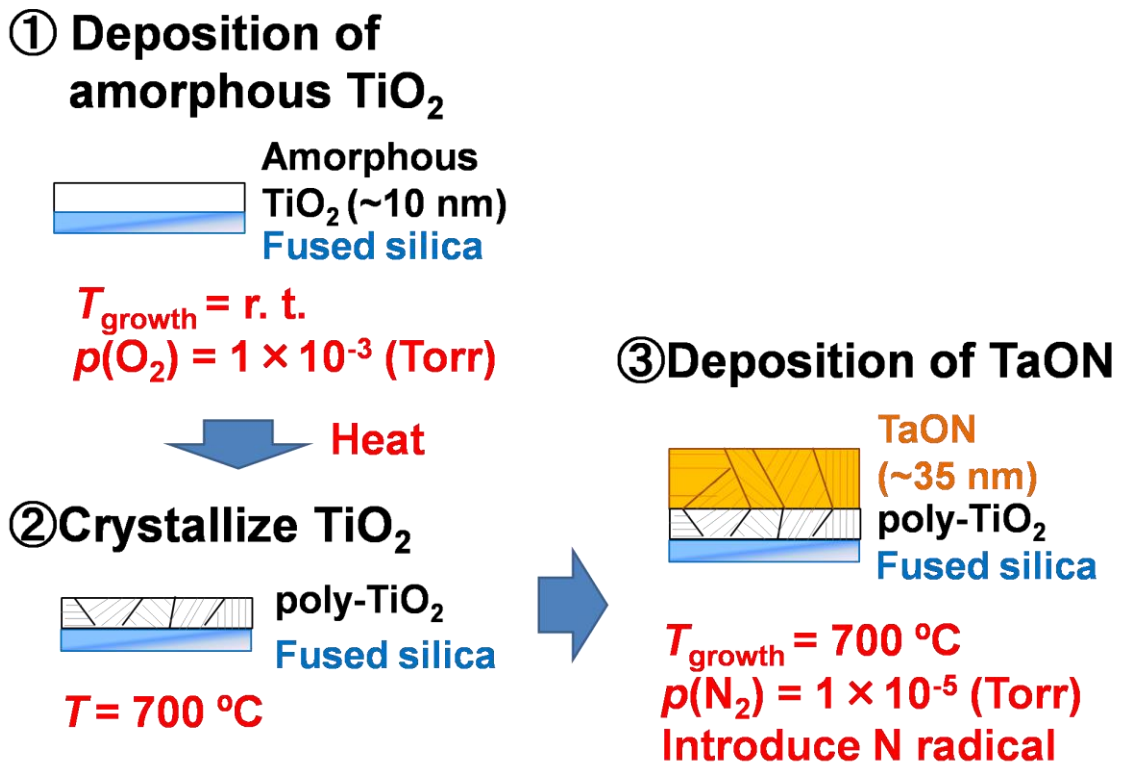

Figure 6.1 Schematic diagram of processes for growth of anatase TaON on fused silica substrates with polycrystalline anatase TiO_2 seed layer.

6.3 Results and discussion

6.3.1 Low temperature epitaxial growth of anatase TaON

Figure 6.2(a) shows θ-2θ XRD patterns of the TaON films grown on various single-crystal substrates at 750 °C. The epitaxial growth of anatase TaON was apparently affected by the substrate lattice parameter: A strong 004 diffraction peak of anatase TaON was observed at ~35° with no impurity peak on NSTO, KTO, and MAO substrates as well as on the LSAT substrate. In contrast, TaON film grown on LSAO exhibited a very weak anatase 004 peak with impurity peaks. This degradation in crystallinity probably originated from the very large lattice mismatch between the (001)-plane of LSAO and that of anatase TaON. On the basis of the lattice parameters of bulk anatase TaON [72], which corresponds well to the value predicted by first-principles calculation [70], a_{bulk}=3.92 Å, the lattice mismatch between anatase TaON and LSAO is −4.5%, which is much larger than the mismatches for LSAT, NSTO, KTO, and MAO substrates (−1.33, −0.38, +1.75, and +3.10%, respectively). I note that anatase TaON thin film on KTO had a slightly nitrogen-rich chemical composition (N/Ta ~1.1). This off-stoichiometry was considered to not affect the epitaxial growth of the film, because the lattice parameters of the film were almost the same as those of the fully relaxed TaON film grown on the MAO substrate. TaON thin films were also deposited at a lower temperature of 700 °C on LSAT, NSTO, KTO, and MAO substrates. Notably, these films show much less intense anatase TaON 004 diffraction than those fabricated at 750 °C, as shown in Fig. 6.2(b). However, there is no significant difference in the peak area of 004 diffraction (Fig. 6.3). From these results, I considered that these substrates are not effective in reducing the growth temperature of anatase TaON; the reduction of growth temperature is less than 50 ºC, as seen from Fig. 6.3.

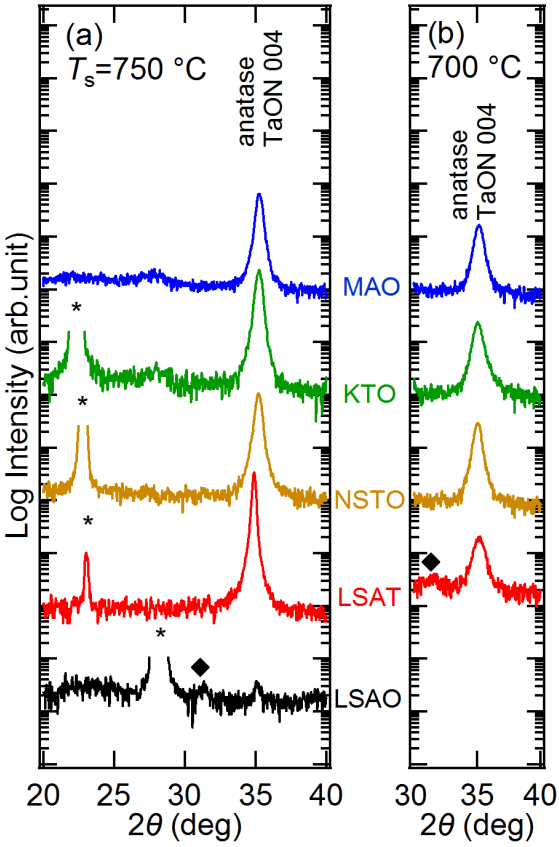

Figure 6.2 θ-2θ XRD patterns of TaON films grown on various substrates at (a) T_S=750 °C and (b) T_S=700 °C. Asterisks and filled diamonds represent diffractions from substrates and impurity phases, respectively.

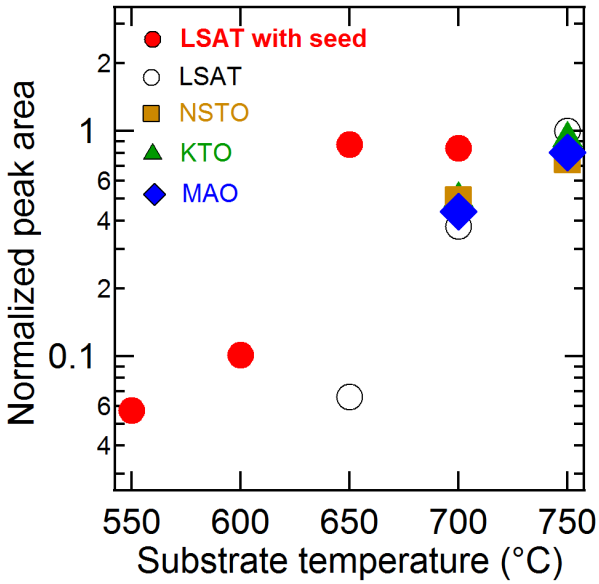

Figure 6.3 Peak area of 004 diffraction of anatase TaON on various substrates and anatase TiO_2 seed layer plotted as functions of T_S. The peak area was normalized by film thickness and scaled by that of the film grown at 750 °C on LSAT.

To discuss the effect of lattice mismatch on the epitaxial growth of anatase TaON, the lattice parameters and crystallinity of the anatase TaON grown at 750 °C were investigated (Fig. 6.4). The in-plane lattice parameters (*a*-axis length) of the TaON films on LSAT and NSTO substrates agreed well with those of the substrates themselves. In contrast, the *a*-axis lengths of the TaON films on the KTO and MAO substrates were smaller than the lattice parameters of the substrates and almost the same as a_{bulk}. This relaxation of epitaxial

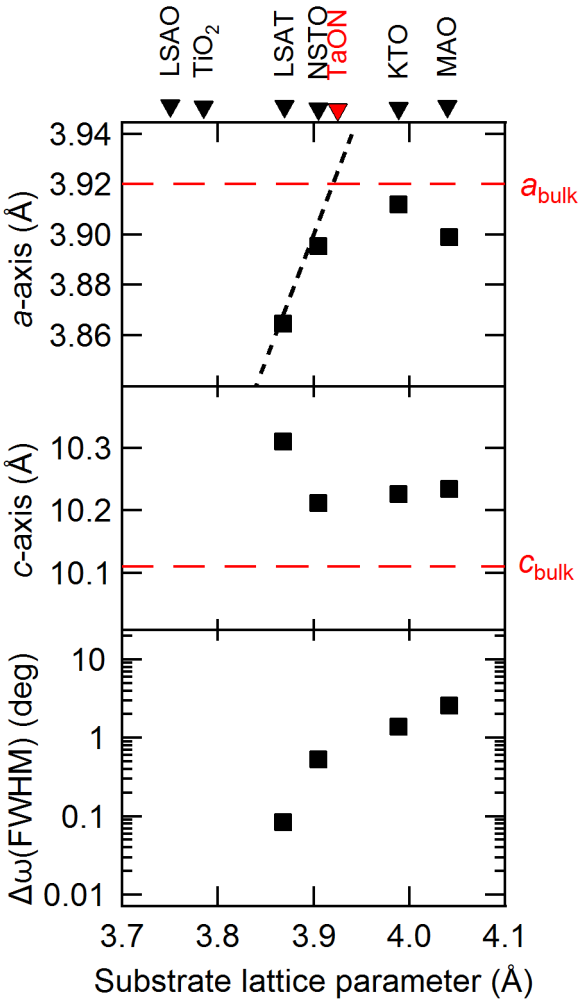

Figure 6.4 In-plane (top panel) and out-of-plane (middle panel) lattice parameters of the anatase TaON films grown on various substrates. The black dashed line represents the lattice parameter fully locked to the substrate. FWHMs of the rocking curves of 004 diffraction are also plotted in the bottom panel.

strain for the anatase TaON thin films on KTO and MAO substrates was caused by the large lattice mismatch. Indeed, the FWHMs of the rocking curves of these relaxed films were much larger than those of the films grown on LSAT and NSTO substrates, reflecting the defects introduced by lattice relaxation. Note that the anatase TaON film grown on NSTO exhibited a broader rocking curve than the film on LSAT despite the smaller lattice mismatch. I speculate that oxygen diffusion from the NSTO substrate [101] deteriorated the crystallinity of the film. These results are indicative of the difficulty in reducing the growth temperature of anatase TaON merely by adjusting lattice matching.

Thus, to decrease the growth temperature, I attempted to stabilize anatase TaON by introducing an epitaxial thin film of anatase TiO_2 (a=3.78Å) as a seed layer. The anatase structure consists of a network of edge-shared MX_6 octahedra, while the perovskite structure is composed of corner-shared MX_6 octahedra. The introduction of an anatase TiO_2 seed layer would reduce the instability originating from the difference between these octahedral networks. Before the deposition of TaON, a ~5-nm-thick (001)-oriented anatase TiO_2 seed layer was epitaxially grown on (001)-plane LSAT single-crystal substrates by conventional PLD. The anatase TiO_2 seed layers were grown at T_S = 600 °C under a partial O_2 gas pressure of 1×10^{-4} Torr. A single-crystal plate of rutile TiO_2 was used as the target. The excimer laser fluence and repetition rate were adjusted to 1.4 J cm^{-2} $shot^{-1}$ and 2 Hz, respectively. Partial relaxation of the in-plane lattice constant of the seed layer (a ~3.81 Å) from the LSAT substrate (a/2=3.868 Å) was observed by reflection high-energy electron diffraction. The growth conditions of the TaON films were the same as those described in the previous sections unless otherwise noted. Figure 6.5 shows the θ-2θ XRD patterns of the TaON films grown on LSAT substrates at low temperature with and without an anatase TiO_2 seed layer. The intensity of the 004 diffraction of anatase TaON was apparently enhanced by the presence of the anatase TiO_2 seed layer, and phase-pure anatase TaON was obtained even at

T_s=650 °C. I note that anatase TaON thin films grown at the lower temperature showed a slightly nitrogen-rich composition. Thus, I compared films with almost the same chemical composition (N/Ta ~1.1) in Fig. 6.5. Then, I again plotted the peak area of the 004 diffraction against T_S (Fig. 6.3). By introducing the seed layer, the peak area was clearly increased at T_s=650 and 700 °C, and became comparable to that at T_s=750 °C without the seed layer. The reduction of the growth temperature is roughly estimated to be 50–100 °C, which is much larger than those attained by changing the substrate. Considering the fact that the partially relaxed anatase TiO_2 seed layer had a larger lattice mismatch with anatase TaON (−2.8%) than that of the LSAT substrate (−1.33%), the seed layer and film having the same MX_6 octahedral network were the main contributors to the reduction in the growth temperature.

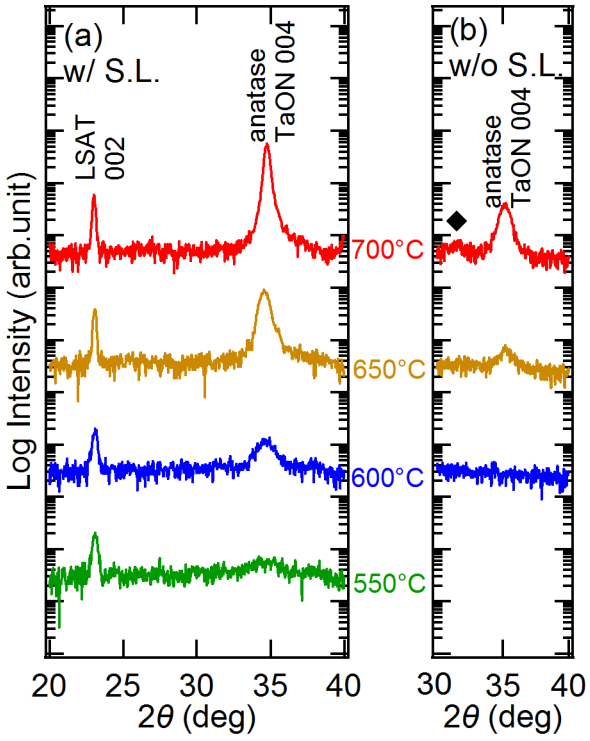

Figure 6.5 θ-2θ XRD patterns of TaON films grown on LSAT substrate (a) with and (b) without anatase TiO_2 seed layer (T_S= 600, 650, and 700 °C). The filled diamond represents diffraction from an impurity phase.

I also grew anatase TaON on NSTO and LSAO substrates seeded with anatase TiO_2, where NSTO was lattice matched to anatase TaON and LSAO to anatase TiO_2. In particular, lattice matching between the substrate and the seed layer has often been argued to be effective for the reduction of the film growth temperature [102]. However, θ-2θ XRD patterns of the TaON films with an anatase TiO_2 seed layer indicated almost the same intensity of the 004 diffraction on NSTO, LASO, and LSAT substrates (Fig. 6.6). This indicates that the growth temperature of anatase TaON is not sensitive to the lattice constants of the substrates even with the seed layer, which supports the fact that the MX_6 octahedral network of the seed layer was the main contributor to the reduction in the growth temperature.

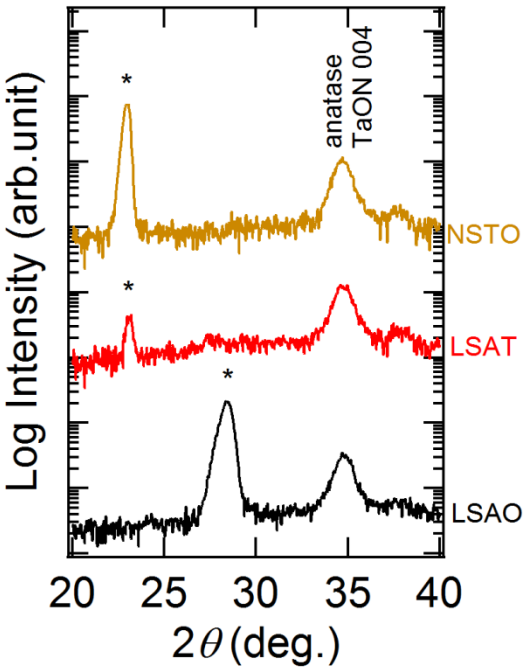

Figure 6.6 θ-2θ XRD patterns of TaON films grown at T_S=650 °C on NSTO, LSAT, and LSAO substrates with anatase TiO_2 seed layer. Asterisks represent substrate diffractions.

6.3.2 Growth of anatase TaON thin film on glass substrate

θ-2θ XRD patterns of the TaON films are shown in Fig. 6.7. The TaON thin film directly grown on fused silica substrate showed diffraction peaks of baddeleyite phase, which is the most thermodynamically stable phase of TaON. In contrast, by introducing the seed layer, peaks originated from baddeleyite phase disappeared and new peaks appeared at 2θ ~ 24.0º, 35.0º and 36.8º. The diffraction pattern of this film obtained by an area detector consists of arches with finite broadening along χ direction, representing preferred orientation of the film (Fig. 6.8). To determine the crystal structure and orientation of the film, analysis

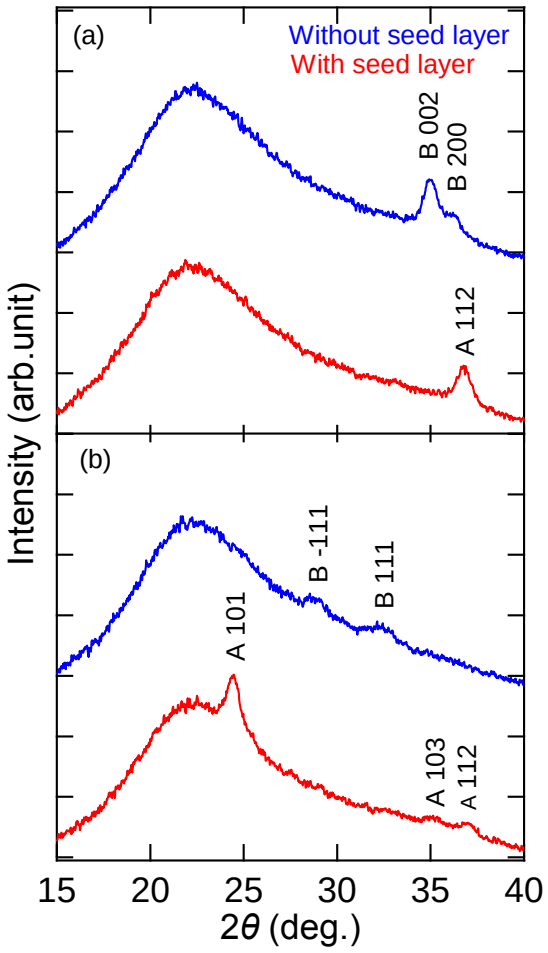

Figure 6.7 θ-2θ XRD patterns in (a) χ = 67.5-113.5° and (b) χ = 0-45° of the TaON films grown on fused silica substrate with and without anatase TiO_2 seed layer. Labels “A” and “B” represent anatase and baddeleyite, respectively.

using simulation software was carried out. As a result, I concluded that the obtained film was (112)-oriented anatase TaON of which [112] axis was tilted by ~6º from the surface normal (Fig. 6.9a) because simulated results with this crystal structure and orientation reproduced the XRD result very well, as shown in Fig. 6.9b. Thus, I successfully fabricated anatase TaON on glass substrate with anatase TiO_2 seed layer.

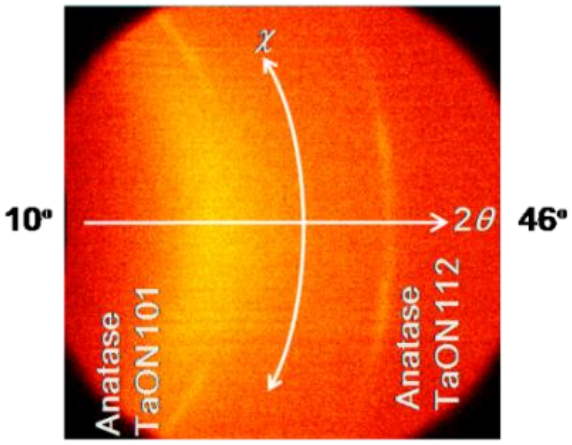

Figure 6.8 Area detector image of XRD pattern of the TaON film grown on fused silica substrate with anatase TiO_2 seed layer. The center of the detector was set at 2θ=28º and χ=90º.

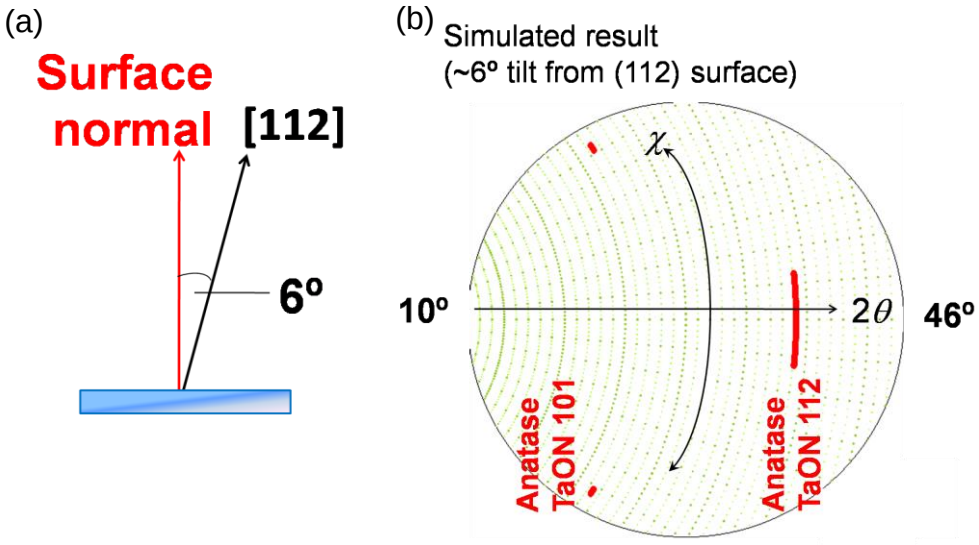

Figure 6.9 (a) Schematic diagram of the orientation of (112) surface tilted by ~6º. (b) Simulated area detector image of XRD pattern of the TaON film with (112) orientation tilted by ~6º.

It should be noted that the anatase TiO_2 seed layer was polycrystalline, as confirmed by the two-dimensional XRD image (Fig. 6.10) revealing a perfect ring with infinite broadening along χ direction. On the other hand, the anatase TaON thin film on the seed layer indicated (112)-preferred orientation. This may be related to the fact that the (112) surface is considerably stable in anatase structure. Actually, (112)-preferred oriented anatase TiO_2 thin films were synthesized on glass substrate [103].

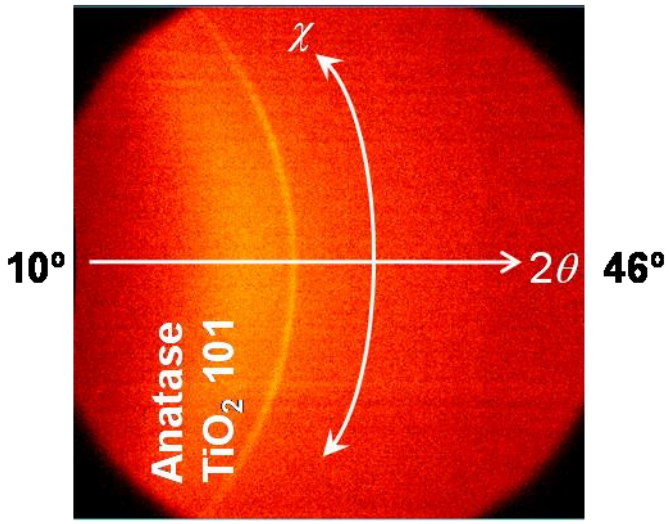

Figure 6.10 Area detector image of XRD pattern of the TiO_2 film grown on fused silica substrate. The center of the detector was set at 2θ=28º and χ=90º.

Lattice constants calculated from the diffractions were a=0.391 nm and c=1.007 nm, which well correspond to the values of bulk polycrystalline anatase TaON (a= 0.392 nm and c=1.011 nm) [72]. The chemical composition of the anatase TaON thin film was evaluated as $TaO_{1.07\pm0.1}N_{0.95\pm0.09}$ by using SEM-EDX, which is almost stoichiometric within the experimental error of ~10%. Lower sheet resistance of the obtained thin films (R ~ 25 kΩ/sq.) than non–doped anatase TiO_2 and TaON (R > 100 kΩ/sq.) suggests the mixing of Ti and Ta at the interface, because anatase TiO_2 doped with Ta indicates low resistance down to

10^{-4} Ωcm order [39].

Finally, the band gap of anatase TaON thin films is briefly mentioned. Figure 6.11 shows the absorption coefficient of the anatase TaON film grown on fused silica substrate determined by UV-Vis spectroscopy. It showed an abrupt increase around 2.2 eV. As same as anatase TaON epitaxial thin film, E_g was determined to be 2.22 eV from $(\alpha h\nu)^{1/2}$ vs hν plot (inset of Fig. 6.11). This E_g value is comparable to that of anatase TaON epitaxial thin film described in Chapter 3 (2.37 eV). The slight differences in the E_g values might be due to the difference in lattice parameters [104].

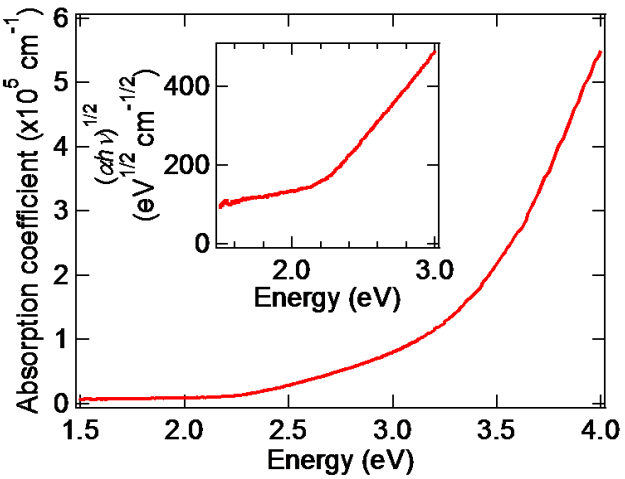

Figure 6.11 Absorption coefficient α of the anatase TaON thin film. (Inset) Optical band gap of the anatase TaON thin film determined under an assumption that anatase TaON is an indirect transition semiconductor.

6.4 Summary

Phase-pure anatase TaON thin films were epitaxially grown on (001)-plane NSTO, KTO, and MAO single-crystalline substrates as well as on LSAT. However, the growth temperatures of anatase TaON on these substrates were almost the same as that on LSAT, which indicates that the reduction of growth temperature by improving the mismatch of

lattice parameters is difficult. On the other hand, the growth temperature was reduced by 50–100 ºC by introducing a seed layer of a thin anatase TiO_2 epitaxial film, which has the same network of edge-shared MX_6 octahedra as anatase TaON. These matching edge-shared networks enhanced the epitaxial growth of the anatase TaON thin films. The enhanced epitaxial stabilization of anatase TaON on the anatase TiO_2 seed layer is expected to enable us to develop a synthetic route for anatase TaON that does not require single-crystal substrates or additives. For example, epitaxial growth on a polycrystalline anatase TiO_2 template on a glass substrate or ammonolysis of anatase TiO_2-Ta_2O_5 core-shell particles may become possible.

I also demonstrated the synthesis of anatase TaON thin films even on glass substrate by introducing a polycrystalline anatase TiO_2 seed layer. This anatase TaON thin film indicated (112) preferred orientation, even though the anatase TiO_2 seed layer was polycrystalline. This might be related to the stability of the anatase (112) surface.

Chapter 7
General conclusion

In this thesis, I studied synthesis, characterization, and functionalization of an oxynitride semiconductor, anatase TaON in thin film form.

High-Mobility Electron Conduction in Oxynitride: Anatase TaON

By using epitaxial force from lattice matched substrates, metastable anatase TaON epitaxial thin films were successfully fabricated with nitrogen-plasma-assisted pulsed laser deposition (NPA-PLD) without any impurity doping. The obtained anatase TaON films showed band gap (E_g) of 2.37 eV and refractive index (n) of ~3.0 in visible light region. Transport measurements revealed that the anatase TaON films fabricated at 800°C can be categorized as a degenerated semiconductor with Hall mobility (μ_H) of ~17 $cm^2V^{-1}s^{-1}$, which is comparable to that of anatase TiO_2 used as photoelectrodes and transparent electrodes in various electric devices.

Tuning of optical properties in solid-solution of anatase $(TiO_2)_x(TaON)_{1-x}$

Tunable optical properties of anatase TaON, refractive index n and band gap E_g, was achieved by making solid-solution with anatase TiO_2: $(TiO_2)_x(TaON)_{1-x}$, which were fabricated by controlling the nitrogen amounts in $(TiO_2)_x(TaON)_{1-x}$ thin films with oxygen partial pressure. E_g systematically changed from visible light region (~2.4 eV) to ultraviolet region (> 3.2 eV) in accordance with ratio of TaON and TiO_2, x. Moreover, n in visible light region was also controllable from 3.2 (TaON side) to 2.7 (TiO_2 side). These imply that

$(TiO_2)_x(TaON)_{1-x}$ could be optimized for wide applications from visible light active photoelectrode and transparent electrode by adjusting *x*.

Carrier doping to anatase TaON

Transport properties of anatase TaON were controlled by the carrier doping with Li insertion, which was conducted by soft-chemical Li insertion with *n*-butyllithium solution. Li insertion was confirmed by the lattice expansion and composition analysis. The concentration of *n*-butyllithium solution largely affected on both Li amount and carrier density in anatase TaON, suggesting that inserted Li generated conduction electrons. The lowest resistivity of Li-doped anatase TaON was ~6.7×10^{-4} Ωcm, which was enough low for transparent electrode applications. Considering the failure of carrier doping by W substitution, it can be said that soft chemical Li insertion is a powerful tool for carrier doping into materials in which conventional cation substitution technique cannot be used due to charge compensation.

Stabilization of anatase TaON by using anatase TiO_2 seed layer

Considering practical applications, low-cost and large-area fabrication is favorable. Thus, I established the process to synthesize anatase TaON at lower growth temperature and without expensive single crystalline substrates by using anatase TiO_2 seed layer, which stabilized anatase TaON with the same crystal structure as anatase TiO_2.

By the synthesis and characterization of anatase TaON, I demonstrated the possibility of anatase TaON as an electronic material applicable to photoelectrode and transparent electrode. Towards these applications, the optical and transport properties of anatase TaON were precisely controlled by fabricating solid-solution with anatase TiO_2 and carrier doping associated with Li insertion, respectively, which considerably widened the

range of application of anatase TaON. As another approach towards practical uses, low-cost and large-area fabrication of anatase TaON was conducted by introducing anatase TiO_2 seed layer. From these results, I concluded that anatase TaON is a promising electronic material, which has the potential in solving problems in existing oxides such as no visible light absorption in photoelectrode and low refractive index in transparent electrode.

Bibliography

[1] S. A. Chambers, Surf. Sci. Rep., **39**, 105 (2000).

[2] 中嶋一雄 責任編集, エピタキシャル成長のメカニズム, 2002 年, 共立出版株式会社.

[3] Y. Suzuki, R. B. van Dover, E. M. Gyorgy, J. M. Phillips, V. Korenivski, D. J. Werder, C. H. Chen, R. J. Cava, J. J. Krajewski, W. F. Peck, and K. B. Do, Appl. Phys. Lett., **68**, 714 (1996).

[4] A. Tsukazaki, H. Saito, K. Tamura, M. Ohtani, H. Koinuma, M. Sumiya, S. Fuke, T. Fukumura, and M. Kawasaki, Appl. Phys. Lett., **81**, 235 (2002).

[5] M. Gonschorek, J.-F. Carlin, E. Feltin, M. A. Py, and N. Grandjean, Appl. Phys. Lett., **89**, 062106 (2006).

[6] T. Minami, Semicond. Sci. Technol., **20**, S35 (2005).

[7] H. Hosono, Thin Solid Films, **515**, 6000 (2007).

[8] H. Liu, V. Avrutin, N. Izyumskaya, Ü. Özgür, H. Morkoç, Superlattices Microstruct., **48**, 458 (2010).

[9] F.O. Durodija, H. Izumi, T. Ishihara, and H. Yoshioka, Jpn. J. Appl. Phys., **39**, L277 (2000).

[10] H. Agura , A. Suzuki, T. Matsushita, T. Aoki, and M. Okuda, Thin Solid Films, **445**, 263 (2003).

[11] J.W. Bae, S.W. Lee, and G.Y. Yeom, Electrochem. Soc., **154**, D34 (2007).

[12] Y. Furubayashi, T. Hitosugi, Y. Yamamoto, K. Inaba, G. Kinoda, Y. Hirose, T. Shimada, and T. Hasegawa, Appl. Phys. Lett., **86**, 252101 (2005).

[13] J. Kasai, T. Hitosugi, M. Moriyama, K. Goshonoo, N. L. H. Hoang, S. Nakao, N. Yamada, and T. Hasegawa, J. Appl. Phys., **107**, 053110 (2010).

[14] H. Kim, C. M. Gilmore, A. Piqué, J. S. Horwitz, H. Mattoussi, H. Murata, Z. H. Kafafi, and D. B. Chrisey J. Appl. Phys., **86**, 6451 (1999).

[15] X. W. Sun and H. S. Kwok, J. Appl. Phys., **86**, 408 (1999).

[16] S. Mohri, Y. Hirose, S. Nakao, N. Yamada, T. Shimada, and T. Hasegawa, J. Appl. Phys., **111**, 093528 (2012).

[17] A. Kudo and Y. Miseki, Chem. Soc. Rev., **38**, 253 (2009).

[18] T. Luttrell1, S. Halpegamage1, J. Tao1, A. Kramer1, E. Sutter, and M. Batzill, Sci. Rep., **4**, 4043 (2014).

[19] K. Lv, J. Yu, L. Cui, S. Chen, and M. Li, J. Alloys Compd., **509**, 4557 (2011).

[20] R. Abe, K. Sayama, K. Domen, and H. Arakawa, Chem. Phys. Lett., **344**, 339 (2001).

[21] H. Tang, K. Prasad, R. Sanjinès, P. E. Schmid, and F. Lévy, J. Appl. Phys., **75**, 2042 (1994).

[22] G.S. Herman and Y. Gao, Thin Solid Films, **397**, 157 (2001).

[23] L. Forro, O. Chauvet, D. Emin, L. Zuppiroli, H. Berger, and F. Lévy, J. Appl. Phys., **75**, 633 (1994).

[24] Z. Ding, G. Q. Lu, and P. F. Greenfield, J. Phys. Chem. B., **104**, 4815 (2000).

[25] A. V. Emeline, Y. Furubayashi, X. Zhang, M. Jin, T. Murakami, and A. Fujishima, J. Phys. Chem. B, **109**, 24441 (2005).

[26] R. Asahi, T. Morikawa, T. Ohwaki, K. Aoki, and Y. Taga, Science, **293**, 269 (2001).

[27] L. Lin, W. Lin, Y. X. Zhu, B. Y. Zhao, and Y. C. Xie, Chem. Lett., **34**, 284 (2005).

[28] T. Umebayashi, T. Yamaki, S. Tanaka, and K. Asai, Chem. Lett., **32**, 330 (2003).

[29] C. Zhang , Y. Jia, Y. Jing, Y. Yao, J. Ma, and J. Sun, Comput. Mater. Sci., **79**, 69 (2013).

[30] T. Okato, T. Sakano, and M. Obara, Phys. Rev. B, **72**, 115124, (2005).

[31] H. Irie, Y. Watanabe, and K. Hashimoto, J. Phys. Chem. B, **107**, 5483 (2003).

[32] J. Wu, J. Appl. Phys., **106**, 011101 (2009).

[33] A. Ohtomo, M. Kawasaki, T. Koida, K. Masubuchi, and H. Koinuma, Appl. Phys. Lett., **72**, 2466 (1998).

[34] K.Y. Rajpure, M.N. Kusumade, Michael N. Neumann-Spallart, C.H. Bhosale, Mater. Chem. Phys., **64**, 184, (2000).

[35] S. woo Lee, Y.-W. Kim, and H. Chen, Appl. Phys. Lett., **78**, 350 (2001).

[36] H. J. Ko, Y. F. Chen, S. K. Hong, H. Wenisch, T. Yao, and D. C. Look, Appl. Phys. Lett., **77**, 3761 (2000).

[37] A.L. Dawar and J. C. Joshi, J. Mater. Sci., **19**, 1 (1984).

[38] K. L. Chopra, S. Major, and D. K. Pandya, Thin Solid Films, **102**, 1 (1983).

[39] T. Hitosugi, Y. Furubayashi, A. Ueda, K. Itabashi, K. Inaba, Y. Hirose, G. Kinoda, Y. Yamamoto, T. Shimada, and T. Hasegawa, Jpn. J. Appl. Phys., **44**, L1063, (2005).

[40] U. Takeuchi, A. Chikamatsu, T. Hitosugi, H. Kumigashira, M. Oshima, Y. Hirose, T. Shimada, and T. Hasegawa, J. Appl. Phys., **107**, 023705 (2010).

[41] S. G. Ebbinghaus, H.-P. Abicht, R. Dronskowski, T. Muller, A. Rüller, A. Weidenkaff, Prog. Solid State Chem., **37**, 173 (2009).

[42] A. Fuertes, Dalton Trans., **39**, 5942 (2010).

[43] M. Yashima, K. Maeda, K. Teramura, T. Takata, and K. Domen, Chem. Phys. Lett., **416**, 225 (2005).

[44] X. Sun, K. Maeda, M. L. Faucheur, K. Teramura, and K. Domen, Appl. Catal. A, **327**, 114 (2007).

[45] Y.-C. Lee, T.-Y. Lin, C.-W. Wu, H. Teng, C.-C. Hu, S.-Y. Hu, and M.-D. Yang, J. Appl. Phys., **109**, 073506 (2011).

[46] R. Aguiar, A. Weidenkaff, C. Schneider, A. Reller, and S. Ebbinghaus, Prog. Solid State Chem., **35**, 291 (2007).

[47] I. C. Lekshmi, A. Gayen, and M. S. Hegde, Mater. Res. Bull., **40**, 93 (2005).

[48] D. Oka, Y. Hirose, T. Fukumura, and T. Hasegawa, Cryst. Growth Des., **14**, 87 (2014).

[49] I. Marozau, A. Shkabko, G. Dinescu, M. Döbeli, T. Lippert, D. Logvinovich, M. Mallepell, A. Weidenkaff, and A. Wokaun, Appl. Phys. A, **93**, 721 (2008).

[50] R. Aguiar, D. Logvinovich, A. Weidenkaff, A. Rachel, A. Reller, S. G. Ebbinghaus, Dyes and Pigments, **76**, 70 (2008).

[51] A. Fuertes, Mater. Horiz., **2**, 453 (2015).

[52] K. Ueda, H. Kato, M. Kobayashi, M. Hara, and M. Kakihana, J. Mater. Chem. A, **1**, 3667 (2013).

[53] S. S. Pan, Y. X. Zhang, X. M. Teng, G. H. Li, and L. Li, J. Appl. Phys., **103**, 093103 (2008).

[54] Y. Ye, R. Lim, and J. M. White, J. Appl. Phys., **106**, 074512 (2009).

[55] H.-S. Kim, S.H. Jeon, J. S. Park, T. S. Kim, K. S. Son, J.-B. Seon, S.-J. Seo, S.-J. Kim, E. Lee, J. G. Chung, H. Lee, S. Han, M. Ryu, S. Y. Lee, and K. Kim, Sci. Rep., **3**, 1459 (2013).

[56] Y.-I. Kim, P. M. Woodward, K. Z. Baba-Kishi, and C. W. Tai, Chem. Mater., **16**, 1267 (2004).

[57] D. Oka, Y. Hirose, H. Kamisaka, T. Fukumura, K. Sasa, S. Ishii, H. Matsuzaki, Y. Sato, Y. Ikuhara, and T. Hasegawa, Sci. Rep., **4**, 4987 (2014).

[58] M. Yang, J. Oró-Solé, A. Kusmartseva, A. Fuertes, and J. P. Attfield, J. Am. Chem. Soc., **132**, 4822 (2010).

[59] G. Brauer and J. R. Weidlein, Angew. Chem., Int. Edit., **4**, 875 (1965).

[60] J. Tao, J.W. Chai, L.M. Wong, Z. Zhang, J.S. Pan, and S.J. Wang, J. Solid State Chem., **204**, 27 (2013).

[61] M. Yashima, Y. Lee, and K. Domen, Chem. Mater., **19**, 588 (2007).

[62] W.-J. Chun, A. Ishikawa, H. Fujisawa, T. Takata, J. N. Kondo, M. Hara, M. Kawai, Y. Matsumoto, and K. Domen, J. Phys. Chem. B, **107**, 1798 (2003).

[63] K. Kato, H. Toyota, Y. Jin, and T. Ono, Vacuum, **83**, 592 (2009).

[64] G. Hitoki, T. Takata, J. N. Kondo, M. Hara, H. Kobayashi, and K. Domen, Chem. Commun., 1698 (2002).

[65] R. Abe, T. Takata, H. Sugihara, and K. Domen, Chem. Lett., **34**, 1162 (2005).

[66] H. Schilling, M. Lerch, A. Börger, K.-D. Becker, H. Wolff, R. Dronskowski, T. Bredow, M. Tovar, and C. Baehtz, J. Solid State Chem., **179**, 2416 (2006).

[67] A. Stork, H. Schilling, C. Wessel, H. Wolff, A. Börger, C. Baehtz, K.-D. Becker, R. Dronskowski, and M. Lerch, J. Solid State Chem., **183**, 2051 (2010).

[68] H. Schilling, A. Stork, E. Irran, H. Wolff, T. Bredow, R. Dronskowski, and M. Lerch, Angew. Chem., Int. Ed. Engl., **46**, 2931 (2007).

[69] H. Schilling, H. Wolff, R. Dronskowski, and M. Lerch, Z. Naturforsch., **61B**, 660 (2006).

[70] T. Bredow, M.-W. Lumey, R. Dronskowski, H. Schilling, J. Pickardt, and M. Lerch, Z. Anorg. Allg. Chem., **632**, 1157 (2006).

[71] H. Wolff, M. Lerch, H. Schilling, C. Bähtz, and R. Dronskowski, J. Solid State Chem., **181**, 2684 (2008).

[72] T. Lüdtke, A. Schmidt, C. Göbel, A. Fischer, N. Becker, C. Reimann, T. Bredow, R.

Dronskowski, and M. Lerch, Inorg. Chem., **53**, 11691 (2014).

[73] Z. Wang, J. Hou, C. Yang, S. Jiao, K. Huang and H. Zhu, Energy Environ. Sci., **6**, 2134 (2013).

[74] J. Garcia-Barriocanal, A. Rivera-Calzada, M. Varela, Z. Sefrioui, E. Iborra, C. Leon, S. J. Pennycook, and J. Santamaria, Science, **321**, 676 (2008).

[75] 応用物理学会編, 応用物理ハンドブック　第2版, 2002年, 丸善株式会社.

[76] P. R. Willmott and J. R. Huber, Rev. Mod. Phys., **72**, 315 (2000).

[77] C. Kittel, *Introduction to Solid State Physics (8th edition)* (Wiley, New York, 2004).

[78] 日本表面科学会編, 透過型電子顕微鏡, 1999 年, 丸善株式会社.

[79] F. J. Giessibl, Rev. Mod. Phys., **75**, 949 (2003).

[80] J. Goldstein, D. E. Newbury, D. C. Joy, C. E. Lyman, P. Echlin, E. Lifshin, L. Sawyer,and J. R. Michael, *Scanning Electron Microscopy and X-ray Microanalysis: Third Edition* (Springer, 2007).

[81] 青野正和編, 表面の組成分析, 1999 年, 丸善株式会社.

[82] P. Williams, Ann. Rev. Mater. Sci., **15**, 517 (1985).

[83] P. Van der Heide, *X-ray Photoelectron Spectroscopy: An introduction to Principles and Practices* (John Wiley & Sons, 2011).

[84] 藤原裕之著, 分光エリプソメトリー, 2011年, 丸善出版.

[85] L. J. van der Pauw, Philips Res. Repts., **13**, 1 (1958).

[86] 河東田隆著, 半導体評価技術, 1989 年, 産業図書.

[87] G. E. Jellison and F. A. Modine, Appl. Phys. Lett., **69**, 371 (1996).

[88] L. Miao, S. Tanemura, P. Jin, K. Kaneko, A. Terai, and N. Nabatova-Gabain, J. Cryst. Growth, **254**, 100 (2003).

[89] J. Y. W. Seto, J. Appl. Phys., **46**, 5247 (1975).

[90] Y. Furubayashi, N. Yamada, Y. Hirose, Y. Yamamoto, M. Otani, T. Hitosugi, T. Shimada, and T. Hasegawa, J. Appl. Phys., **101**, 093705 (2007).

[91] T. Minami, Thin Solid Films, **516**, 5822 (2008).

[92] C. M. Fang, E. Orhan, G. A. de Wijs, H. T. Hintzen, R. A. de Groot, R. Marchand, J.-Y. Saillardd, and G. de With, J. Matter. Chem., **11**, 1248 (2001).

[93] J. Grins, J. Eur. Ceram. Soc., **17**, 1819 (1997).

[94] W. Dang, H. Chen, N. Umezawa, and J. Zhang, Phys. Chem. Chem. Phys., **17**, 17980 (2015).

[95] Q. Li, J. Xue, W. Liang, J.-H. Huang, and J. K. Shang, Philos. Mag. Lett., **88**, 231 (2008).

[96] S. D. Yoon, Y. Chen, A. Yang, T. L Goodrich, X. Zuo, D. A Arena, K. Ziemer, C. Vittoria, and V. G Harris, J. Phys.: Condens. Matter, **18,** L355 (2006).

[97] N. Yamada, K. Maruya, Y. Yamaguchi, X. Cao, and Y. Ninomiya, Chem. Mater., ***27***, 8076 (2015).

[98] T. Ebina, T. Iwasaki, Y. Onodera, H. Hayashi, T. Nagase, A. Chatterjee, and K. Chiba, J. Power Sources, **81**, 393 (1999).

[99] K. Matsubara, P. Fons, A. Yamada, M. Watanabe, and S. Niki, Thin Solid Films, **347**, 238 (1999).

[100] T. Hitosugi, A. Ueda, S. Nakao, N. Yamada, Y. Furubayashi, Y. Hirose, T. Shimada, and T. Hasegawa, Appl. Phys. Lett., **90**, 212106 (2007).

[101] C. W. Schneider, M. Esposito, I. Marozau, K. Conder, M. Doebeli, Y. Hu, M. Mallepell, A. Wokaun, and T. Lippert, Appl. Phys. Lett., **97**, 192107 (2010).

[102] M. Mukaida, Y. Takano, K. Chiba, T. Moriya, M. Kusunoki, and S. Ohshima, Jpn. J. Appl. Phys., **38**, L926 (1999).

[103] D. Byun, Y. Jin, B. Kim, J. K. Lee, and D. Park, J. Hazard. Mater., **B73**, 199 (2000).

[104] W.-J. Yin, S. Chen, J.-H. Yang, X.-G. Gong, Y. Yan, and S.-H. Wei, Appl. Phys. Lett., **96**, 221901, (2010).